Picosecond Spectroscopy of van der Waals Clusters

Thesis by

Dean Michael Willberg

In Partial Fulfillment of the Requirements

for the Degree of

Doctor of Philosophy

California Institute of Technology

Pasadena, California

1994

(Submitted July 9, 1993)

Acknowledgments

Creation is a beautiful and wonderful thing and I am grateful that the good Lord in his mercy has given me the opportunity to enjoy it, and to make my living studying it. I am a very fortunate person, through no fault of my own.

There are many people who throughout my life have encouraged me to love and appreciate nature. These people have my deepest gratitude, and my highest respect. Among them I would especially like to acknowledge my parents who have encouraged me in both word and deed, but more importantly, they have supported me by the things that they taught me. I would also like to acknowledge my debts to my uncle Mayland Toole, and my fishing mentor Joey Cocciloni. Their friendships were very important to me as I grew up, and in many ways they were among the most important teachers that I have ever had.

Dr. W. R. Thorson, and Dr. J. E. Bertie at the University of Alberta both befriended me as an undergraduate and encouraged me to consider chemistry as a career. I still appreciate their good advice, their honesty about the chemical profession, and their enthusiasm for good science.

Here at Caltech I would like to thank Prof. Zewail for accepting me into his research group, for his guidance, for his hard work in keeping the research machinery operating, and for his infectious enthusiasm. His vision of the "big picture", and his commitment to detail have both been inspirational.

I have worked with no finer people than with my comrades in the Zewail group. The mode of operation of this group has always seemed to be based on teamwork, friendship, and kindness. Most of what I know about physical chemistry I have learned from members of this group. I would especially like to thank the two postdoctoral fellows, Jack Breen and Michael Gutmann with whom I was privileged to work with. It was Jack's dedication and leadership that helped get our laboratory off to the best possible

start. The time spent working with Michael were the most enjoyable years of research that I have experienced so far. It has been my fortune to reap some of the benefits of the seeds that Larry Peng and P. Cong planted, and I am grateful for their work which I inherited. Over the last six months it has been a pleasure to work with Ahmed Heikal, and I wish him good luck with the lab. Although I never worked with them directly, Martin Gruebele and Bob Bowman patiently answered my questions, and were always willing to help lend a hand when it was needed.

With respect to this thesis in particular, I would like to thank Jennifer Herek and Chuck Williamson who both did amazing jobs of proofreading the text. Proofreading is a miserable job, especially when one has research of his/her own to do. Their thorough performance at this mind numbing task was a great act of kindness.

I would also like to thank my friends that have encouraged me in my work, joined me at play, and provided the listening ears when I needed to talk. At Caltech special mention should go to Earl Potter and Donnie Cotter. The miles of trails that I hiked with these two, were among the best that I have traveled. I hope that there will be more trails in the future. The folks at Pasadena Mennonite Church were always a source of encouragement, and I hope that this community will continue to prosper in the years ahead. The Harmons deserve special mention in that they have graciously accepted me into their family, and have given me support through some of my most difficult times here in California. I hope that I can return their love in good measure.

Finally I would like to acknowledge the love and encouragement of my wife Laurie. I have spent my past with some wonderful people, but I get to spend my future with Laurie. The future looks good.

Funding for this work was provided for by the National Science Foundation and the Air Force Office of Scientific Research.

Abstract

This thesis presents pump/probe picosecond spectroscopic investigations of the dynamics of van der Waals clusters. The first phase of these investigations was the construction of a laboratory specifically designed for van der Waals cluster research consisting of a molecular beam apparatus and a two-color picosecond laser system. It is possible to perform both time resolved laser induced fluorescence (LIF), and multi-photon ionization (MPI) experiments in this laboratory. A description of the construction and operation of the laboratory, focusing on the laser system, is presented. A full account of the real-time studies of the vibrational predissociation of I_2X_n clusters where X = He, Ne, Ar, and H_2, and n = 1 - 4 is given. The first set of experiments described is the measurement of the rates of vibrational predissociation for I_2Ne and I_2Ar clusters. The results for I_2Ne are compared with a number of theoretical models of vibrational predissociation, specifically focusing on the dependence of the rates on the initially prepared vibrational state of the cluster. The results for the I_2Ar cluster are described in terms of the competition between two relaxation channels: vibrational predissociation of the van der Waals cluster, and electronic predissociation of the I_2 moiety. The second set of experiments are the analogous measurements of the rates of vibrational predissociation of I_2He clusters. These results are compared with the I_2Ne results, as well as with lifetime estimates available from high resolution spectroscopy. The final chapter in this series describes our investigation of vibrational predissociation and intramolecular vibrational energy relaxation in I_2Ne_n (n = 2 - 4) clusters. The dynamics of these larger clusters are inherently more complicated than when n = 1, however, a quantitative model for the fragmentation of n = 2 clusters is presented. This thesis also presents a preliminary description of an ongoing MPI experiment on the dynamics of *t*-stilbene clusters.

Table of Contents

Chapter I

Introduction

The study of van der Waals clusters has been an active field of research in the chemical physics community for many years, and in the past two decades it has undergone a period of explosive growth. Much of this work has focused on describing and cataloging the properties of clusters themselves.[1] Apart from that, there has been somewhat of a marriage between the fields of cluster research and chemical dynamics, as clusters have proven to be useful environments in which to explore dynamical processes. This marriage has been facilitated by advances in molecular beam technology and laser spectroscopy, particularily those advances that assist in the generation and characterization of van der Waals clusters.

As is the case of many active fields of science, it is somewhat difficult to establish if there is one objective over riding all the intense experimental and theoretical activity that has been performed in the name of cluster dynamics. The motivation of much of this work, indeed probably its best-selling feature, has been the perception that clusters are ideal systems in which to study how the bulk properties of solids and liquids evolve out of the microscopic properties of the isolated molecule.[1] As the cluster size increases, the intermolecular forces that a molecule experiences is assumed to begin to approximate those found in the solid or liquid state-environment.

There has been recent successes in observing *condensed phase dynamics* in van der Waals clusters. An example in this regard is the study by Potter *et al.* on the photofragmentation of I_2 embedded in large clusters of argon.[2] The behavior that they observed in these experiments is analogous to the caging of nascent atomic iodine in photodissociation studies in liquids.[3] Another example is excited-state proton transfer which is observed in the mixed clusters of naphthol (or phenol) and ammonia.[4,5] The results of these studies can be correlated to the acid/base chemistry of these species in solution.[6]

In addition to serving as microscopic environments in which solvation dynamics can be studied, van der Waals clusters are also interesting as model systems for studying

intramolecular vibrational energy redistribution (IVR) and vibrational predissociation (VP). Quantum mechanical, semi-classical, classical and statistical theories have attempted to describe the VP process in vdW clusters. In particular, halogen-rare gas clusters, A_2X, have become prototypical systems for numerous theoretical investigations.[7] These systems are amiable to theoretical calculations for a number of reasons. First, the initially prepared excited state of the cluster can be reasonably well defined, as is discussed in Chapters III-V for the case of the excited I_2X (X = He, Ne, and Ar) clusters. In these clusters the initially prepared state is an excited vibrational level (v'_i) of the *B*-electronic state of the cluster. Secondly, the energy required to break a van der Waals bond is rather low, typically > 80 cm^{-1}, which is less than one vibrational quantum of the I_2 stretch. Finally, the dynamics of cluster fragmentation occur on relatively simple potential energy surfaces that can be characterized via spectroscopic methods. Conversely, trying to study VP of covalent bonds would involve excitation of the molecule to extremely high vibrational energy levels where the potential surface is often difficult to characterize, and where matters are complicated by the extremely high density of states and by the rotational-vibrational coupling.

The vast majority of spectroscopic work done on clusters has been performed in the frequency domain. This work has had success in the determination of the structures of clusters, especially those experiments employing IR and far-IR lasers which probed the actual vdW bond directly.[8] Frequency-domain experiments in the visible region have successfully determined the vibrational level structures of clusters. Furthermore, frequency shifts in the vibronic spectra of molecules as the chromophore in the cluster undergoes stepwise *solvation* provides additional information about the intermolecular interactions. These experiments have also proven invaluable for product state analysis in vibrational predissociation experiments.[7]

For a large number of systems, linewidth measurements taken in the frequency domain have been used to deduce the lifetimes of dynamical processes, particularly

vibrational predissociation lifetimes (see References 8 and 9 for recent reviews). However, frequency domain experiments do not readily provide information on the rates of dynamical processes in clusters. This is unfortunate, as many of the theories on VP focus on calculating these rate constants. This topic will be extensively discussed in Chapter IV, but briefly, linewidth analysis of cluster transitions is difficult, as there is often significant rotational congestion and other sources of inhomogeneous broadening. Furthermore if the dynamical pathway is complicated, and contains more than one rate process, then the linewidth measurement will only yield the rate constant of the fastest process.[10] Only a time-resolved experiment can determine the rates and sequences of a multistep dynamical process, such as VP in I_2Ne_2 (discussed in Chapter V).

Time-resolved experiments on van der Waals clusters is the focus of this thesis. Experiments of this nature have been previously performed in this group, and in others; these investigations focused primarily on the processes of VP and IVR in van der Waals clusters.[11,12] The work reported on in this thesis contains my contribution to our research groups concerted effort into applying ultra-fast laser techniques to the study of dynamical processes in van der Waal clusters. All of the work presented in this thesis, both the construction of the apparatus and the operation of the system, has been performed in collaboration with several coworkers, all under the instruction of Dr. A. H. Zewail. It should be noted that Chapters III-V have been taken, with minor revisions, from a previously published series of papers.[13] My personal contributions to these efforts will be discussed below.

Chapter II presents a description of the laboratory apparatus built especially for the study of time-resolved processes in van der Waals clusters. A detailed description of the molecular beam apparatus has been previously presented in a prior thesis from this group. Therefore, this instrument will be only briefly discussed, focusing primarily on some recent changes in design and operation. A large portion of this chapter focuses on the design, and operation of the homebuilt picosecond laser system. A section of this chapter is

designed to act as a comprehensive manual for the alignment of this laser system, as little prior documentation for this system exists, or has not been organized in a coherent manner. Furthermore, this chapter describes the set-up of the system to perform time-resolved laser-induced fluorescence (LIF) experiments on van der Waals clusters, the subject of the following three chapters.

Chapters III through V make up the bulk of this thesis, and present a thorough account of our work on I_2X_n clusters where (X = He, Ne, Ar, and H_2, and n = 1-4). The vibrational dynamics of these clusters, as previously mentioned, has become a classic benchmark system for many theoretical models. The frequency domain spectroscopy of these clusters was first studied in a series of pioneering and comprehensive papers published by Levy and coworkers.[14] These investigators assigned the excitation transitions of each of the clusters, determined the frequency shifts as a function of cluster size, and determined the van der Waals bond strengths. This work proved invaluable for our investigations. However, the line-width measurements of the Levy group did not provide accurate values for the rates of vibrational predissociation as required for comparison with theoretical models.

In Chapter III the results are presented for our real-time studies on the VP of vibronically excited I_2Ne clusters as shown in equation (1).

$$I_2Ne(B,v'_i) \xrightarrow{k_{vp}} I_2(B,v'_i-1) + Ne \qquad (1)$$

The state-to-state VP rates were measured over a range of initially prepared vibrational levels, v'_i. The rate of VP was found to have a nonlinear dependence on v'_i. Our results were compared with a number of theoretical models, especially the *energy-gap law* of Beswick and Jortner,[15] which have attempted to describe the v'_i-dependence of k_{VP}. The results of our investigations into I_2Ar clusters are also presented. This is an interesting system with which to compare our I_2Ne results. First, the well depth of the I_2-Ar bond is

relatively deep (200 cm^{-1}), and it requires the energy of three quanta of the I_2 stretch to cause fragmentation. Secondly, electronic pre-dissociation of the I_2 moiety is a second channel available for relaxation of the cluster.

The extension of our investigations into the study of vibrational predissociation in I_2X clusters is presented in Chapter IV, particularly focusing on the I_2He cluster. This is the only cluster for which Levy and coworkers were able to obtain sufficient rotational resolution that they could make reasonably accurate linewidth measurements. By de-convoluting these linewidths, they were able to obtain estimates of the VP lifetimes of I_2He clusters over the same range of initially excited states (v'_i) that we were able to access in our experiment. Therefore, this is one of the few cases for which the lifetimes obtained by real-time and line-width experiments can be dirrectly compared. Furthermore,there is evidence that I_2He and I_2Ne have the same structure, and that they both decay solely via VP. Therefore, the results for both of these clusters should provide two independent sets of data which allow theoretical models to be tested for their dependence on the van der Waals bond energy, and the reduced mass of the predissociating cluster.

Chapter V presents our study on VP in larger clusters, which undergo the composite reaction,

$$I_2Ne_n(B,v'_i) \longrightarrow I_2(B,v'_i - m) + n\,Ne. \qquad (2)$$

Again, the results are discussed in relation to the mechanisms of vibrational predissociation. However, in these larger clusters, the effects of IVR begin to play an important role in the dynamics of cluster fragmentation. Even when $n = 2$ the effects of IVR and the increased density of states is apparent. In this chapter, a quantitative model is presented that describes the dynamics of I_2Ne_2 as the consecutive bond breaking of the two van der Waals bonds. This model takes into account both the rate constants and the

product state distribution of the fragmentation process. As n gets even larger, IVR becomes even more important and significantly retards the efficiency of VP. The VP process of these clusters is so complex that the possibility of elucidating their dynamics simply by observing the rise of nascent $I_2(v'_i - 1)$ is eliminated. Therefore an *effective* over-all reaction rate constant is introduced in order to discuss the fragmentation processes of these larger clusters, and to facilitate comparison with the dynamics observed in I_2Ne_2 and I_2Ne.

Chapter VI presents an attempt at observing the photo-isomerization dynamics of *t*-stilbene in van der Waals clusters. The excited-state dynamics of stilbene has become a model system for the study of reaction dynamics in the condensed phase, and is also an example of a cis/trans isomerization, an important class of unimolecular reactions.[16] A series of papers previously published by this research group has characterized the photoisomerization dynamics of *t*-stilbene isolated in the molecular beam.[17] Chronologically, this chapter accounts for the first and latest projects performed in this laboratory. Measuring the fluorescence lifetime of *t*-stilbene, excited to the $S_1 \leftarrow S_0$ origin, in mass-selected argon clusters [$St(Ar)_n$, $n = 1 - 10$] was the first project attempted in this laboratory. Within experimental error, the fluorescence lifetime of *t*-stilbene in these Ar clusters was found to be equal to the value for the isolated molecule (2.7 ns).[18] Present studies continue in the attempt to measure the rates of photo-isomerization of stilbene in these clusters by exciting them at energies in excess of 1200 cm^{-1} of the origin. It is hoped that these studies will help to explain the order of magnitude difference between the isomerization rates of *t*-stilbene isolated in the molecular beam and in solution.

1.1 References

1. M. Kappes,and S. Leutwyler, in *Atomic and Molecular Beam Methods Vol. 1*, ed. by G. Scoles, (Oxford University Press, 1988) p.380.

2 a) E. D. Potter *Ph. D. Thesis, California Institute of Technology,* (1993); b) E. D. Potter, Q. Liu, and A. H. Zewail, Chem. Phys. Lett., **200**, 605 (1992).

3. A. L. Harris, J. K. Brown, and C. B. Harris, Ann. Rev. Phys. Chem. **39**, 341 (1988).

4. (a) O. Cheshnovsky, S. Leutwyler, J. Chem. Phys. **88**, 4127 (1988); (b) R. Knochenmuss, S. Leutwyler, J. Chem. Phys. **91**, 1268 (1989); (c) T. Droz, R. Knochenmuss, S. Leutwyler, J. Chem. Phys. **93**, 4520 (1990); (d) J. J. Breen, L. W. Peng, D. M. Willberg, A. Heikal, P. Cong, and A. H. Zewail, J. Chem. Phys. **92**, 805 (1990); (e) L. W. Peng, *Ph. D. Thesis, California Institute of Technology*, (1991); (f) M. F. Hineman, G. A. Brucker, D. F. Kelley, and E. R. Bernstein, J. Chem. Phys. **97**, 3341 (1992).

5. (a) J. Steadman, and J. A. Syage, J. Phys. Chem. **95**, 326 (1991); (b) J. Steadman, and J. A. Syage, J. Am. Chem. Soc. **113**, 6786 (1991); (c) J. A. Syage, and J. Steadman, J. Chem. Phys. **95**, 2497 (1991).

6. J. Lee, G. W. Robinson, S. P. Webb, L. A. Philips, and J. H. Clark, J. Am. Chem. Soc. **108**, 6538 (1986); S. P. Webb, L. A. Phillips, S. W. Yeh, L. M. Tolbert, and J. H. Clark, J. Phys. Chem. **90**, 5154 (1986).

7. D. H. Levy, Adv. Chem. Phys. 47, part 1, 323 (1981) and references therein.

8. a) R. J Saykally, and G. A. Blake, Science, **249**, 1570 (1993); (b) R. E. Miller, Science, **240**, 447 (1988).

9. (a). K. C. Janda, Adv. Chem. Phys. **60**, 2011 (1985); (b). F. G. Celli and K. C. Janda, Chem. Rev. **86**, 507 (1986); (c). K. C. Janda and C. Bieler, in *Atomic and Molecular Clusters*, E. R. Bernstein ed., Elsevier, Amsterdam (1990), pp. 455. W. R. Gentry, in *Structure and Dynamics of Weakly Bound Molecular Complexes*, NATO ASI series, A. Weber ed., D. Reidel, Dordrecht (1987), pp. 467.

10. D. M. Semmes, J. S. Baskin, and A. H. Zewail, J. Chem. Phys. **92**, 3359 (1990).

11. L. R. Khundkar, and A. H. Zewail, Ann. Rev. Phys. Chem. **41**, 15 (1990).

12. M. P Casassa, Chem. Rev. **88**, 815 (1988).

13. (a) D. M. Willberg, M. Gutmann, J. J. Breen, and A. H. Zewail, J. Chem. Phys. **96**, 198 (1992); (b) M. Gutmann, D. M. Willberg, and A. H. Zewail, J. Chem. Phys. **97**, 8048 (1992); (c) M. Gutmann, D. M. Willberg, and A. H. Zewail, J. Chem. Phys. **97**, 8048 (1992).

14. (a) W. Sharfin, K. E. Johnson, L. Wharton, and D. H. Levy, J. Chem. Phys. **71**, 1292 (1979); (b) J. E. Kenny, K. E. Johnson, W. Sharfin, and D. H. Levy, J. Chem. Phys. **72**, 1109 (1980); (c) K. E. Johnson, W. Sharfin, and D. H. Levy, J. Chem. Phys. **74**, 163 (1981); (d) J. A. Blazy, B. M. DeKoven, T. D. Russell, and D. H. Levy, J. Chem. Phys. **72**, 2439 (1980); (e) G. Kubiak, P. S. H. Fitch, L. Wharton, and D. H. Levy, J. Chem. Phys. **68**, 4477 (1978); (f) R. E. Smalley, L. Wharton, and D. H. Levy, J. Chem. Phys. **68**, 671 (1978).

15. J. A. Beswick, and J. Jortner, Adv. Chem. Phys. **47**, part 1, 363 (1981).

16. D. H. Waldeck, Chem. Rev. **91**, 415 (1991).

17. (a) J. A. Syage, P. M. Felker, and A. H. Zewail, J. Chem. Phys. **81**, 4685 (1984);(b) J. A. Syage, P. M. Felker, and A. H. Zewail, J. Chem. Phys. **81**, 4706 (1984);(c) P. M. Felker, and A. H. Zewail, J. Phys. Chem. **89**, 5402 (1985).

18 P. M. Felker, W. R. Lambert, and A. H. Zewail, J. Chem. Phys. **82**, 3003 (1985)

Chapter II

Experimental

2.1 Introduction

All of the experiments that are described in this thesis were performed using the combination of time-resolved laser spectroscopy, and molecular beam methods. Pump-probe laser spectroscopy on isolated molecules is the primary experimental method used in this research group. In simple terms the chemical species of interest, whether it is single molecules or clusters, are seeded into a molecular beam where they are isolated from external perturbations. The reaction of interest is initiated by the pump laser. At a known time later the probe laser samples the population of the remaining reactants, or the population of one of the products of the reaction. A transient profile of the dynamics of the reaction is obtained by varying the delay time between the pump and probe lasers. This method has been proven to be useful on time scales over six orders of magnitude from the femtosecond to the nanosecond regime. The time resolution of a pump-probe experiment depends solely on the cross-correlation of the pump and probe laser pulses, and the timing jitter between the two pulses. The general applications of this methodology have been reviewed in detail elsewhere.[1] This chapter will describe the design and operation of a laboratory specifically built for studying time resolved reactions in clusters using the pump-probe methodology

The work encompassed by this dissertation involved the design and construction of an entirely new laboratory devoted to picosecond time-resolved studies of clusters in molecular beams. The laboratory was designed by members of this research group, and most of the equipment was homebuilt.[2] Two different types of pump/probe experiments were performed in this laboratory, time-resolved multi-photon ionization (MPI) experiments (Chapter VI),[3] and time-resolved laser-induced fluorescence (LIF) experiments (Chapters III-V). The experimental apparatus was designed so that the system could be switched between MPI and LIF configurations with minimal effort.

Time resolved cluster experiments make certain demands on the design of the experimental apparatus, and these demands were taken into consideration during the

construction of this laboratory. The first consideration is the "synthesis" of the clusters themselves. Cluster formation in the adiabatic expansion of a supersonic nozzle is highly dependent on the temperature of the expansion; the colder the expansion, the more efficient cluster nucleation. High stagnation pressures behind the nozzle are required in order to enhance cooling. In our system, this is realized by using a pulsed nozzle, and an high throughput diffusion pump in the expansion chamber. The second requirement of many cluster experiments is the ability to size select the cluster under examination. This is especially true for those systems where a number of clusters have overlapping absorption transitions, thereby making it impossible to selectively excite a cluster of a given size. In our laboratory a time-of-flight mass spectrometer (TOFMS) has been incorporated into the molecular beam apparatus to serve this function.

There are requirements made of the laser system as well. First of all both the pump and probe lasers have to be tunable. Unlike the situation with ion clusters, that can be mass selected before interaction with the lasers, the experiment on neutral clusters is performed on a mixture of clusters generated in the molecular beam. In a number of these experiments, especially the LIF experiments described in chapters (III-V), selection of a cluster of given size is accomplished by exciting a spectroscopic transition peculiar to the cluster with the pump laser. Additionally, these same experiments involved measuring the state-to-state rates of vibrational predissociation in I_2X_n clusters which required the pump laser to be tuned to various vibronic transitions of a given cluster. The probe laser in these experiments was also required to be tunable as it was set to specified $I_2\, f \leftarrow B$ state transitions that were state dependent. Furthermore, threshold or near threshold ionization is required in the multi-photon ionization (MPI) experiments in order to minimize fragmentation of the ionized cluster. Therefore a tunable probe laser is required for MPI as well LIF experiments.

The rest of this chapter will be organized as follows. In Section 2.2, a brief description of the design of the molecular beam apparatus will be presented. The design

of this system has been described in detail in a previous thesis from this group.[3] In Section 2.3 the design and construction of the laser system will be described in detail. As this laboratory was almost completely homebuilt much of the knowledge of its operation had to be obtained empirically; therefore Section 2.4 presents a manual for the alignment and operation of the system.

2.2 The Molecular Beam Apparatus

The molecular beam apparatus, which was built specifically for studying gas phase clusters is schematically presented in Figure 1. The beam apparatus consisted of three chambers: the source, buffer, and time-of-flight (TOF) compartment. A thorough description of the dimensions of the vacuum chambers is given in reference 3. The source chamber is pumped by a Varian VHS-10 diffusion pump, while the buffer and TOF chambers are each pumped by Varian VHS-6 diffusion pumps. All three pumps are outfitted with Varian cryobaffles and pneumatic gate valves. In order to minimized liquid nitrogen expenditures, the VHS-10 cryobaffle was converted to operate with institutional chilled water as a coolant. The VHS-10 diffusion pump is backed by a Leybold-Heraeus D90A mechanical pump, while the other two diffusion pumps are backed by a single Leybold-Heraeus D60A.

The nozzle was mounted on a carriage which can be translated along the molecular beam axis. This design allowed for adjustment of the X/D ratio; X is the distance between the nozzle and the intersection point with the lasers, and D is the diameter of the nozzle. Time-resolved LIF experiments were performed on the free-jet expansion in the expansion chamber. Therefore, for this experimental configuration the nozzle carriage was set at a position along the molecular beam axis preceding the four-way cross (see Figure 1). However, when MPI experiments were being performed, the nozzle carriage was typically set at a position between 3-5 cm in front of the first skimmer.

Two different nozzles have been used in this system, a continuous flow (cw) glass nozzle, and a pulsed solenoid valve. The glass nozzle was home-built and had an orifice diameter of 75 μm. This nozzle could be heated using a heating tape controlled dynamically by an Omega Engineering Model CN310KC Temperature Controller. Temperature feedback to the controller was achieved by using a chromel-alluminum thermocouple. The cw nozzle made it possible to perform the experiments at the maximum Q-switching repetition rate of the laser, (typically 800 Hz), and greatly increasing the speed at which data could be collected. However, due to the limitations of the pumping speed of the vacuum system, the stagnation pressure behind the glass nozzle was limited to 40 psig pure neon. If higher stagnation pressures were required, one had to resort to using the pulsed nozzle.

The pulsed nozzle (General Valve Series 9) had a nozzle diameter of 150 μm with a conical cross-section for maximum cluster formation.[4] A diagram of the latest nozzle and sample holder configuration used in this laboratory is shown in Figure 2 of Chapter VI. The pulsed nozzle driver was limited to a repetition rate of 100-130 Hz, which was therefore the maximum repetition rate at which data could be collected. However with the pulsed nozzle one could achieve very high stagnation pressures, up to 160 psig with pure He as the carrier gas. These high pressures were often required in order to generate sufficiently large cluster populations, especially I_2He clusters (chapter 4).

The triggering of the pulsed nozzle was controlled by a homebuilt dual pulse generator,[5] which also controlled the firing of the Q-switch in the Nd:YAG laser (*vide infra*). This box controlled the three parameters that were responsible for proper operation of the nozzle: 1) pulse width one (PW1), which controlled how long the nozzle was open (discussed below); 2) delay time two (DT2), typically 675-750 μs, which synchronized the gas pulse with the laser Q-switch; 3) the repetition rate of the nozzle, typically 100 Hz.

Under most circumstances PW1 was set between 300 and 400 μs. This parameter significantly influenced the quality of the gas jet, and hence the amount of signal detectable in an experiment. If PW1 was set below 300 μs, the nozzle would not fully open, thereby limiting the intensity of the molecular beam. If PW1 was set at too large of a value, typically > 425 μs, then the nozzle would double pulse and remain open significantly longer than intended. This could result in a gas load possibly exceeding the capabilities of the expansion chamber's diffusion pump. It should be noted that the solenoid valves could be extremely temperamental, and that the ideal value for PW1 could change with time (over periods of many weeks or months). If signal intensity is lost during the course of a set of experiments that last many weeks, PW1 should be one of the first parameter to be checked.

2.3 The Picosecond Laser System

The picosecond laser system that was built specifically for this work on clusters is comprised of a CW-pumped, modelocked, Q-switched (MLQS)Nd:YAG laser which synchronously pumps two tunable cavity-dumped picosecond dye lasers. Along with the three lasers which are the core of the system, there is the associated delay-line required for the pump-probe experiments, the optics required for second harmonic generation (SHG), and the optics necessary to steer the lasers into the molecular beam.

This system, centering on the MLQS YAG laser has a number of advantages over other picosecond laser designs. Standard CW-modelocked dye lasers typically have pulses with energy in the nanojoule range, which is too weak for ionization experiments in molecular beams. Usually these lasers are amplified by an external pulsed-dye-amplifier (PDA) to yield energies on the order of 100 μJ per pulse, which is more than sufficient for multiphoton ionization experiments. However, these systems require a pulsed Q-switched Nd:YAG laser to pump the PDA, which is a large installation and operational expense, and which limits the repetition rate of the laser to 20-30 Hz. On the other hand, the laser

system used in our laboratory requires no extra-cavity amplification; the visible energy of a dye-laser pulse is ~3-10 μJ, which is sufficient for most LIF and many MPI experiments. Therefore the MLQS system is, less expensive, less complicated, takes up less space, and is easier to tune than an amplified modelocked laser. Furthermore it can operate at repetition rates up to 800 Hz.

There are disadvantages with this system however, the first being that its time resolution is limited to 20-30 ps. Furthermore, since it does have low pulse energy, the lasers must be highly focused on the molecular beam to enhance MPI signal, which presents difficulties during alignment (*vide infra*). However, in most circumstances, these difficulties are compensated for by the relative simplicity, stability, and robustness of the system. Under most circumstances the laser system was stable on a day-to-day basis, and after a one hour warm-up period, only minor tweaking was required in order to reproduce the previous days performance.

2.3.1 The MLQS Nd:YAG Laser

The MLQS Nd:YAG laser (henceforth referred to as the YAG laser) was homebuilt with components intended for the Quantronix 416 CW laser system (see Figure 2). Not only was the home construction of the laser financially prudent, saving approximately twenty thousand dollars, the resulting resonator cavity proved to be superior to the commercial product. Only three major realignments of the cavity were required over a five year period. The resonator cavity consisted of three 8' Invar rods (for thermal stability) mounted in three aluminum support blocks, two of these rods served as rails onto which the laser components could be mounted with specially machined clamps.[6] Similar in nature to an optical bench, these clamps were restricted to linear motion along the laser axis.

The resonator cavity was approximately 1.9 m long; [this value is determined by the modelocking frequency(*vide infra*)]; and was bounded by a high-reflector mirror and

an output coupler (~ 20% transmission coefficient).[7] The high reflector was mounted on a micrometer (Klinger MR80.25), so that the cavity length can be adjusted for optimum modelocking performance.

The CW laser head and power supply/cooler were manufactored by the Quantronix Corp. (New York, Model 116). The laser head was mounted approximately 1/3 of the cavity length away from the front mirror. The DC power supply was operated between 31 and 35 amps current, depending on the age of the lamp used. Krypton arc lamps from a number of suppliers were tried in this system; the lamp that gave the best performance and longevity was the proprietary Quantronix long-life lamp, which would typically give between 550 and 750 hours of service.

The acousto-optic modelocker and Q-switch were also manufactured by the Quantronix Corp. (model numbers 352, and 351 respectively). Similar to the design of the Quantronix 416 laser cavity, the modelocker was mounted as close as possible to the output coupler, and the Q-switch was mounted as close as possible to the high reflector. Klinger TR80 mounts were used to adjust the angle of both devices with respect to the laser axis of the cavity. The driver for the model 351 modelocker generated a rf output frequency of 37.8 MHz, which corresponds to a cavity modelocking frequency of 76 MHz. The modelocker was cooled via a branch line of the primary cooling loop of the Quantronix 116 chiller. The repetition rate of the 352 Q-switch could be set between 1-1000 Hz, or it also could be fired by an external trigger; in our case the dual pulse generator which also controlled the pulsed nozzle.

An iris with a ~1 mm minimum diameter was used to select the TEM_{00} Gaussian mode in the cavity. Vertical polarization (with respect to the optical table) inside the laser cavity was selected via a fused quartz plate mounted at the Brewster angle.

The second harmonic (532 nm) of the 1.06μ fundamental was generated using a KTP crystal cut for type II phase matching. The crystal's dimensions were $3 \times 3 \times 5$ mm; it had antireflective coating for 1.06 μm on the input, and for 532 nm on the output faces

of the crystal. The crystal was placed in a homebuilt mount where the rotation about the laser axis could be adjusted as well as its angle with respect to the x and y axes. Although focusing the 1.06 μm fundamental into the KTP crystal was attempted, it was found that the best double efficiency occurred without focusing, when the KTP crystal was placed directly after the output coupler. The polarization of the 532 nm light was selected using a λ/2 waveplate, and the 532 nm was separated from the 1.06 μm fundamental with a dichroic beamsplitter. The 532 nm light is split again with a 50/50 beamsplitter in order to pump the two independent dye lasers.

The combined action of a modelocker and Q-switch results in a train of modelocked pulses superimposed on an asymmetric Q-switch envelope (see Figure 3). The modelocked pulses were measured to be 100 ps FWHM, and have a 12.8 ns peak-to-peak separation. The Q-switch envelope has a pulse width of approximately 180-300 ns. When the Q-switch repetition rate is set to 500 Hz the power of the laser output at 532 nm varies between 350 mW and 400 mW, depending on the quality and age of the arc lamp. This power corresponds to 700-800 μJ per Q-switch envelope. It has been our experience that each dye laser requires at least 300 μJ per Q-switch envelope of pump energy before they will operate in a regime that is both stable and of sufficient intensity to be useful for experimental purposes.

The modelocked pulses and Q-switch envelopes are monitored by directing the leakage out of the high reflector onto an E. G. & G. FND-100 photodiode. The signal from this photodiode is used to monitor the YAG laser's performance, and to trigger the cavity dumpers in the dye lasers. The FND-100 photodiodes are work-horses, at least four different diodes are used during the course of daily operations in our laboratory. The photodiodes are mounted in an aluminum "hockey-puck" assembly based on the design described in Reference 8, and are biased at 90 V with an Ever-Ready B-radio battery. Mounting the photodiode in this manner serves to minimize the electronic ringing of the circuit, which gives rise to anomalous peaks in the signal. These photodiodes have rise,

and fall times on the order of a few nanoseconds, which is sufficient to resolve the modelocked pulses (12.8 ns spacing, peak-to-peak).

2.3.2 The Synchronously Pumped Cavity Dumped Dye Lasers

The two dye lasers used in this laboratory are based on a design originally used in the Feyer group, with modifications incorporated by the Simon group.[9] The dye laser cavity is bound by two flat, broadband, high reflecting mirrors (the mirrors were coated for 600 nm). A plano-convex lens is the focusing element in the cavity, and is placed at its focal length (25 cm) distance from one end of the cavity. The beam waist is thereby kept on one of the flat mirrors, henceforth referred to as the back mirror. The front mirror of the cavity is mounted on a Klinger TR80 translational stage so that the optical path in the dye laser can be matched to the optical path in the YAG laser. Synchronously pumping of the dye laser requires matching cavity lengths; note however, that the physical length of each cavity is different, due to the differences in optical components in the YAG cavity compared with those found in the dye cavity. In the alignment section of this chapter the cavity length matching procedure will be described in detail.

The flowing dye cell is mounted at the Brewster angle and is placed as close to the back mirror as the optical mounts would allow. The flowing dye cell was homemade out of stainless steel, with 1.6 mm quartz windows spaced 1 mm apart. The windows are held in place using Torr-Seal epoxy (Varian). The 532 nm pulse train from the YAG is brought in as colinearly as possible to the optical path inside the dye laser (see figure 4). In order to enhance pumping efficiency, the 532 nm light is focused (with the 40 cm plano-convex lens) to match the dye laser spot size at the dye cell. Both the 532 nm light from the YAG laser, and the lasing inside the dye cavity are horizontally polarized with respect to the optical table. The dye cell is set at the Brewster angle in order to select horizontal polarization.

The cavity dumper consists of an electro-optic Pockels cell and Glan laser single escape window. The Pockels' Cell (Quantum Technology, model QK-10-1), contains a dueterated KDP crystal, and acts as a $\lambda/4$ waveplate when a 2.4 kV (determined empirically for 600 nm) voltage is placed transversely across the crystal. The Glan laser escape window (Karl Lambrecht, model MGLA-SW-8) allows horizontally polarized light to pass through, while vertically polarized light is ejected out of the cavity. Cavity dumping of a laser pulse is achieved by rapidly placing a 2.4 kV bias across the Pockels' cell (in a period of <3 ns). The laser pulse passes once through the Pockels' cell, is phase shifted 45°, and becomes circularly polarized. The pulse then is reflected off the front mirror, and passes through the Pockels' cell a second time, and is phase shifted an additional 45°. The dye laser pulse is again linearly polarized, but along an axis perpendicular to its original orientation. Therefore, when the pulse intercepts the Glan laser escape window it is ejected from the cavity. When the cavity is dumped, lasing in the dye laser essentially stops until the next Q-switch envelop arrives from the YAG laser.

There are two key factors in order for successful cavity dumping to occur, first, a stable trigger source is required to activate the Pockels' cell at the appropriate time, usually when the pulse in the dye laser has reached its maximum amplitude. Secondly, the pulsed 2.4 kV bias must have a rise time shorter than the round-trip time of a pulse in the dye laser cavity (*i. e.*, < 12.8 ns). The trigger source for the Pockels' cell is the FND-100 photodiode (PD1) which monitors the leakage of the high-reflector on the YAG laser. The signal from this photodiode is sent to trigger in connector of a SRS model DG535 digital delay generator. In order to minimize jitter due to fluctuations in the YAG laser, the discriminator is set to a rather high voltage (usually 0.5 V),which means that it is a modelocked pulse of the YAG laser well inside the Q-switch envelope which triggers the digital delay generator. The Pockels' cell itself is triggered by a TTL pulse from the delay generator. The advantage of this system is that it allows one to choose when to dump the dye laser, by simply adjusting the delay on the DG535 box.

The pulsed 2.4 kV bias is generated by a VFET switching circuit designed in the Dlott group,[10] and built by Tom Dunn of the Caltech Chemistry electronics shop. When the circuit is not operational, *i. e.*, when the dye laser is not being cavity dumped, both sides of the Pockels' cell are biased at 2.4 kV. The bias for the Pockels' cell is provided for by an EG&G Ortec 3kV power supply. When VFET switching circuit is triggered by the DG535 digital delay generator, the bias on one side of the Pockels' cell is dropped to ground, in approximately 2 ns. Recovery time for this circuit is 100 μs, sufficiently short for the Q-switch repetition rates that we run at during normal operations.

The wavelength of the dye laser is determined by selecting a laser dye with the appropriate gain profile, and by angle tuning two intracavity Fabry-Perot etalons. Lasing would occur at a frequency where the transmission bandwidths of both the etalons would overlap the gain profile of the dye. Table 1 lists the spectral tuning ranges of a number of dye/solvent combinations used during the course of the experiments described in this thesis. Dye concentrations were empirically found to have profound effects on the performance of the lasers, both in the accessible tuning range for a given dye, and in the output power of the dye laser. Steps by which the dye concentrations were optimized will be discussed in detail in Section 2.4. The dye circulators were homebuilt, and consisted of the pump (Micropump model 120), the reservoir, the filter (Filterite LM04SS-3/8), the hoses, and the dye cell (described above). All components of the circulators were either stainless steel or virgin polyethylene.

Both of the etalons were custom manufactured by the Virgo Corp. The first is an 5μm fixed air gap etalon; the inner surfaces of this etalon are coated for 70% reflectivity (at 600 nm). The second is a 100 μm thick solid etalon where both sides are also coated for 70% reflectivity. The optical characteristics of each of these etalons is listed in Table 2.[11] Often, when higher laser power was required and the bandwidth of the laser was not critical, the dye lasers would be run without the 100 μm etalon. Figure 5 shows the bandwidths of the pump laser set at 630.0 nm both with and without the 100 μm etalon.

Time resolution in pump-probe type experiments is achieved by delaying the probe pulse relative to the pump pulse using an arrangement reminiscent of a Michelson Interferometer. In our system the pump laser is collimated and set down a variable delay line, which is a Aerotech ATS224 linear positioning stage, (1 μm/step; total range 60 cm, or 4 ns of delay) before being sent to the molecular beam. A corner cube (Precision Lapping, 1 sec. accuracy) is mounted on the stage to reflect the pump pulse, (see Figure 6). The probe laser is collimated and sent down a static delay line before being sent to the molecular beam. The relative distances of the static and variable delay lines are set so that time-zero corresponds to the 100,000 step of the delay line. That is, if the delay line is set a step position of < 100,000 μm, the probe laser pulse arrives at the molecular beam before the pump laser pulse. If the delay line is set at a position > 100,000 μm then the pump laser pulse arrives first.

2.3.3 Data Collection System

The data collection system in this laboratory, including the data collection and analysis software, was described in detail in reference 3. Therefore, only a brief description will be presented here, focusing particularly on the timing sequences that coordinate the molecular beam nozzle, the lasers, and the detection systems. There are obvious differences how data is obtained when one is operating in a MPI mode as opposed to an LIF mode, but the heart of the system is basically the same. Before continuing on with the rest of this section, the reader is advised to look at Figure 7, which attempts to present the timing sequences in a block diagram format.

All LIF experiments were performed on the free-jet expansion in the expansion chamber (figure 1). Fluorescence was collected and collimated using a single plano-convex lens (f/1.5, 2 inches in diameter), that was mounted inside the chamber. A second identical lens was used to focus the fluorescence onto a 1P28 photomultiplier tube (PMT). It should be noted that much experimentation was done trying to optimize the geometry of

these collecting optics, particularly during the early experiments reported on in Chapter III. Spatial filtering of the fluorescence was tried in an attempt to reduce the extraneous signal produced by scattered light. This attempt failed, as the fluorescence signal was also reduced. It was found that by carefully blocking the scattering centers inside the chamber (see discussion in Section 2.4) the extraneous signal due to scattered light could be reduced to the point of being inconsequential.

Signal from the PMT was amplified 25× with a SRS440 high frequency preamplifier, before being sent to an Stanford Research Systems gated integrator (also referred to as the boxcar in this thesis). The averaged signal from the boxcar was sent to National Instruments A/D board (model NB-MIO-16H-9), which was interfaced with a Macintosh II computer. Both the boxcar, and the A/D board required triggering from the SRS535 digital delay generator.

When the system was operated in a TOFMS-MPI mode, two types of data collection schemes could be employed depending whether one wanted to obtain the TOF mass spectrum of the ionization products, or the integrated signal of one mass selected ion species. The detector for the positively charged ions generated by EI or MPI was a Galileo Corporation multichannel plate (MCP), typically biased at 1.8-2.0 kV. The signal from the MCP was also amplified 25× with the SRS440 high frequency preamplifier. If one wanted to measure the intensity of one particular ion species the signal could be sent to the boxcar, as done with the LIF experiments. The gate of the boxcar could be adjusted so that only the signal generated by one particular ion would be integrated over.

In order to obtain a TOF mass spectrum of all of the ionization products, the amplified signal from the MP is sent to a LeCroy transient digitizer. Besides the signal the transient digitizer also requires triggering by the SRS535 digital delay generator. The digitized mass spectrum is transferred to the Macintosh computer via a National Instruments NB-DMA-8-G GPIB interface board.

2.4 Operation of the Laser and Molecular Beam Apparatus

2.4.1 Alignment of the Delay Line

As previously mentioned in the introduction two types of experimental methods are used in the experiments described in this thesis, time-resolved LIF, and time-resolved MPI-TOFMS. These two different methodologies require differences in the arrangement and operation of the experimental apparatus. Figure 6 is a schematic of the set up of the optics *downstream* of the two dye lasers that are required in order to perform either LIF or TOFMS experiments on molecules in the molecular beam. The only major difference in the arrangement of the optics on the table is how the pump and probe beams are *combined*, *i. e.*, brought together in either a colinear or parallel configuration before they leave the table and are sent to the molecular beam. The arrangement of the apparatus for the MPI experiments is discussed in Chapter VI. For the LIF experiments reported on in Chapters III-V, the pump laser was visible, and the probe laser was UV. Therefore a dichroic beamsplitter which was highly reflective in the visible spectral region, and highly transmissive in the UV region could be used to make the pump and probe pulses colinear. This greatly simplified overlapping the two laser pulses on the molecular beam.

An important step in the set-up of both LIF and MPI experiments, is the alignment of the pump laser on the Aerotech linear positioning stage. If the pump laser is not properly collimated, or if it is not aligned colinearly with the stage's axis of travel, the beam spot as *seen* by the molecular beam can either change in its size, or it can walk. Either of these phenomena may influence the spatial overlap of the two lasers on the molecular beam, and introduce artifacts, such as a sloping base line, into an experimental transient. This is especially true if one attempts to measure lifetimes longer than 1 ns, since in these experiments the Aerotech stage has a long travel range (greater than 6"). We have found that the best solution to these problems, and the experimentally most expedient, is to collimate the pump laser with a telescope before the pulse enters the

variable delay line. If the frequency doubling of the pump laser is required then the SHG crystal should be mounted at the waist of the telescope.

Furthermore, consistent alignment of the pump laser along the Aerotech stage's direction of travel is important to ensure that the pump laser pulse does not walk as the delay is changed through the course of measuring a transient. We have found that using two permanently mounted irises (one before the Aerotech stage, and one mounted behind the stage), serve as useful guides to align the laser along the delay line. The corner-cube that is mounted on the Aerotech stage needs to be removed for this process.

2.4.2 Characterization of the Laser Pulses

Common to both the LIF and the TOFMS experiments is the need to characterize the pulsewidth of the pump and probe lasers, either by means of an autocorrelation for each laser, or by means of the cross-correlation measured of both the pump and probe lasers.

Real-time scanning autocorrelators, which are used in other laboratories of this research group,[12] are not suitable for our system due to its low repetition rate. Autocorrelations are performed using a Michelson interferometer which includes the Aerotech linear stage as the variable length arm. Obtaining autocorrelations for the dye lasers in our system is experimentally laborious due to the limited table space available, and requires the removal and realignment of practically all of our optics downstream of the two dye lasers. On the other hand obtaining the cross-correlation between the pump and probe laser is relatively easy, and the apparatus for this can be permanently installed on the laser table. In practically all situations, including optimization of the dye laser's cavity lengths (*vide infra*) we have found that a cross-correlation is a satisfactory replacement for an autocorrelation.

Cross-correlations are obtained by sum frequency generation of the pump and probe laser pulses in a $LiIO_3$ or a BBO crystal. A cross-correlation is obtained in the

same fashion as any transient scan, except rather than being sent to the molecular beam the visible pump and probe laser pulses are deflected into the cross-correlation apparatus. The apparatus is simple, and consists of; a lens (30 cm focal length) to spatially overlap the two pulses on the doubling crystal, the doubling crystal for sum frequency generation, a UG-11 filter (to filter out the residual visible light), and an FND-100 photodiode as detector. The mixed UV signal is collected on the FND-100 photodiode as a function of the position of the Aerotech variable delay line. We have discovered that the residual visible light after SHG (if the pump and/or probe lasers are frequency doubled), is of sufficient intensity for cross-correlation. Furthermore the presence of these crystals does not affect the FWHM of the measured cross-correlations. The advantage of this system is that the cross-correlation can be obtained with the pump and probe lasers being aligned in the same configuration as they would be for an experiment.

The shortest cross-correlation possible depends significantly on the laser dye and on the configuration of the dye lasers. The shortest cross-correlation measured in our system was 4800 steps, when a R590/methanol solution was used in the pump laser and DCM/DMSO was used in the probe laser. The 100 μm etalon was present in both lasers.

2.5 Alignment of the Picosecond Laser System

2.5.1 The MLQS Nd:YAG Laser

The alignment, or complete realignment, of the YAG laser is essentially identical to the procedure described in the Chapter V of the Quantronix 416 laser manual.[13] This manual should be referred to religiously in the unfortunate situation where complete realignment of the laser is required. In most situations complete realignment is not required, and often it can be avoided even if major repair work on the laser head is required, such as replacing the YAG rod. Therefore before attempting any procedure that may require realignment, such as removing an optical component or changing the YAG

rod inside the laser head, one should contact the service department of the Quantronix Corporation for any possible shortcuts.

If a complete re-alignment is required the procedure in Chapter V of the Quantronix 416 laser manual should be followed step-by-step. This section will describe those variations in the re-alignment procedure that are due to the differences between our homebuilt resonator cavity and the commercial available cavity that is described in the Quantronix manual. Of critical importance is getting the components of the cavity roughed in to their proper locations along the resonator cavity. The spacing of the components, with respect to the output couple are shown in Figure 2. Note that unlike the commercially available resonator, the position of components in the homebuilt cavity are almost infinitely adjustable, both along the optical axis, and in the directions perpendicular to it.[14] Therefore before beginning the alignment procedure careful note should be made of the location and orientation of all optical components in the cavity, especially if their removal is required during the alignment process (as is the case for the modelocker and Q-switch). A Helium-Neon laser is a great help in aligning the optics along a straight line. As far as possible the optical axis of the cavity should be made to be colinear with the invar rails; this will allow for large scale motion of components along the z-axis, with minimal walk in the x-direction.

The mount for the laser head, is not vertically adjustable (along the y-axis), and therefore it determines the height of the laser beam. The mounts for the modelocker, and Q-switch, were not designed to be adjustable along the y-axis, however, some adjustment is necessary. It was found that brass shims, in 0.010" and 0.005" thicknesses, could be inserted between Q-switch housing and the translational stage on which it was mounted. Adjusting the height this way is somewhat tiresome, but the end result is rather robust.

In our system we have replaced what the Quantronix manual refers to as a model 506 slow photodetector with the FND-100 photodetector described previously. Furthermore, we found that in order to conserve space, it was more efficient to

permanently mount it behind the rear of the cavity to measure the leakage from the high reflector, rather than having it placed at the front of the cavity. This photodiode is used throughout the alignment procedure and, also used to monitor the YAG lasers performance during daily operations.

In paragraph 5.1.5 (preliminary modelocker alignment), instruction 33, the operator is instructed to turn the rear mirror *x*-axis adjustment 3 to 4 turns clockwise. In our system, the fine *x*-axis adjustment knob of the high-reflector mirror mount should be turned 3 to 4 turns counterclockwise.

Our system uses a completely different SHG system than the Quantronix 416 commercial product, and unlike the procedure in the manual, the complete alignment of the MLQS laser should be finished before any work is done aligning the KTP crystal. The KTP crystal is mounted in an aluminum disk, and is a rather small target to hit with the 1.06 μm output of the YAG laser. It is important to note that the KTP crystal is expensive, and can be easily damaged if the incident 1.06 μm laser pulse strikes the aluminum near the edge of the crystal. Vaporized aluminum may coat the surface of the KTP, or differential heating of the crystal may cause it to fracture. Therefore the KTP crystal should be carefully aligned so that the 1.06 μm output of the YAG passes cleanly through the center of the crystal.

Once the YAG is properly aligned, it typically gives consistent daily performance over periods of many months to years; requiring only an occasional lamp change every 550-750 hours. Start-up and shut down procedures for the YAG are given in Chapter IV of the Quantronix manual. Usually start-up is followed by a one hour warm-up period, after which only very minor adjustments need to be made to the cavity length, the angle of the high-reflector, and occasionally the lamp current. In order to determine whether the YAG requires optimization, the power of the 532 nm output is monitored on a power meter, and the signal from the FND-100 photodiode is observed on a Textronix 2465B oscilloscope.

2.5.2 The Synchronously Pumped Cavity-Dumped Dye Lasers

This section will describe the procedures by which the dye lasers are aligned. First, a description of how the dye laser can be completely realigned will be presented. Usually this will only be required if there is a major failure of one of the optical components. Following this, there will be a brief discussion of how the dye lasers can be optimized for use on a daily basis. The first step in the completely realignment of the dye laser is to place the two flat end mirrors, the 25 cm plano-convex lens, and the dye cell in their proper positions. Lasing can occur with just these four elements of the cavity, the cavity-dumper and the etalons will be added later. The initial cavity length should be set to match the cavity length of the YAG laser, ~ 75". It should be noted that as more optical components are added to the cavity, the actual physical cavity length will need to be substantially decreased. Therefore, it is important to get the laser path as colinear as possible to the invar rails; this will greatly assist the operator in adjusting the cavity length as more components are introduced into the cavity. All cavity length adjustments should be performed by moving the front mirror, either by sliding the entire mount along the invar rails for major adjustments, or by adjusting the Klinger MR80.25 translational stage for precision changes in the cavity length.

In order to assure the colinearity of the dye laser cavity with the invar rails, the operator should make use of a Helium-Neon laser. It should be noted that the Klinger SL25.4BM mirror mounts are extremely solid, and if care is taken, the mirrors can be removed and replaced from these mounts without substantially affecting the x and y tilt adjustments. Therefore the cavity can be aligned around a He-Ne reference laser beam, (which will determine the axis of the dye laser) by passing the beam through an empty front mirror mount, as shown in Figure 8. The rear mirror x and y tilt micrometers should be adjusted so that the reflected He-Ne beam is colinear with the incident beam. After the rear mirror is adjusted the dye cell can be introduced into the cavity at the brewster angle,

followed by the intracavity lens. As far as possible the lens should be centered on the He-Ne laser beam. The last step in this process is to place the front mirror back in its mount.

Once the primary optical components are in place, the dye circulator can be started, and one can attempt to initiate lasing in the cavity. In order to make the detection of the onset of lasing easier, rhodamine 590 in methanol, which has the best gain of any of the dye/solvent combinations, should be used during the alignment procedure. A good mixture for this purpose is 100 mg L^{-1}. It is very important to note that the dye concentration should not be adjusted for maximum power until the 5 μm etalon (the largest source of loss) is placed in the cavity. Otherwise the intracavity dye laser intensity is so strong that the rear mirror, which is located at approximately the waist of the laser, can be damaged.

Finally the 532 nm pump beam from the YAG needs to be aligned. There are two imported parameters that need to be adjusted. First, obviously the 532 nm pump beam and the dye laser beam need to spatially overlap inside the dye cell. This is achieved by systematically sweeping the pump beam across the dye cell, using the pump beam steering mirrors as shown in Figure 8, and watching for the onset of lasing. Once lasing occurs, the dye laser power is maximized by fine tuning the pump beam steering mirrors, fine tuning the x and y-axis tilt adjustments of the front mirror mount, and by tuning the dye laser cavity length. The most effective way of monitoring the intracavity power of the dye lasers is to set up an FND-100 photodiode to monitor the leakage from the front mirror of the cavity. The signal from this diode can be directly monitored on a fast oscilloscope.

The second major adjustment required is the placement of the pump-focusing mirror along the z-axis. The best dye laser performance occurs when the spot size of the pump beam matches the spot size of the dye laser beam on the dye cell. If the pump laser spot size is too large, dye-laser power is lost. If the pump laser is focused too tightly, then the pointing of the dye laser can be extremely unstable. Furthermore, damage to the dye cells windows can occur if the pump laser beam is focused too tightly. At this stage in the

alignment process the *z*-axis adjustment of the pump lens should be made by carefully monitoring the dye laser performance on the FND-100 photodiode. Corrections for walking of the laser beam can be made by fine tuning the pump beam steering mirrors. Later, after the cavity dumper is installed, the spot size of the pump laser can undergo final fine tuning.

The next step in the process is the installation of the cavity dumper, consisting of the Pockels' cell and the Glan laser single escape window. The Pockels' cell should be installed such that the optical axis of the deuterated KDP crystal is concentric with the optical axis of the dye laser. Figure 9 shows a schematic of the best arrangement by which this is accomplished. First, two irises are aligned along the dye laser, these serve as guides for the He-Ne laser. Second, the He-Ne laser is installed, and its pointing direction is adjusted so that there is no clipping of its beam as it passes through the two irises. The Pockels' cell is then installed at its proper location (see Figure 4, note however that its exact location is not critical), and it is centered according to the directions given in its manual.[15] At this point the He-Ne laser can be removed from the dye laser's cavity. It is quite likely that the lasing of the dye laser will be weak, or even non-existent after the installation of the Pockels' cell. This can carefully be remedied by shortening the length of the laser cavity by adjusting the micrometer on the front mirror. Furthermore, minor adjustments of the *x* and *y*-axis tilt of the front mirror may also be required. The laser should be tweaked to its maximum intensity before installing the Glan-laser window (calcite polarizer). Installing the polarizer is not difficult, however it should be adjusted to maximize its transmission of light in the laser cavity. Later, after the etalons are installed, its angle can be adjusted to maximize the intensity of the cavity dumped laser pulse. Again, the cavity length should be shortened to maximize the intracavity dye-laser intensity.

After both the Pockels' cell and the polarizer are installed in the laser cavity, and intracavity lasing has again been optimized, the parameters that control the efficiency of

the cavity dumping can be set. First, the power supply to the Pockels' cell should be turned on, and set to 2.4 kV; this value has been determined empirically and may be adjusted, however operation at above 2.5 kV is not recommended. The SRS535 digital delay generator should be turned on and be triggered by PD1 (typically the discriminator on the SRS535 is set to -0.5 V); a TTL pulse from this box (delay should be between 30 and 100 ns) is set to trigger the Pockels' cell. Cavity dumping is best monitored on the FND-100 photodiode monitoring the leakage of the dye laser, as shown in figure 4. Once all the electronics are on the operator can begin to adjust the angular and spatial adjustments on the Pockels' cell in order to enhance cavity dumping. This process requires much trial and error. Figure 3 shows a oscilloscope trace of a cavity dumped pulse. Note that in this case cavity dumping was not 100 % efficient and did not completely quench lasing, giving rise to the trailing pulses. After the 5 μm air-gap etalon is installed the Pockels' cell may need to be slightly re-adjusted in order to compensate for any changes in the geometry of the optical path

The final step in assembling the dye-laser is to install the 5 μm air-gap etalon. Installation of the 5 μm air-gap etalon significantly changes the optical path length of the cavity as it is constructed of two thick billets of fused quartz. Furthermore, due to the 70% reflectivity coating of its interior surfaces it is a high loss optical component in the lasers cavity. Therefore, as was the case for the Pockels' Cell, its installation into the cavity can significantly reduce, or completely extinguish lasing. There are three operations that can be performed to maximize lasing at this point. First, the etalon should be installed so that it is close to perpendicular to the optical path of the dye laser, this will minimize the effect of "walking" the beam path due to the high refractive index of the fused quartz billets. Adjustment of the *x* and *y*-axis tilt of the front mirror can also help to compensate for a geometrical change of the optical path inside the dye laser cavity. Second, the concentration of the laser dye can be adjusted to increase the gain of the laser, to compensate for the loss introduced by the etalon. As previously mentioned, one should be

careful at this stage not to cause damage to the rear mirror of the cavity. The reader is referred to the section on changing laser dyes for the procedure on how to adjust the dye concentration (*vide infra*). Third, the laser cavity will again require shortening, by repositioning the front mirror, to compensate for the increase in the optical path length by the etalon.

Once the 5 μm air-gap etalon is installed the dye laser is ready for its final optimization. At this point it should be decided whether or not the 100 μm solid etalon should be installed. As discussed previously the issue in this decision is the trade-off of the total energy of the cavity dumped pulse, for higher frequency resolution (the FWHM of the pulse with the 100 μm etalon is ≤ 3 cm^{-1}). It should be noted however, that the 100 μm etalon only marginally affects the optical path length of the cavity. Once the laser is completely aligned, it can easily be operated both with or without the 100 μm etalon.

The first step in the final optimization of the dye laser is to adjust the dye concentration for the maximum laser power. This is accomplished by adding concentrated dye solution in 2-3 ml aliquots to the dye circulator's reservoir, while monitoring the dye lasers performance on the FND-100 photodiode. Between each addition of concentrate the operator should allow 2-3 minutes to pass for the dye solution to undergo mixing, and for the laser's performance to stabilize. Laser performance typically improves significantly with the addition of the first few aliquots of concentrate. Concentrate should be added until additional affect on the lasers performance is no longer observed. Usually the best performance occurs when the dye solution absorbs ~90 % of the incident 532 nm pump light.

The second step is to optimize the overlap of the 532 nm pump and dye laser spots on the dye cell. The initial phase of this process was described earlier when the position of the pump lens was adjusted for maximum laser power, as monitored by cavity leakage intensity on the FND-100 photodiode. The final phase of alignment is best accomplished by monitoring both the leakage intensity, and by observing the mode quality of the cavity

dumped laser pulse. The latter is easily achieved by projecting the cavity dumped pulse across the laboratory (~ 40') onto a white board. The laser spot should correspond to a TEM_{00} transverse mode profile, *i. e.*, it should be round, symmetrical, and significantly brighter in its center then on its edges. Occasionally we have seen TEM_{10} profiles, however these are easily remedied by adjusting the pump laser steering mirrors.

If the pump laser is too tightly focused, the projected laser spot will display pointing instabilities, *i. e.*, the bright central spot will erratically jump around. This can be corrected by adjusting the *z*-axis position of the pump lens to defocus the pump laser spot on the dye cell. Usually, any movement of the pump lens will require the re-adjustment of the pump steering mirrors. If the dye laser power is low, less than 5 μJ for rhodamine 590, then the position of the intracavity lens may also need to be adjusted, usually in the direction that will decrease the dye lasers spot size on the dye-cell. If this is required then the intracavity lens and the pump lens will need to be adjusted iteratively until optimal laser performance is achieved. Note that when the intracavity lens' position is changed, the *x* and *y*-axis micrometers on the front mirror mount may also require minor adjustments due to slight variations in the cavities optical path.

The final adjustments to the dye laser cavity length need to be made while observing the temporal width of the cavity dumped dye laser pulse. Therefore this adjustment needs to be performed when the entire system is set up to measure the autocorrelation of the dye laser, or the cross correlation of both dye lasers. As discussed above, due to the difficulty in setting up a Michelson Interferometer to measure the autocorrelation, most often we would use the cross correlation arrangement when adjusting the cavity length of the dye lasers. The length of the laser cavity is systematically varied by adjusting the micrometer on the front mirror mount, and the cross-correlation is measured at each position. The cross-correlation typically is only mildly affected by changes in the micrometer setting until the cavity approaches the region close to the ideal length for synchronous pumping by the YAG laser. In this region the

cross-correlation is highly responsive to changes in the micrometer setting. Usually the shortest cross-correlation is also the most symmetric in profile, and can be fit to a Gaussian function. Once both the lasers are adjusted to yield the shortest cross-correlation possible, the cavity lengths will require no further adjustment.

Once the dye lasers are set up and functioning properly at a particular wavelength, then their output characteristics are remarkably consistent for many weeks at a time. Usually the only adjustments that need to be made on a daily basis is a minor adjustment of the 532 nm pump laser steering mirrors. Occasionally the x and y-axis micrometers on the front mirror mount may require minor adjustments, and the dye solutions may require the addition of fresh solvent to replace the loss due to evaporation. The most common problem we have experienced that causes loss of laser power is laser induced degradation of either the dye-cell or the rear mirror. This can be diagnosed by projecting the cavity dumped pulse across the laboratory. If spots appear in the transverse profile of the pulse, or if it is not shaped as a Gaussian TEM_{00} mode, then most likely the problem is a burned spot on the dye cell or on the mirror. This problem can easily be fixed by slightly moving the dye-cell vertically in its mount, or by rotating the rear mirror in its mount.

The wavelength of the dye laser is selected by angle tuning both the 5 μm air-gap etalon, and the 100 μm solid etalon. The best procedure is to remove the 100 μm etalon from the laser cavity (if it is present in the first place), and direct the cavity dumped laser pulse into a monochromator, set at the desired wavelength. The 5 μm etalon is tuned for maximum transmission by the monochromator. The 100 μm etalon is then reinstalled into the cavity, and is also angle tuned for maximum transmission of light through the monochromator. Occasionally, after the 5 μm air-gap etalon has been angle tuned over a large distance, the cavity length may need to be adjusted to account for the difference in the optical path length. Occasionally lasing can simultaneously occur at a satellite band, as well as at the desired wavelength, if two transmission bands of the 100 μm etalon overlapped the transmission band of the 5 μm etalon. This problem can usually be easily

remedied by carefully tweaking both of the etalons, for maximum transmission at the desired frequency.

2.6 References

1. L. R. Khundkar, and A. H. Zewail, Ann. Rev. Phys. Chem. *41*, 15 (1990).

2. The molecular beam was designed by J. J. Breen, P. C. Cong, L. W. Peng, and A. H. Zewail.

3. L. W. Peng, *Ph. D. Thesis, California Institute of Technology,* (1991).

4. M. Kappes,and S. Leutwyler, in *Atomic and Molecular Beam Methods Vol. 1*, ed. by G. Scoles, (Oxford University Press, 1988) p.380.

5. The circuit was built by P. Cong and a diagram can be found in reference 3.

6. These mounts are available from Montford Enterprises, San Diego CA.

7. The exact specifications for these mirrors is proprietary information of the Quantronix Corporation.

8. G. H. McCall, Rev. Sci. Instr. **43**, 865 (1972).

9. F. G. Patterson, *Ph.D. Thesis, Stanford University* (1985).

10. J. C. Postelwaite, J. B. Miers, C. C. Reiner, D. D. Dlott, IEEE J. Quantum Electronics, **24**, 411 (1988).

11. Based on the equations presented in, W.Demtroder, *Laser Spectroscopy, Basic Concepts and Instrumentation*, (Springer-Verlag, Berlin, 1982) p.157.

12. E. D. Potter, *Ph.D. Thesis California Institute of Technology,* 1993, p.20.

13. This manual is available from the Quantronix Corporation, 49 Wireless Blvd., Smithtown, NY 11788.

14. For convenience, the optical axis will be considered the *z*-axis in Cartesian coordinates. The axis perpendicular to the z-axis, but parallel to the top of the laser table will be referred to as the *x*-axis. The axis perpendicular to the laser table will be referred to as the *y*-axis.

15. This manual is available from Quantum Technology, 2620 Iroquois Ave., Sanford Fl, 32771.

Table 1: Spectral tuning ranges for various dye/solvent combinations

Laser Dye	Solvent	Tuning Range	
		Minimum λ (nm)	Maximum λ (nm)
Rhodamine 6G	methanol	550	574
Sulfarhodamine 640	methanol	597	615
Sulfarhodamine 640	methanol/water	605	625
DCM	methanol	622	655
DCM	DMSO	665	687
LDS 698	methanol	690	715

Table 2: The optical characteristics of the dye lasers etalons

Thickness (μm)	Finesse	Resolving Power	$\Delta\lambda$ (at 600 nm)	Free Spectra Range
5	8.76	219	2.74 nm	667 cm^{-1}
100	8.76	4380	0.137 nm	33.33 cm^{-1}

2.7 Figure Captions

1. A schematic of the molecular beam apparatus. This figure was taken from Reference 3.
2. A schematic diagram of the MLQS/ Nd:YAG laser cavity. The measurements given are distances from the center of the particular optical component to the output coupler. Note that this figure is not drawn to scale.
3. Oscilloscope traces of : *a*) the Q-Switch envelope of modelocked pulses, *b*) leakage out of the front mirror of the synchronously-pumped dye laser without the cavity dumper, *c*) same as *b*, except the cavity dumper is activated, d) A cavity dumped visible pulse. Note that in *d* the cavity dumping is not 100 % efficient, giving rise to the residual pulses after the main pulse. All traces were measured using the FND-100 photodiode that is described in the text.
4. A schematic diagram of one of the synchronously pumped dye lasers. The measurements given are distances from the center of the particular optical component to the rear mirror. Note that this figure is not drawn to scale.
5. Two spectra of the probe dye laser (DCM in methanol) showing the bandwidth of the laser when operating both with, and without the 5 μm solid etalon. See the text for details.
6. Schematic overview of the picosecond laser system highlighting the arrangement of the static and variable delay lines of the Michelson Interferometer.
7. Timing diagram as discussed in Section 2.3.3 of the text.
8. A schematic illustrating the alignment procedure for the dye laser optical components as discussed in the text.
9. A schematic illustrating the alignment procedure for the Pockels' cell as discussed in the text.

Molecular Beam Apparatus

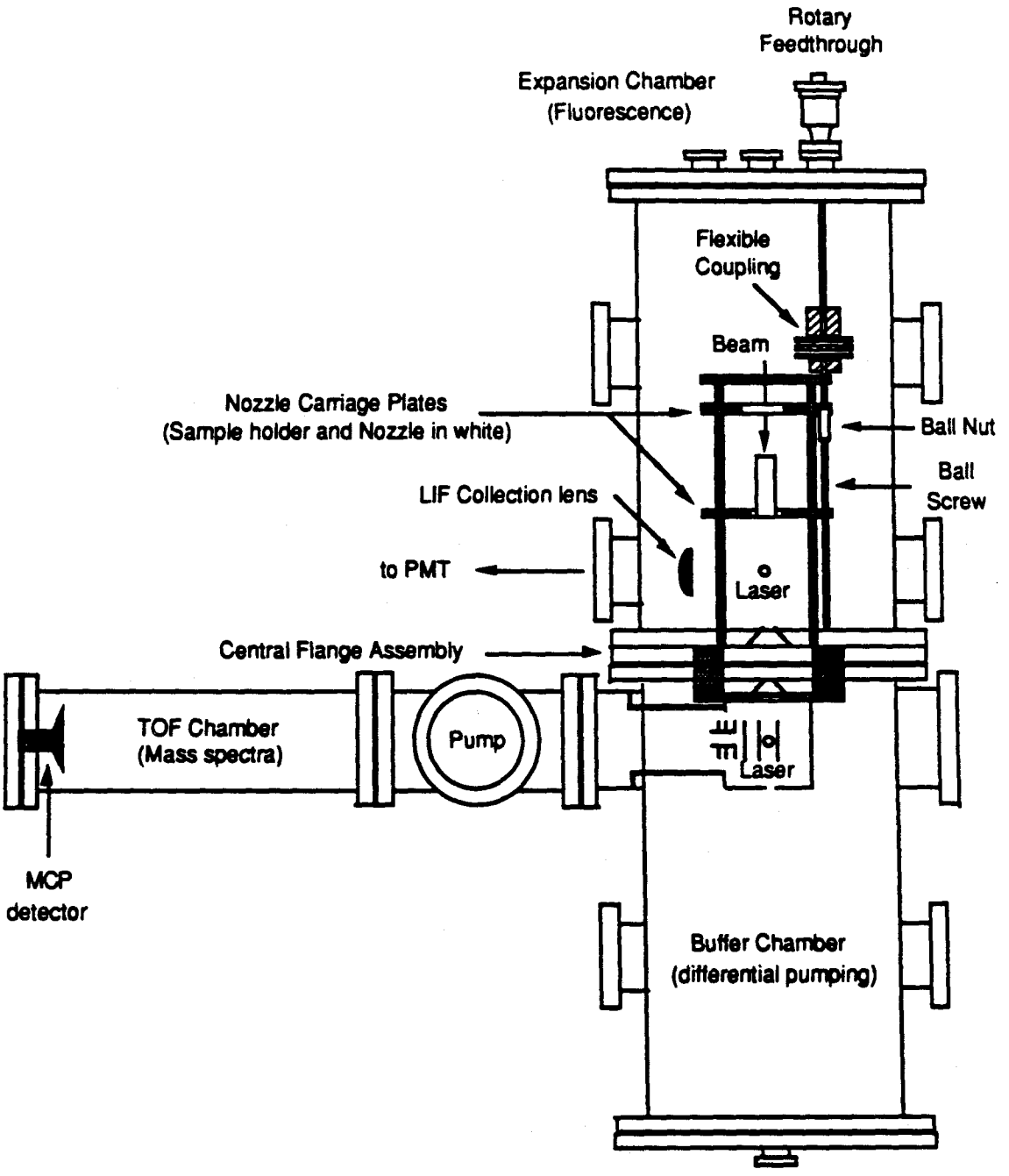

Figure 1

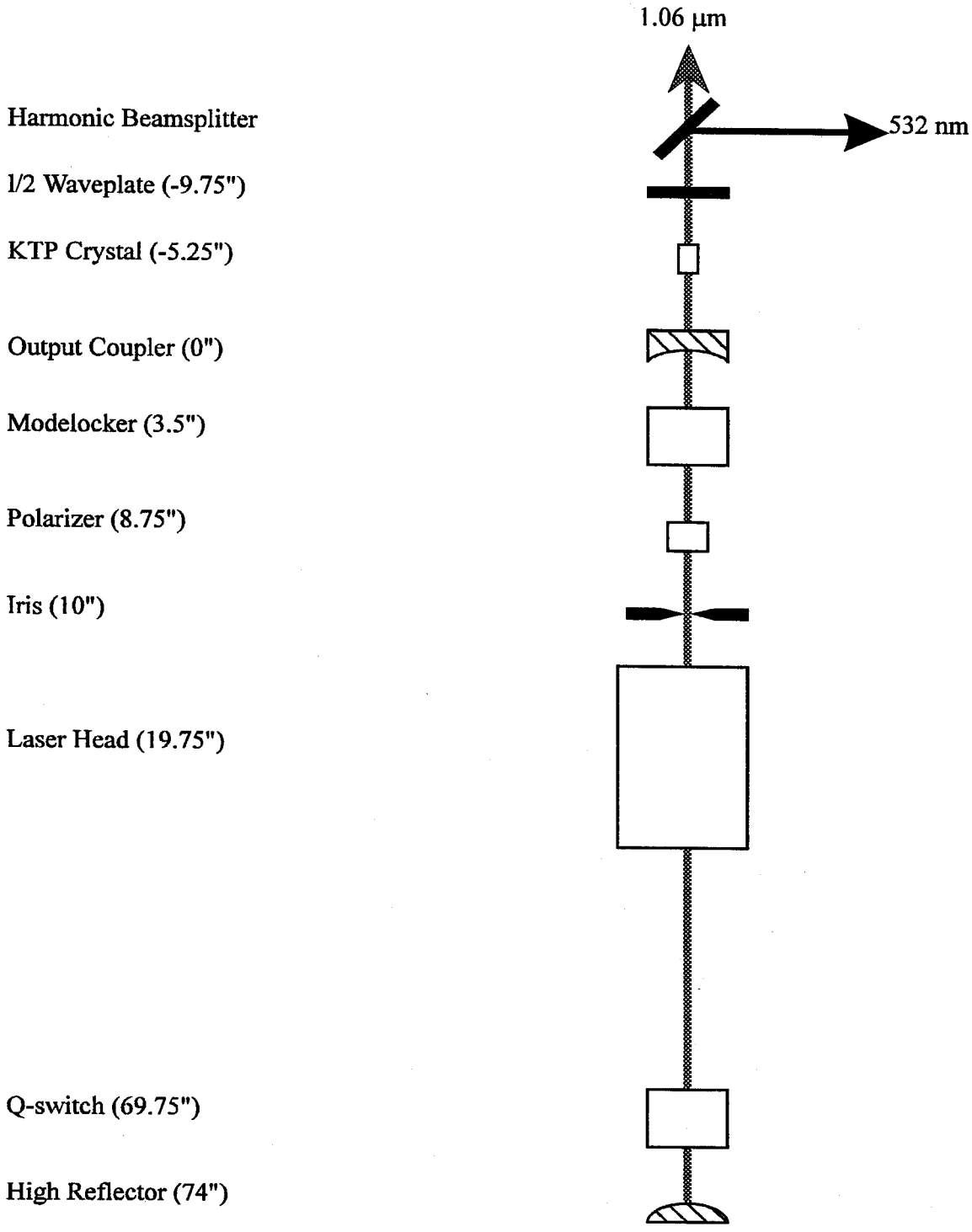
1.06 μm
532 nm
Harmonic Beamsplitter
1/2 Waveplate (-9.75")
KTP Crystal (-5.25")
Output Coupler (0")
Modelocker (3.5")
Polarizer (8.75")
Iris (10")
Laser Head (19.75")
Q-switch (69.75")
High Reflector (74")

Figure 2

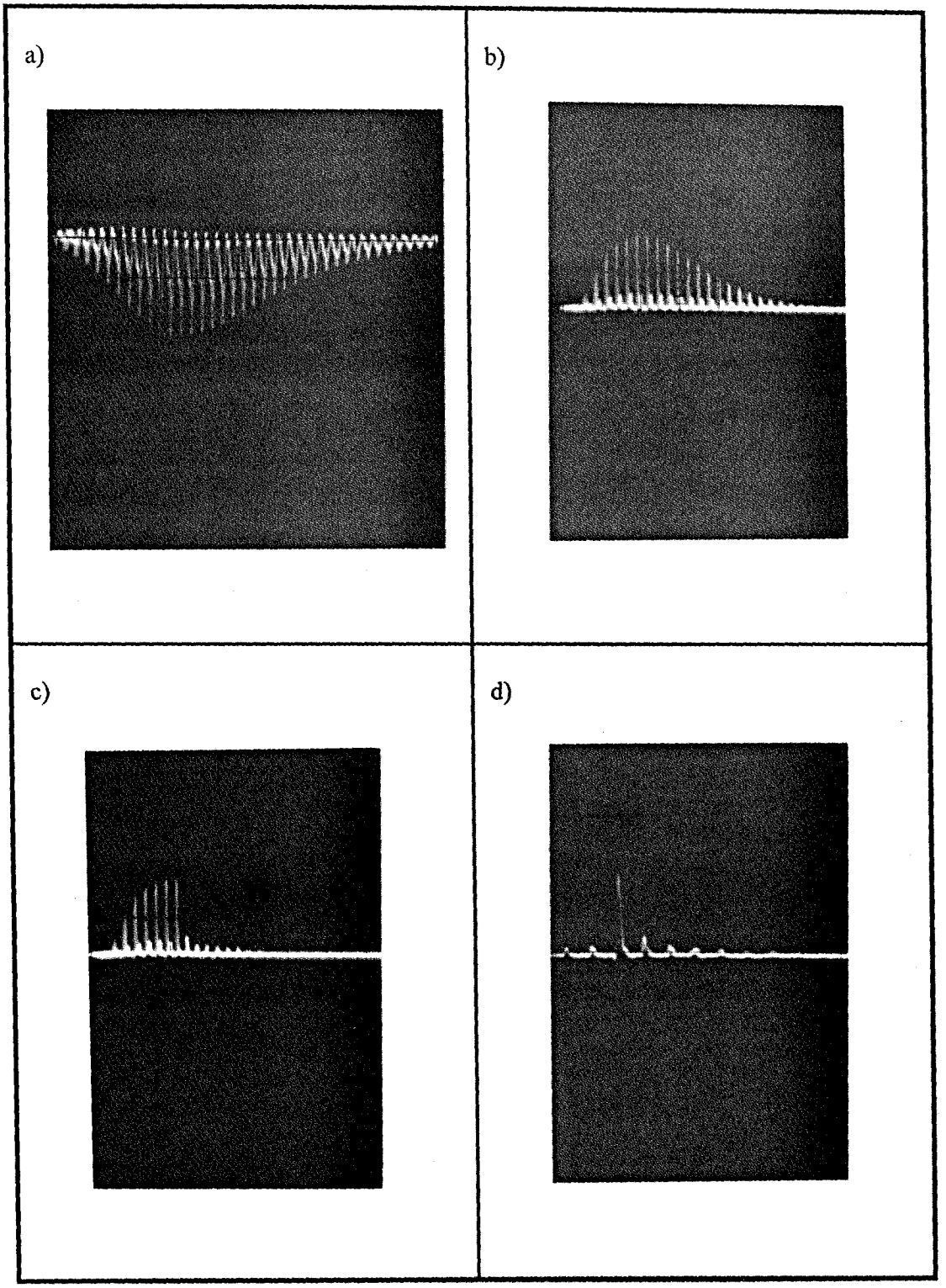

Figure 3

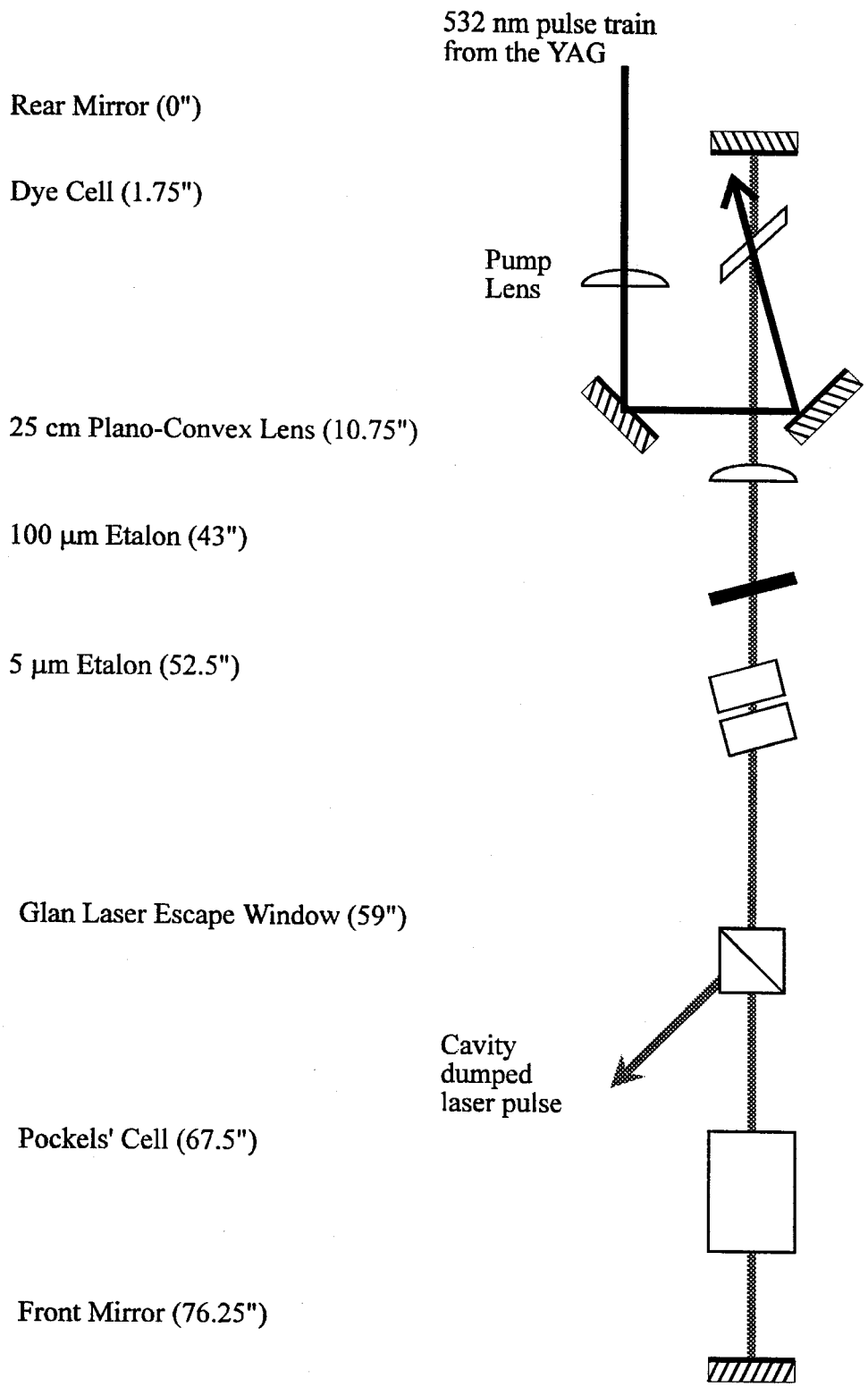
532 nm pulse train
from the YAG
Rear Mirror (0")
Dye Cell (1.75")
Pump
Lens
25 cm Plano-Convex Lens (10.75")
100 μm Etalon (43")
5 μm Etalon (52.5")
Glan Laser Escape Window (59")
Cavity
dumped
laser pulse
Pockels' Cell (67.5")
Front Mirror (76.25")

Figure 4

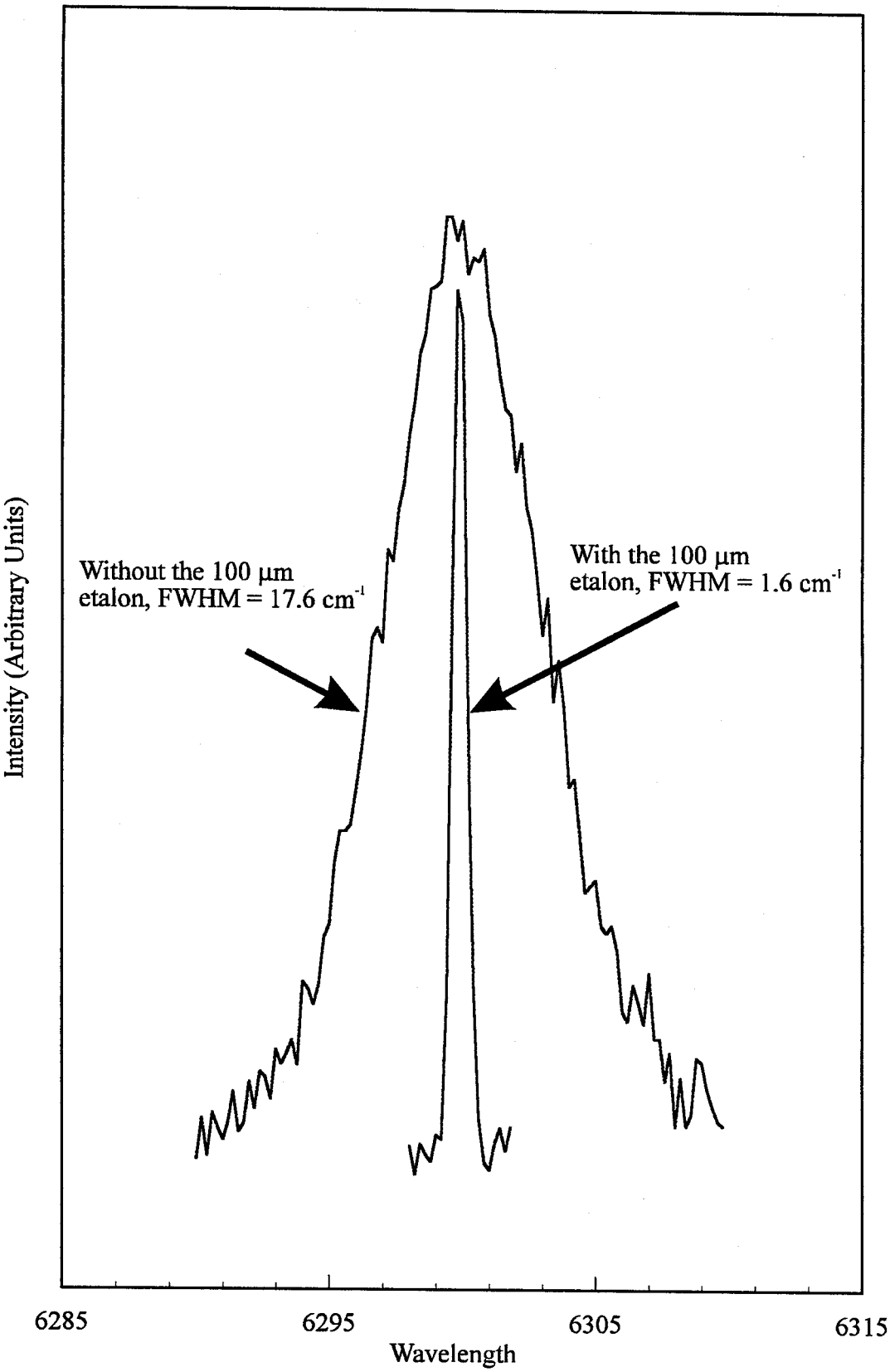
Intensity (Arbitrary Units)
Without the 100 µm etalon, FWHM = 17.6 cm-1
With the 100 µm etalon, FWHM = 1.6 cm-1
6285
6295
6305
6315
Wavelength

Figure 5

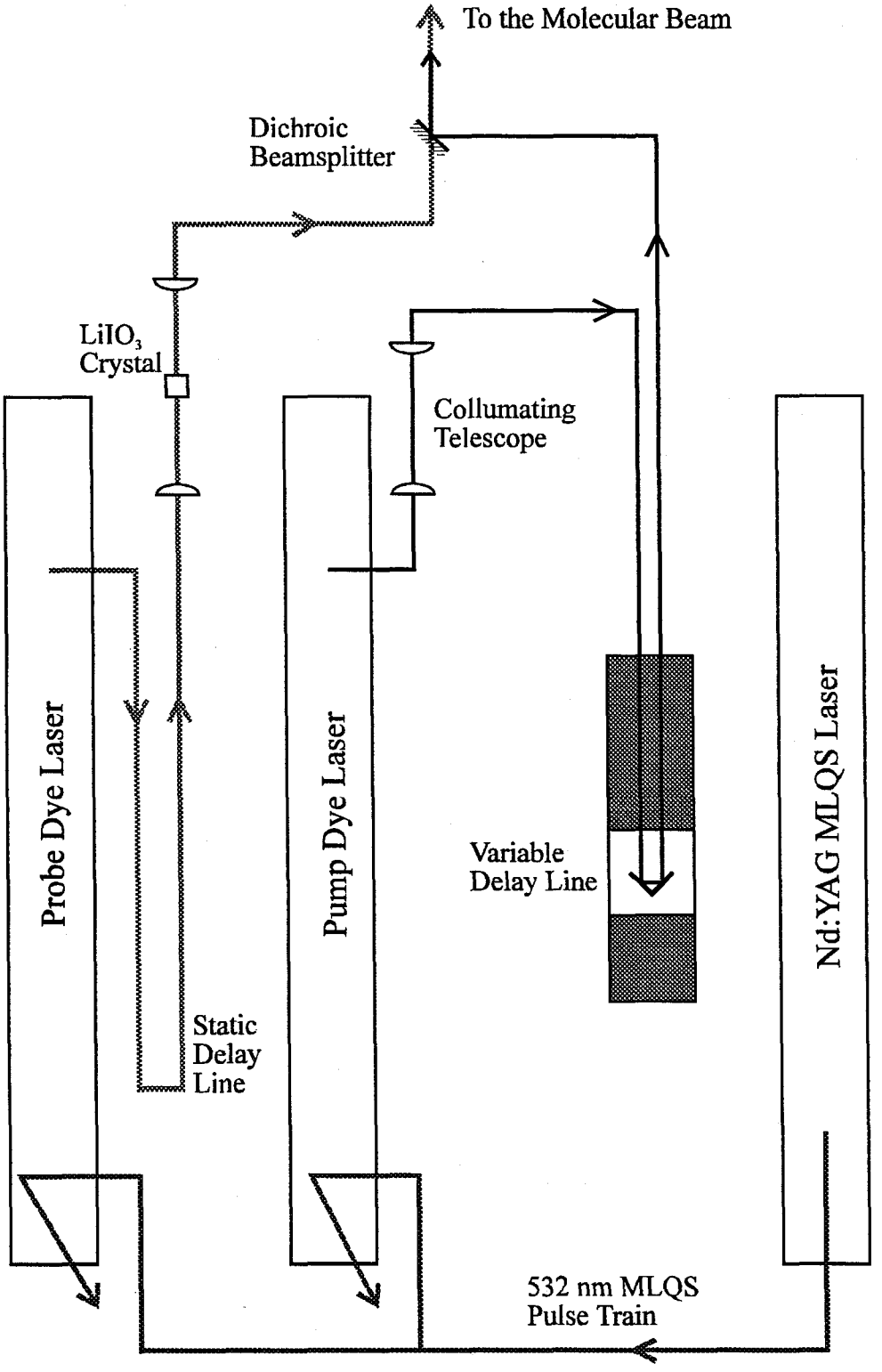
To the Molecular Beam
Dichroic
Beamsplitter
LiIO3
Crystal
Collumating
Telescope
Probe Dye Laser
Pump Dye Laser
Nd:YAG MLQS Laser
Variable
Delay Line
Static
Delay
Line
532 nm MLQS
Pulse Train

Figure 6

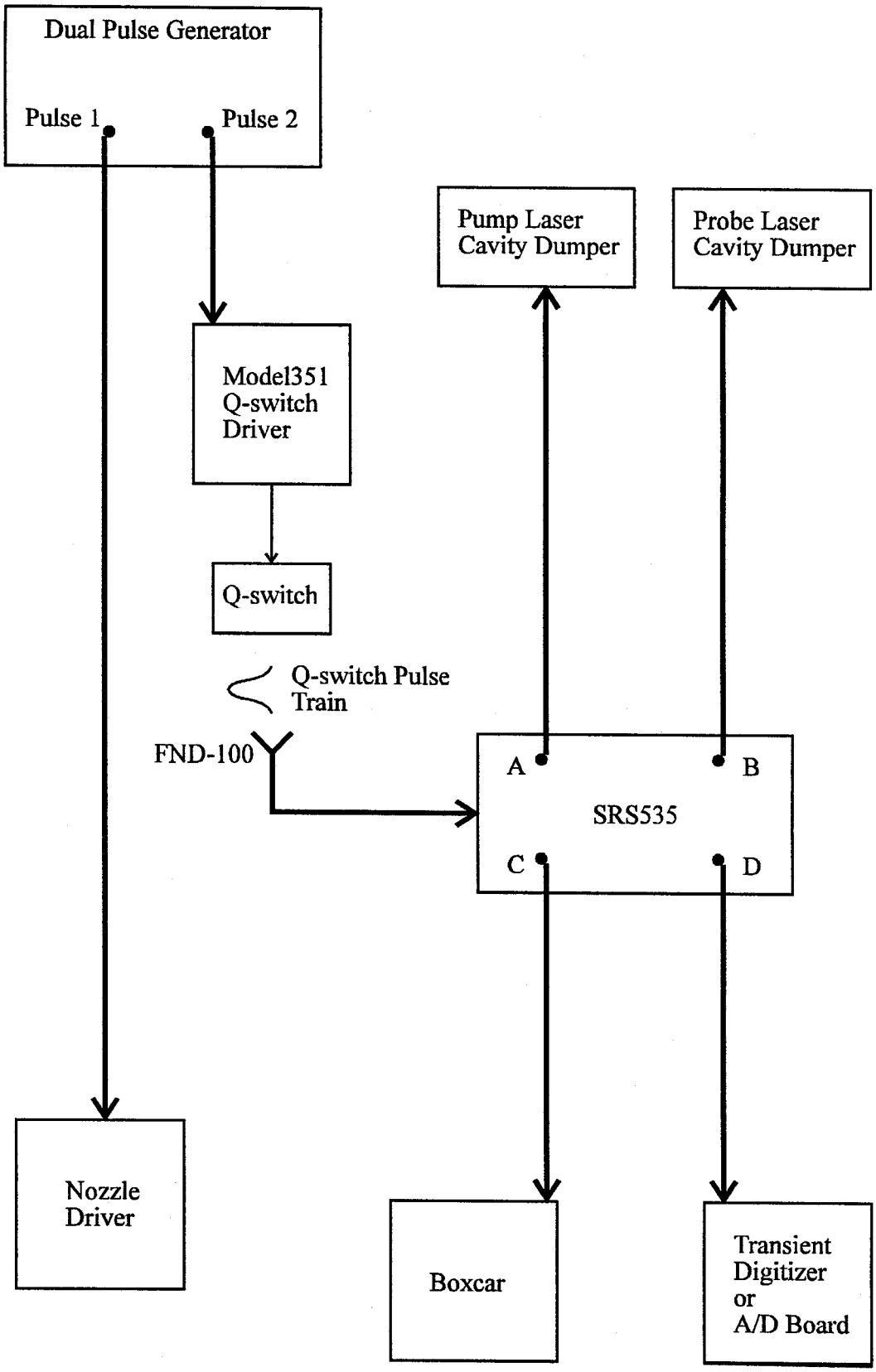
Dual Pulse Generator
Pulse 1
Pulse 2
Pump Laser Cavity Dumper
Probe Laser Cavity Dumper
Model351 Q-switch Driver
Q-switch
Q-switch Pulse Train
FND-100
A
B
SRS535
C
D
Nozzle Driver
Boxcar
Transient Digitizer or A/D Board

Figure 7

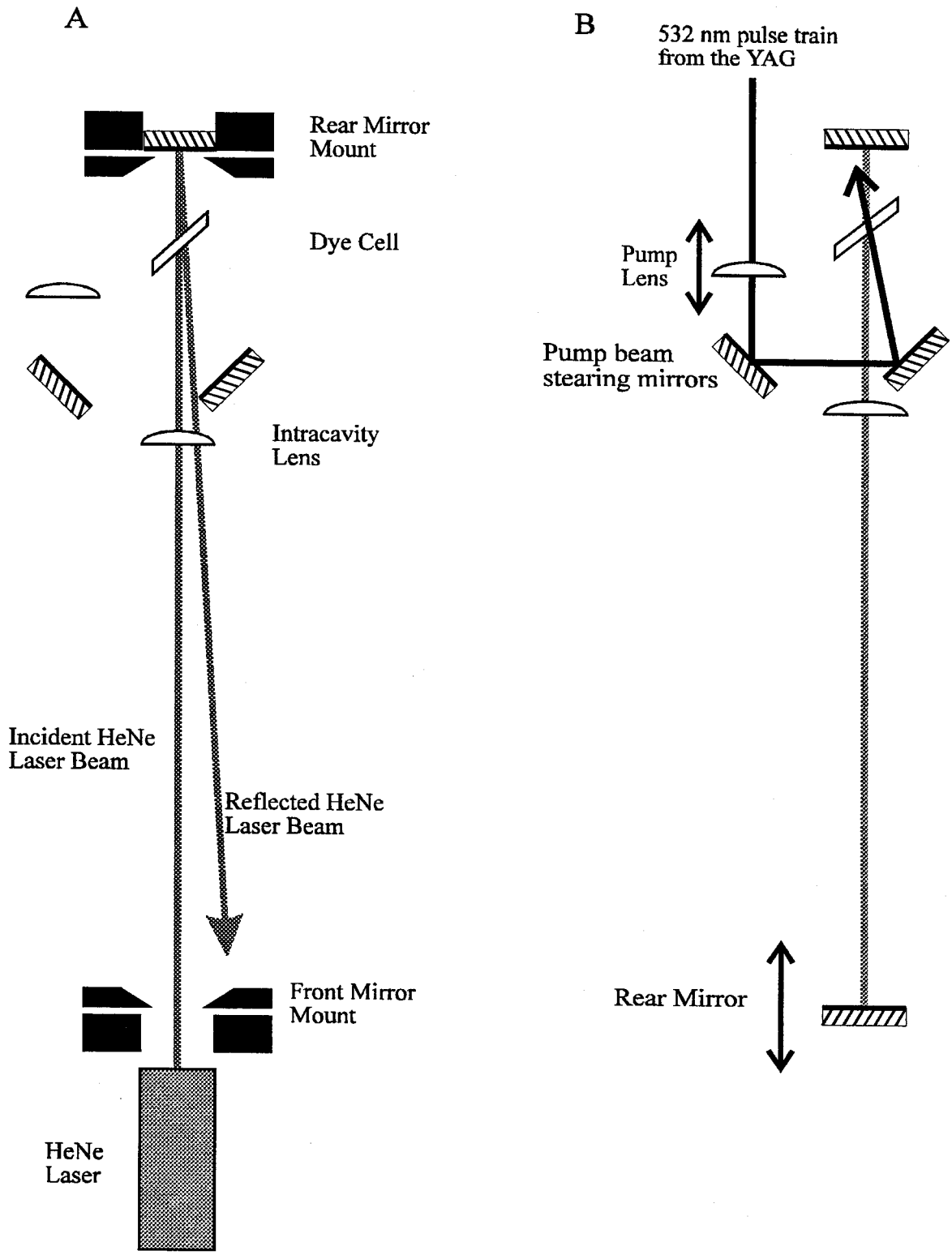
A
Rear Mirror Mount
Dye Cell
Intracavity Lens
Incident HeNe Laser Beam
Reflected HeNe Laser Beam
Front Mirror Mount
HeNe Laser
B
532 nm pulse train from the YAG
Pump Lens
Pump beam stearing mirrors
Rear Mirror

Figure 8

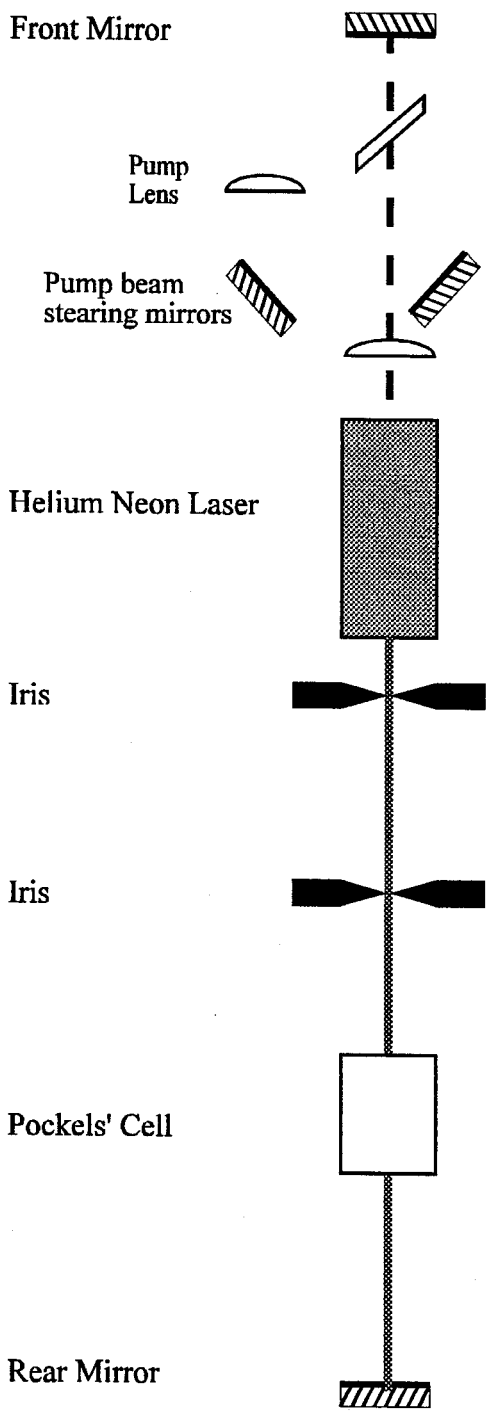
Front Mirror
Pump
Lens
Pump beam
stearing mirrors
Helium Neon Laser
Iris
Iris
Pockels' Cell
Rear Mirror

Figure 9

Chapter III

Real-Time Dynamics of Clusters I. I_2X_n (n = 1; X = Ne, and Ar)

3.1 Introduction

Besides yielding important information on "static" intermolecular interactions (for reviews see Refs.1,2), van der Waals (vdW) clusters are challenging and "simple" systems for understanding reaction dynamics. Of great interest are the questions pertaining to energy redistribution and fragmentation and their dependence on cluster size. It is not obvious that the clusters will be the intermediates between gas-phase and liquid-phase limits of dynamics, but their finite size offers a unique opportunity for testing microscopic and macroscopic theories.

Real-time studies of large vdW complexes have been reported for isoquinoline,[3] tetrazine (in S_1 and S_0),[4,5] phenol,[3] cresol,[3] perylene,[6] stilbene,[3,7] aniline,[8] and $(NO)_2$ (in S_0);[9] recently results have become available for the family of halogens. With nanosecond lasers, the lifetime of ICl-Ne in its A state was measured to be 3 ± 2 ns for $v' = 14$ by the Lester group,[10] and for a large number of systems linewidth measurements have been used to deduce vibrational predissociation lifetimes (for recent reviews see Refs. 11-13). Even for small clusters there remain unanswered questions, especially on how the intermolecular potential influences the dynamics of predissociation. For example, as discussed below, I_2Ne undergoes vibrational predissociation in its excited vibronic states; while I_2Ar undergoes both vibrational and electronic predissociation in the equivalent states.

In the real-time picture, the time scales for the different motions and interactions are relevant to the dynamics. The vibrational period (τ_v) of the I_2 wavepacket in the B-state is typically 300 fs in the region of interest here.[14] The available energy for a change of one quantum in the I_2 vibration, between the initial and final states of the I_2Ne system (v'_i=19, v'_f=18), translates to a typical velocity of about 130 m/s. With a repulsive distance scale of $L \sim 0.5$Å one obtains a "half-collision" time $\tau_c \sim 380$ fs. The ratio of τ_c/τ_v reflects the adiabaticity of the half-collision, and L plays an important role in the outcome of I_2 energy relaxation. As τ_c decreases, the (non-adiabatic) energy transfer

becomes more efficient since the change of force is large during this short time. The state-to-state rates are characterized by times much longer than τ_c and τ_v.

This chapter gives a fuller account of a communication[15] published by this group which reported our first study of the small clusters of iodine/rare gas systems in real-time. When there is only one rare gas atom, I_2X (X=Ne,Ar), the focus is on the processes of intramolecular vibrational-energy redistribution (IVR), vibrational predissociation (VP), and their relationship to the nature of the binding van der Waals potential. In the following chapter,[16] we present our findings for I_2X_n (n>1).

These small clusters are ideal for studies of VP and IVR for a number of reasons. First, the vibrational dynamics (the I_2 stretch, the van der Waals stretching mode, and the van der Waals bending mode) are well defined. As this is a relatively simple system, there are a variety of theoretical models (quantum and classical) which may be formulated and tested with the experimental results. Second, elegant and comprehensive spectroscopic studies are available on these systems.[17-23] Third, the I_2 real-time dynamics on the femtosecond-picosecond time scales have already been reported.[14] Finally, unlike the case of large molecules, theory is quite advanced for these smaller systems (*vide infra*), and there is hope for detailed understanding of IVR and VP.

Frequency-domain spectroscopic studies of I_2X_n (where X = He, Ne, and Ar; $n \geq 1$) give the spectral shift of the $B \leftarrow X$ transition of I_2X to be 6.65 cm^{-1} for neon, and 13.26 cm^{-1} for argon[17] (note that this shift varies slightly with v'). The state-to-state channels by which VP occurs have also been determined.[18-20] The primary channel for I_2Ne is given in equation (1):

$$I_2Ne^*(v'_i) \xrightarrow{k(v'_i,v'_f)} I_2^*(v'_f = v'_i - 1) + Ne \qquad (1)$$

where the asterisk denotes the electronically excited B-state. The situation for I_2Ar is different due to the presence of both electronic and vibrational predissociation channels, as

discussed below. By performing channel-closing experiments — determining at which values of v'_i various channels were opened or closed — Levy and coworkers were also able to obtain the van der Waals bond energies of the different clusters.[21]

The first step in equation (1) is the absorption of a photon which prepares the cluster in a well-defined vibrational level v'_i of the I_2 stretching mode. This is followed by energy redistribution from this mode into the van der Waals stretching mode. In the case of neon, the energy of one quantum of the I_2 stretching mode exceeds the van der Waals binding energy of the complex. Therefore, energy redistribution results in fragmentation, with I_2 being in its B (v'_i-1) vibronic state, and the excess energy converting into translational kinetic energy and rotational energy of the nascent I_2. Figure 1 shows this process schematically. The theoretical models, which assume an exponential type repulsion at short I_2-X separations and R^{-6} interactions at long range, predict that the coupling of the I_2 vibrations to the van der Waals stretch coordinate is highly dependent on the initial value for v'_i. As the VP state-to-state rate is directly determined by this coupling, the rates are highly dependent on v'_i.

In order to understand the coupling involved in VP, it is necessary to accurately determine the rates of VP as a function of the initial quantum number v'_i. Levy and coworkers have estimated the VP lifetimes from linewidth measurements.[19,22] Linewidth measurements provide an upper limit for the rate of VP as they are often contaminated by unresolved substructure (only with I_2He are the rotational bands resolved[23]). One may deduce the lifetimes, in the absence of pure dephasing processes, if the transition is homogeneously-broadened,[24,25] but homogeneous broadening reflects only the initial step of the dynamics. To observe VP, the state-to-state rates must be measured.

The real-time measurements presented here for I_2Ne and I_2Ar are compared with different theoretical models to test their predictions of the absolute magnitudes of the state-to-state rates and their dependence on energy and the quantum state excited. For I_2Ne the measurements are made over the range $v'_i = 13$ to $v'_i = 23$, and the rates range

from 4.6×10^9 s^{-1} to 1.89×10^{10} s^{-1}. For I_2Ar the total rates are 1.30×10^{10} s^{-1} (v'_i=21) and 1.43×10^{10} s^{-1} (v'_i=18), and the electronic predissociation rate is comparable to the VP rate.

This chapter is outlined as follows: In Section 3.2 the experimental procedure is described in detail. A thorough description of the laser and molecular beam apparatus has already been presented in Chapter II, therefore we will focus on those elements of the experimental apparatus and methodology that are specific to this experiment. The results of these experiments are presented in Section 3.3 and are discussed in conjunction with the relevant spectroscopic investigations and theoretical models. In Section 3.4, an account of the studies of the I_2Ar system is presented, and the chapter is brought to a conclusion in Section 3.5.

3.2 Experimental

The experiments were performed using a combination of picosecond laser and molecular beam techniques. To measure the state-to-state VP rates as a function of the vibrational quantum number v'_i, two color (pump-probe) laser pulses were employed. The first laser pulse (the pump) excited the iodine to a given v'_i of the B electronic state,[26-28] covering the range v'_i=13-23. For the majority of the vibrational states studied, dye solutions of rhodamine 590 (Exciton) in methanol were used for the pump laser, except for v'_i=13,14, where rhodamine 610 (Exciton) in methanol was used. The second laser pulse (probe), which was delayed in time from the first, was tuned to the $f \leftarrow B$ transition of the nascent I_2^* produced by predissociation. DCM (Exciton and Kodak) in DMSO was used as the dye solution in the probe laser for all of the vibrational levels studied. Ultraviolet fluorescence from the I_2 f ion-pair state was measured as a function of the delay time between the pump and probe laser pulses. As the delay was varied, the resulting transient yielded the risetime of the nascent $I_2^*(v'_f=v'_i-1)$. Temporal resolution in experiments of this nature is limited only by the cross-correlation of the pump and probe

laser pulses.[3] The laser system used in these experiments had a cross-correlation (FWHM) of 40 ± 3 ps, with an approximately Gaussian profile.

The I_2Ne complexes studied were formed in a free jet expansion of neon (99.996% purity, Spectra Gases Inc.) which had been seeded with iodine (99.999% purity, Aldrich) at room temperature vapor pressure. Two different nozzles were used, a cw glass nozzle for I_2Ne v'_i = 16-21, and a General Valve Series 9 pulsed solenoid valve for v'_i = 13, 14, 22, 23. The glass nozzle was home-built and had an orifice diameter of 75 μm. The nozzle was heated to 43 °C to avoid clogging with I_2. The pulsed nozzle had a conical cross-section for maximum cluster formation, with a nozzle diameter of 150 μm. The pulsed nozzle was not actively heated during the experiments performed in the studies reported here, however, as it was operated, it reached an equilibrium temperature of approximately 45 °C.

Since the expansion contained both bare iodine and larger complexes of I_2Ne_n (where $n > 1$), as well as I_2Ne, selective excitation of the desired complex was important. The spectroscopic measurements published by Levy and coworkers proved invaluable in this regard. It was shown that for the I_2Ne_n complexes, where $n < 7$, the $(B,v') \leftarrow (X,v''=0)$ transition is blue shifted ($n \times 6.65$ cm^{-1}) from the corresponding bare I_2 transition.[17] The lasers used in our experiments had a bandwidth of 3 cm^{-1}, and it was possible to selectively excite a given cluster size.

The experimental scheme for the I_2Ar studies was essentially the same as described for I_2Ne, and has been described briefly in an earlier communication.[15] The conditions were as follows. An approximately 20% mixture of Ar in He was seeded with iodine (99.999% purity, Aldrich) at its room temperature vapor pressure. The mixture was expanded through a heated (43 °C) continuous glass nozzle (d=75 mm). The backing pressure was typically 20 psi, and x/d was kept at about 75.

A number of test experiments were performed. First, prior to each I_2Ne (v'_i) scan, an I_2 (v'_i-1) scan was taken. In the latter, the pump laser was tuned to the uncomplexed

$B(v'_i\text{-}1) \leftarrow X(v''=0)$ transition, while the probe laser was set for the same transition used in the I_2Ne scan. As in the I_2Ar cluster $v'_f = v'_i\text{-}3$, a corresponding $I_2(v'_i\text{-}3)$ scan was made for this system. These tests ensured the correct probe laser wavelength, as well as proper alignment between the pump and probe lasers. Second, UV fluorescence was shown to decrease as the pump laser was detuned either to the red or to the blue of the I_2X (X = Ne,Ar) absorption maximum, indicating that the signal was not due to the "tail" of a bare iodine transition. Third, the molecular beam conditions were varied: signal intensity was found to be highly dependent on the stagnation pressure behind the nozzle (as expected for van der Waals clusters), and no signal was observed when pure helium was used as the carrier gas. Finally, multiple transients were obtained for each vibrational level to ensure the accuracy of the measurements.

3.3 Results and Discussion

3.3.1 State-to-State Rates

Figure 3 shows transients for three of the vibrational quantum numbers, $v'_i = 13$, 18, and 23. The time constants (τ) were extracted from the transients by fitting them to an exponential rise, including a convolution with the Gaussian system response function. The fitting procedure was based on a Marquardt non-linear least squares fitting routine.[29] For all transients reported, no parameters were fixed other than the cross-correlation bandwidth. The value of time zero obtained from these transients corresponded well to that obtained from bare I_2 control scans; there was no evidence of an induction period in the case of I_2Ne, within our time resolution. The measured τ, as a function of v'_i, are shown in Figure 4 and are listed in Table I. Note that the errors listed are the standard deviations of all values obtained for a given v'_i.

An interesting feature observed in the $v'_i = 22\text{-}23$ transients was the appearance of rotational recurrences corresponding to nascent $I_2^*(v'_i\text{-}1)$, as can be seen in Figure 5. For all of the transients measured, the pump and probe lasers had parallel polarizations and the

rotational recurrences observed were found to be in accord with this arrangement. When I_2Ne was pumped to $v'_i = 23$ and the product I_2^* was probed in $v'_f = 22$ the spacing between the in-phase and out-of-phase recurrences was found to be 336 ± 5 ps. This corresponds to a rotational constant of 0.02483 cm^{-1}, which is in good agreement with the literature value of 0.02485 cm^{-1} for I_2 in the $v' = 22$ vibronic state.

For these values of v'_i, the process of VP is relatively fast so that rotational coherence of the sampled population is preserved. This is an important result when considering the effect of rotations on VP. At the rotational temperature of the beam (~ 4 - 5 K), a number of rotational levels are excited in any given vibronic state. Most theoretical models neglect the role of rotationally-excited states on the rate of predissociation. The observed rotational recurrences indicate that there is a separation between the timescales of VP and of the rotational motion.

As mentioned above, Levy and coworkers have estimated the predissociation lifetime of I_2Ne in various vibrational levels from linewidth measurements.[19] Their reported estimates, along with the τ-values measured in the real-time experiments, are shown in Figure 4. The value obtained by linewidth measurement for $v'_i = 14$ is significantly shorter than the value obtained in our experiment. As has been previously noted,[19] linewidth measurements of I_2X systems are difficult to unravel due to inhomogeneous broadenings; the rotational congestion is one contribution. The linewidth estimate of τ, therefore, represents an upper limit for the corresponding rate, and this is a possible reason for the differences between Levy's results and ours. The reported errors for the linewidth estimates are large, and it is difficult in this case to establish the functional form for the v'-dependence of VP. The values obtained in real-time have errors typically less than ten percent of the magnitude of τ, and they show clearly that the v'_i-dependence is monotonic, but highly non-linear, over the range of v'_i measured.

The rate of vibrational predissociation $k(v'_i, v'_f)$ in equation (1) is taken as the inverse of the measured τ. The obtained rates are listed in Table 1, and the v'-dependence

of the rates is shown in Figure 6. The available energy for the predissociation process in Equation (1) is defined here as the energy released from one quantum of the I_2 vibrational stretch. Due to the anharmonicity of the I_2 B-electronic state potential surface, the energy available for predissociation decreases as v'_i increases. As can be seen in Figure 7, the rate of predissociation is inversely proportional to the available energy. More on these findings will be discussed in the following section.

3.3.2 Comparison with Theory

The VP of van der Waals complexes consisting of a diatomic molecule B-C and a rare gas atom X has been the subject of many theoretical studies during the last decade.[30–55] Realizing that VP can be described as a half-collision process, the advanced methodology of scattering theory can be applied, as has been done by Beswick, Jortner (BJ) and co-workers.[30-33] Their treatment of VP essentially considers the decay of a bound complex state into a set of coupled translational continua.

The relevant coordinates for a description of VP are the intramolecular coordinate r of the diatomic fragment and the inter-molecular coordinate R (the distance between the rare gas atom X and the center of mass of the B-C molecule, frozen in its equilibrium distance r_0). If rotational and bending motions are considered, the angle θ between these coordinates has to be varied as well.

The coupling of the vibrations along these coordinates is given by $V(r,R)$, and the full van der Waals potential $U(r,R)$ can be written as:

$$U(r,R) = U(r_0,R) + V(r,R). \qquad (2)$$

With this separation, the zero-order Hamiltonian gives a separable basis set; the diabatic bound states in this frozen approximation are direct products $|v'_i\rangle|l'\rangle = |v'_i\, l'\rangle$, where v'_i labels the quantum state of the oscillation along r [with energy $E_{BC}(v')$] and l' that of the

vibration along R (with energy $\varepsilon_{l'}$). The diabatic continuum states are direct products $|v'_f\rangle|\varepsilon'\rangle = |v'_f\ \varepsilon'\rangle$, where ε' denotes the energy-normalized continuum state describing the fragments B-C and X flying apart with relative kinetic energy ε'. The corresponding energies are $E_{BC}(v'_i) + \varepsilon_{l'}$ for the bound states and $E_{BC}(v'_f) + \varepsilon'$ for the continuum states.

Assuming that only the discrete states of the electronic B-state are connected to the ground state of the molecule by a non-vanishing optical transition moment, the initial state at time zero can be assumed to be prepared in $|v'_i\ l'\rangle$. This initial state decays into the continuum exponentially with a lifetime:

$$\tau = (\hbar/2\Gamma);\ \ \tau^{-1} = k(v'_i, v'_f). \tag{3}$$

As VP of the systems considered here is much faster than the radiative decay, Γ (in energy units) is the HWHM of the dissociation resonance.

By neglecting both the discrete-discrete state and continuum-continuum state coupling, and by assuming that the residual coupling is small compared with the energy spacing between the discrete levels (i.e., neglecting interference effects between resonances), BJ arrived at the golden rule expression:[30]

$$\Gamma = \pi\left|\langle v'_i, l'|V|v'_f, \varepsilon'\rangle\right|^2, \tag{4}$$

describing VP into the channel $|v'_f\ \varepsilon'\rangle$. Neglecting the usually small level shifts introduced by the coupling operator, energy conservation implies:

$$\varepsilon' = E_{BC}(v'_i) + \varepsilon_{l'} - E_{BC}(v'_f). \tag{5}$$

Expanding $V(r,R)$ about the equilibrium value r_0 and retaining only the linear terms in $(r - r_0)$, BJ separated the golden rule expression (4) into an intramolecular term (A) and an intermolecular term (B):[30]

$$\Gamma = \pi AB\,, \tag{6}$$

with

$$A = \left|\left\langle v'_i \left| r - r_0 \right| v'_f \right\rangle\right|^2 \tag{7}$$

and

$$B = \left| \left\langle l' \left| \left(\frac{\partial U}{\partial Q}\right)_{r_0} \right| \varepsilon' \right\rangle \right|^2 . \tag{8}$$

For a harmonic B-C potential the intermolecular term does not depend on the quantum number v'_i since the recoil energy is the same in all v'_i states. The v' dependence of Γ arises from A being proportional to v'_i. From the properties of the operator r, the propensity rule $\Delta v = -1$ follows from equation (7). Even for an anharmonic potential the propensity rule is valid to a first-order approximation,[30] and the A term is proportional to v'_i as long as $v'_i < K_{BC}$, where

$$K_{BC} = \omega_{BC} / [2(\omega x_e)_{BC}]. \tag{9}$$

ω_{BC} is the intramolecular vibrational frequency and $(\omega x_e)_{BC}$ is the corresponding anharmonicity. As BJ pointed out,[30] K_{BC} is large (82.2 for I_2), so for most experiments the above relations are fulfilled.

For a linear X·····B-C bound by a Morse potential,[30]

$$U(Q) = D_{XB}\left\{\exp[-2\alpha_{XB}(Q-Q_0)]-2\exp[-\alpha_{XB}(Q-Q_0)]\right\}, \qquad (10)$$

where the distance between B and X is denoted by Q and its equilibrium value by Q_0 (note that Q is different from, but related to, R). The key parameters and relations needed in describing the physics of the problem are given in Table II (see Ref. 30).

For a linear geometry, BJ derived an analytical formula for the VP rate [diabatic distorted wave (DDW) approach]. In the limit $\theta_{\varepsilon'} >> 1$ and taking $v'_f = v'_i - 1$, they obtained:

$$\Gamma = \pi^2 \hbar \omega_{BC} \mu g(N,l') \times \frac{(2K_{BC}-2v'_i+1)(2K_{BC}-2v'_i-1)}{[2K_{BC}(2K_{BC}-v'_i)]} \times \theta_{\varepsilon'}^{2N-1} v'_i \exp(-\pi\theta_{\varepsilon'}) \qquad (11)$$

where μ is the mass ratio $\mu_{X,BC}/\mu_{BC}$ and $g(N,l') = (N-l'-1)/[l'!(2N-l'-1)!]$.

From this expression, some simple physically intuitive relations can be derived. For large values of $\theta_{\varepsilon'}$, the exponential in expression (11) is dominant, yielding:

$$\Gamma \propto \exp\left[-\pi\left(2\mu_{X,BC}\,\varepsilon'\right)^{1/2}/(\hbar\alpha_{XB})\right], \qquad (12a)$$

or equivalently,

$$\Gamma \propto \exp\left[-2\pi\left(D_{X,B}\,\varepsilon'\right)^{1/2}/(\hbar\omega_{XB})\right]. \qquad (12b)$$

Energy conservation in (5) leads to:

$$\varepsilon' = \left[\hbar\omega_{BC}\left(1 - v'_i / K_{BC}\right)\right] - \left[D_{XB} - (\hbar^2 \alpha_{XB}^2)(K_{XB} - l' - \tfrac{1}{2})^2 / (2\mu_{X,BC})\right] \quad (13)$$

where the first term in square brackets corresponds to the energy difference between the initial and the final state of the I_2 intramolecular vibration, while the second term is the energy of the excited van der Waals vibration with respect to D_{XB}.

From expressions (12) and (13), it can be seen that as the energy difference between levels v'_i and v'_f matches the van der Waals stretch energy of level l' (i.e., $\varepsilon' \rightarrow 0$), Γ increases. This relation is referred to as the energy-gap law. It also explains why the VP rates are so dependent on the nature of the diatomic B-C in the complex. Equation (12) also reveals the momentum-gap law obtained by Ewing.[34-37] Because the translational momentum p is given by

$$p = (2\mu_{X,BC}\varepsilon')^{1/2}, \quad (14)$$

equation (12) may be rewritten as:

$$\Gamma \propto \exp\left[-\pi p / (\hbar\alpha_{XB})\right]. \quad (15)$$

It is now possible to obtain an expression giving the dependence of the VP rate on the vibrational quantum number v'_i. If the second term on the right-hand side of equation (13) approaches zero, we can write:

$$(D_{XB}\varepsilon')^{1/2} = [D_{XB}(\hbar\omega_{BC})]^{1/2}(1-v'_i/K_{BC})^{1/2}$$
$$= [D_{XB}(\hbar\omega_{BC})]^{1/2}[(1-v'_i/(2K_{BC})]. \quad (16)$$

In this case, the VP rate, including the intramolecular factor v'_i (according to the A term of equation (6) which is obtained from equation (11) when $K_{BC} >> v'_i$), leads to:

$$\Gamma \propto v'_i \exp(\gamma v'_i), \quad (17)$$

where

$$\gamma = \pi[D_{XB}(\hbar\omega_{BC})]^{1/2}/[K_{BC}(\hbar\omega_{BC})]$$
$$= \pi[\mu_{XB}(\hbar\omega_{BC}/2)]^{1/2}/[K_{BC}(\hbar\alpha_{BC})]. \quad (18)$$

The derivation of equation (17) should, however, fail if the energy $\varepsilon_{l'}$ cannot be neglected relative to the energy difference between levels v'_i and v'_f. In other words, if the energy difference of v'_i and v'_f is much larger than the bound van der Waals level energy, then expression (17) is valid, and we only have the intramolecular effect (v'_i of the pre-exponential A term) and a simple exponential. Γ should show a nonlinear dependence on the quantum number v'_i due to the anharmonicity of the B-C bond, even if ε'_l is included.

Within a semiclassical approach,[38] equation (17) can be derived. The intermolecular term is approximated by a "free-free" transition between different states of the relative motion of the two fragments. In this semiclassical approach it is assumed that the repulsive part of the potential is responsible for the energy exchange between the fragments. This assumption is essentially in line with a highly excited van der Waals state of the complex, i.e., neglecting the potential well. The half-collision can then be related to a full collision, and the length parameter L mentioned in the introduction is a key parameter to the early time dynamics.

Recently, simple expressions for VP rates, like the momentum-gap law, have been critically reviewed.[39] The authors performed model calculations which showed that the momentum-gap law can lead to severe failure when sufficiently high quantum numbers v'_i are involved.

The D_0 value of the I_2Ne van der Waals bond has been measured to be approximately 65-67 cm^{-1},[21] while the available energy for dissociation varies between 104.4 cm^{-1} for $v'_i = 13$, and 85.6 cm^{-1} for $v'_i = 23$. Therefore, for the values of v'_i studied in this experiment, the amount of excess energy going into the fragmentation process is between 19 cm^{-1} and 37 cm^{-1}, assuming $l' = 0$.

3.3.2a Absolute rate values

Before applying the above mentioned results to the system I_2Ne, a note concerning the approximation is in order. Equation (11), from which the functions important to the VP of I_2Ne are derived, is valid for a cluster geometry assuming a linearized Morse potential in the limit $\theta_{\varepsilon'} >> 1$. With values obtained spectroscopically by Levy and coworkers[21] for the B state of I_2Ne ($\alpha = 1.5$ $Å^{-1}$, $K_{XB} = 6.21$, $D_{0,XB} = 66.05$ cm^{-1}) and the experimental parameters for the I_2 B-state, we obtained $\theta_{\varepsilon'} = 3.55$ for $v'_i = 20$. This value for $\theta_{\varepsilon'}$ is larger than one, but it is not a factor of ten or a hundred larger than one. This may influence the validity limit for using equation (11) for the I_2Ne case.

Calculating the VP rate for $v'_i = 20$ according to the more exact equation (2.B.53) in Reference 30b (from which equation (11) was derived in the limit $\theta_{\varepsilon'} >> 1$) yields $\tau = 2.7$ ps, a value much too small when compared to our real-time result of 78 ps. With the same parameters, one can calculate the VP rate by means of equation (11) and end up with $\tau = 2.8$ ns, a value much too large. Other calculations for nonlinear geometries and close couplings are discussed below [Sections 3.3.2(a) and (b)]. Although both equations do not lead to quantitative agreement with our experimental results, fits of the data to these functional forms may be, at least qualitatively, meaningful. The energy-gap law and

the momentum-gap law have been applied before in the interpretation of VP processes (see *e.g.*, Ref. 56) and it is important to test the predicted trends with experiments.

3.3.2b Momentum-gap law

With the momentum-gap law, we fitted the experimental results to an exponential function according to equation (15):

$$1/\tau \propto \exp(\beta\varepsilon'^{1/2}). \tag{19}$$

The fit, together with our data, is shown in Figure 8(a). From the fit parameter β we obtain an effective Morse parameter $\alpha = 3.94$ Å^{-1}. A reasonable value of α should lie in the range 1-2 Å^{-1}. Taking into account the intramolecular term, an attempt to improve equation (19) was made by fitting to the following expression:

$$1/\tau \propto v_i' \exp(\beta\varepsilon'^{1/2}). \tag{20}$$

Surprisingly, the fit (Figure 8b) yields a worse value of $\alpha = 6.31$ Å^{-1}. Improvement by including the Morse factor [see equation (11)],

$$M(v) = (2K_{BC} - 2v + 1) \times (2K_{BC} - 2v - 1)/[2K_{BC}(2K_{BC} - v)], \tag{21}$$

leads to a fit of the type:

$$1/\tau \propto M(v_i')v_i' \exp(\beta\varepsilon'^{1/2}), \tag{22}$$

and we obtained a value of $\alpha = 4.89$ Å^{-1}. The fit is shown in Figure 8c.

Assuming $l'>0$ the data could be fitted to the functional form (22) with $\alpha = 4.78$ Å^{-1} ($l' = 1$), $\alpha = 4.10$ Å^{-1} ($l' = 2$), $\alpha = 3.76$ Å^{-1} ($l' = 3$), $\alpha = 3.56$ Å^{-1} ($l' = 4$); and $\alpha = 3.45$ Å^{-1} if the van der Waals energy $\varepsilon_{l'}$ is completely neglected in equation (5). Accordingly, higher l'-values tend to shift the parameter α to lower values but by no means into the expected range. The functional form suggested by the simple momentum gap law is not sufficient to obtain reasonable Morse parameters from a fit of the experimental data.

Even though equation (11) has been derived for triatomic van der Waals clusters in a collinear geometry only, the equation may be used to obtain the following functional form when taking into account the effect of higher terms in $\theta_{\varepsilon'}$:

$$1/\tau \propto M(v_i')v_i' \, (\beta\varepsilon'^{1/2})^m \exp(\beta\varepsilon'^{1/2}). \qquad (23)$$

For $m = 8$ ($l' = 0$) we obtain $\alpha = 1.50$ Å^{-1} and for $m = 9$ ($l' = 0$) $\alpha = 1.38$ Å^{-1}. Similar fits were made but without the intramolecular factor, *i.e.*, to

$$1/\tau \propto (\beta\varepsilon'^{1/2})^m \exp(\beta\varepsilon'^{1/2}), \qquad (24)$$

which yield $\alpha = 1.52$ Å^{-1} for $m = 7$ ($l' = 0$) and $\alpha = 1.40$ Å^{-1} for $m = 8$ ($l' = 0$).

3.3.2c Energy-gap law and close coupling

In addition to the momentum-gap law, we next consider the energy-gap law in the limit specified by equation (17), i.e.,

$$1/\tau \propto v'_i \exp(\gamma v'_i). \qquad (25)$$

From the parameter γ we extract $\alpha = 2.45$ Å^{-1}. The fit is shown in Figure 9(a). To test the uniqueness of the fit we also attempted a simpler exponential form,

$$1/\tau \propto \exp(\gamma v'_i), \tag{26}$$

which yields $\alpha = 1.53$ Å^{-1} [Figure 9(b)]. A polynomial fit including linear, quadratic, and cubic terms is shown in Figure 9(c). From Figure 9, it is clear that the VP rate shows a definite nonlinear dependence on the vibrational quantum number v'_i as has been predicted by theory, independent of the different functional forms suggested by different limits.

Using the full Morse potential,[30,33] BJ performed numerical model calculations for linear triatomic van der Waals complexes and showed that the results were in line with the qualitative energy-gap law. They found that the dependence of the VP rate on the van der Waals quantum number l' is such that the rate increases with l' up to a maximum and then decreases. If the van der Waals potential can only hold very few (*i.e.*, two) bound states, the rate decreases with l'. BJ also went beyond the golden rule approximation, *i.e.*, included continuum-continuum interactions.[30] Intercontinuum interactions result in relaxing the propensity rule $\Delta v = -1$ and allow different v'_f channels to be open, particularly for high v'_i quantum numbers.

The geometry of I_2Ne is most likely T-shaped,[19] and the influence of any anisotropy in the potential, including effects of the bending motions and rotation, on the rates has not been dealt with here. Hence, α can only be looked upon as an effective parameter. In order to calculate VP rates for nonlinear geometries, numerical techniques have to be invoked as analytical solutions do not exist for this type of problem. BJ solved the close coupling (CC) equations numerically employing the scattering formalism.[31,32] The quasibound states of the complex manifest themselves as scattering resonances, close to the zero order energies of the bound states of the v'-state-averaged van der Waals potential. The width of these resonances can be related to the rate of VP. Calculations of

the VP rates for T-shaped I_2He within this scheme resulted in lowering the rates with respect to analogous calculations in the collinear geometry. The van der Waals potential for the T-shaped complex was taken as a sum of two identical Morse potentials between each I atom and He, where $D_{XB}(\text{collinear}) = 2D_{XB}(\text{T-shape})$.[31,32]

The CC calculations for I_2Ne in a collinear configuration were obtained and gave a VP lifetime of about 2 ns for $v'_i = 2$. The parameters used were $\alpha_{XB} = 1.31$ Å^{-1} and $D_{XB} = 100$ cm^{-1}. It is difficult to compare this number with our results as the lowest vibrational state covered in our studies is $v'_i = 13$. DDW calculations using the same parameter set led to comparable results. From Figure 11(b) of Reference 30a, where some results of VP rate calculations for I_2Ne (collinear geometry) in the DDW framework (including continuum-continuum coupling) were plotted, we can extract some data for e.g., $v'_i = 20$. With $D_{XB} = 100$ cm^{-1} and $\omega_{XB} = 25$ cm^{-1}, the authors obtained a lifetime τ of about 3.5 ps for this vibrational quantum number; changing ω_{XB} to 20 cm^{-1} leads to about 5 ps, and with $D_{XB} = 95$ cm^{-1} and $\omega_{XB} = 35$ cm^{-1} they obtained ca. 500 fs. These calculations were performed by choosing l' to be the van der Waals stretch quantum number that maximizes the VP rate. All of the above calculations do not agree with the absolute magnitudes obtained experimentally (see Table I).

3.3.2d Effect of rotations, and other models

In order to take into account the effect of rotational excitation, calculations within the rotational infinite order sudden approximation (RIOSA) have been performed for I_2X complexes.[40,41] As the rotational energies are smaller than the vibrational stretching energies, the rotations are treated adiabatically. Vibrational-rotational coupling as well as centrifugal coupling can also be included. RIOSA calculations have been performed in the Fermi golden rule diabatic distorted wave framework, and in the CC framework where the CC-equations are solved exactly for each angle θ and the rotationally averaged resonance widths yield the desired VP rates.[41] Calculations on I_2He show that the effect of the

rotations on the excitation is negligible (pure V-T process) and on the VP rates leads to a further slowing down with respect to the T-shaped geometry.[30,41]

An interesting result emerges from these calculations. By going from the linear configuration to the T-shaped configuration and including rotations, the additional degree of freedom seems to stabilize the complex with respect to VP.[30b]

Delgado-Barrio and coworkers performed three-dimensional CC RIOSA type calculations in order to obtain VP rates for I_2Ne.[42] For $v'_i = 28$ ($l' = 0$, no van der Waals bending excitation), they calculated VP rates for different angles θ. Their angle-averaged VP rate leads to a lifetime of about 13 ps which is in line with our results ($v'_i = 23$: 53 ps) as the rate is expected to increase nonlinearly with v'_i. The parameters these authors used[43] were $D_{XB} = 66.48$ cm^{-1} and $\alpha_{XB} = 1.9$ Å^{-1}.

Further improvements of the above described procedures have been proposed. An adiabatic distorted wave (ADW) approach, by Halberstadt and Beswick,[44] and an adiabatic model including non-Condon effects by Kokubo and Fujimura,[45] have been formulated. There are other calculations on different van der Waals molecules (see e.g., Refs. 46-48).

The adiabatic calculation by Kokubo and Fujimura[45] of the VP rate of I_2Ne employed the parameters $D_{XB} = 94.7$ cm^{-1} and $\alpha_{XB} = 1.38$ Å^{-1}. They chose a collinear geometry for the complex. From Figure 4 of their paper we extract a lifetime of ca. 15 ps ($v'_i = 20$, $l' = 2$) in the Condon approximation, a value which should be compared with our result of 78 ps for the same level. Inclusion of non-Condon effects, however, led Kokubo and Fujimura to a lifetime of about 650 fs, which is far too small even if one considers that they did not perform calculations for $l' = 0$.

Schatz, Gerber, and Ratner introduced a SCF Hartree product as an initial state into the DDW calculations.[49] They performed calculations on the VP of I_2Ne in a collinear geometry. With the same parameters as BJ they obtained very good agreement with the DDW calculations including continuum-continuum interactions.[30]

3.3.2e Classical trajectory and RRKM calculations

Classical trajectory calculations have been performed by several groups[41,50-52] on I_2He, I_2Ar, and on I_2Ne above $v'_i = 35$ (in the crossover range were the v'_i-1 channel closes).[41,53] The results agree quite well with quantum calculations. Unfortunately, to our knowledge, there does not exist a classical trajectory study on I_2Ne in the range covered by our experiments, but these calculations are now under way in the groups of S.A. Rice[54a] and G. Delgado-Barrio.[54b]

Gray and Rice discussed an alternative RRKM (ARRKM) method, in addition to quantum mechanical and classical dynamical calculations,[52] and performed calculations on I_2Ar (*vide infra*). Very recently a time-dependent wavepacket approach[55] has been proposed which will prove particularly useful when we experimentally bridge the femtosecond wave packet dynamics to the picosecond dynamics of VP (this work).

3.4 The I_2Ar System

In two ways I_2Ar behaves differently from I_2Ne. First, as the depth of the van der Waals potential (D_0 = 220 - 226.3 cm^{-1}) is much larger than that of I_2Ne, the VP process favors the channel $v'_f = v'_i$-3 (see Ref. 22). Second, VP in I_2Ar is accompanied by a competing electronic predissociation (EP), as reported by Levy and coworkers[22] and by Atkinson and coworkers.[57] Thus, the measured rates are expected to be faster than those determined by pure VP which is one of the two channels describing the dynamics:

$$I_2Ar^*(v'_i) \xrightarrow{k_{vp}} I_2^*\ (v'_f = v'_i - 3) + Ar \qquad (27a)$$

$$\xrightarrow{k_e} I + I + Ar. \qquad (27b)$$

For the I_2Ar experiments reported here, the pump laser excites the complex into a vibrational level v'_i. The probe laser detects the nascent I_2^* in its B-state vibrational level $v'_f = v'_i - 3$ by exciting it to an I_2 ion pair state from which fluorescence was collected. The transients measured for $v'_i = 21$, $v'_f = 18$ and for $v'_i = 18$, $v'_f = 15$, together with the corresponding bare iodine transients $v' = 18$ and $v' = 15$, are shown in Figures 13(a) and 13(b), respectively. From least-squares fits to the exponential rise, we obtained a rise time of 77 ± 8 ps for $v'_i = 21$ and 70 ± 11 ps for $v'_i = 18$. An estimate of 30 ps for $v'_i = 15$ was obtained from linewidth measurements;[22] the spectral bands are inhomogeneously broadened due to unresolved rotational bands.

3.4.1 VP and EP Rates

Evidence for non-negligible EP in I_2Ar comes from measurements of the fluorescence intensity of I_2^*, formed after excitation of the complex, as a function of v'_i. Levy and coworkers found strong "oscillations" which were not exhibited by the complexes I_2He and I_2Ne.[22] Using intracavity absorption, fluorescence quantum yield studies by Atkinson and coworkers showed such oscillations.[57] These oscillations were attributed to variations in k_e with v'_i, presumably caused by the crossing of the B-state with the repulsive Π state(s).

From our experiments we obtain the absolute state-to-state rate for $v'_i = 21$ and for $v'_i = 18$, and we may use these rates and a simple kinetic scheme to obtain the ratio of the VP rate constants $k_{vp}(v'_i = 21)/k_{vp}(v'_i = 18)$. The model features the following channels:

$$\begin{array}{ccccc} 2I + Ar & \xleftarrow{k_e} & I_2^*Ar\ (B, v'_i) & \xrightarrow{k_{vp}} & I_2^*(B) + Ar \\ & & \downarrow k_f & & \downarrow k_{f'} \\ & & I_2Ar(X) + \text{photon} & & I_2(X) + Ar + \text{photon} \end{array} \qquad (28)$$

Assuming $k_f, k_{f'} << k_{vp}, k_e$, the number of I_2^* molecules can be expressed as:

$$[I_2^*](t) = \frac{N_0 k_{vp}}{(k_{vp} + k_e)}\left\{1 - \exp\left[-(k_{vp} + k_e)t\right]\right\}, \tag{29}$$

where N_0 denotes the number of initially (t = 0) excited $I_2Ar^*(v'_i)$ complexes. The final number of nascent I_2^* is formed before any appreciable radiative decay, and thus,

$$[I_2^*]_\infty = \frac{N_0 k_{vp}}{(k_{vp} + k_e)}, \tag{30}$$

which also corresponds to the number of photons emitted (μs time scale) if only the radiative decay of I_2^* is assumed. In order to obtain an expression for the normalized fluorescence,[22] we have to consider the excitation of bare iodine into the vibrational level v'_i. Exciting N'_0 I_2 molecules into v'_i leads to a collection of N'_0 fluorescence photons if the fluorescence quantum yield is one. The normalized fluorescence can then be expressed as follows:

$$F(v'_i) = \frac{k_{vp}(v'_i)}{\left[k_{vp}(v'_i) + k_e(v'_i)\right]}\left[\frac{N_0(v'_i)}{N'_0(v'_i)}\right]. \tag{31}$$

From the state-to-state real-time measurements, the rise time gives:

$$\tau(v'_i) = \left[k_{vp}(v'_i) + k_e(v'_i)\right]^{-1}, \tag{32}$$

which when combined with equation (31) yields the ratio of interest:

$$\frac{F(21)}{F(18)} = \frac{N_0(21)N_0'(18)}{N_0(18)N_0'(21)} \times \frac{\tau(21)}{\tau(18)} \times \frac{k_{vp}(21)}{k_{vp}(18)}. \tag{33}$$

Assuming that the relevant Franck-Condon factors of bare I_2 and I_2 within the complex do not differ significantly (*i.e.*, the presence of the Ar atom does not disturb the shape and equilibrium position of the potential curves for absorption), and, furthermore, assuming that the experimental conditions under which the complex spectra were measured and those under which the bare iodine experiments were performed are identical, equation (33) reduces to:

$$\frac{k_{vp}(21)}{k_{vp}(18)} = \frac{F(21)}{F(18)} \frac{\tau(18)}{\tau(21)}. \qquad (34)$$

This equation relates the state-to-state rates to the ratio of the VP rate constants. F(21)/F(18) = 3, as estimated from Figure 2 of Reference 22, and our real-time results, when used in equation (34), give a ratio $k_{vp}(21)/k_{vp}(18)$ of about 2.9. Accordingly, k_{vp} increases with increasing the quantum number v'_i whereas k_e increases with decreasing v'_i. This latter behavior may be the reason why I_2Ar complexes have not been observed for low v'_i, and is consistent with the quantum yield results obtained by Atkinson and coworkers.[57]

3.4.2 Calculations of the VP Rates and Their v'_i-Dependence

Exploring the effect of the anharmonicity of the intramolecular bond on the behavior of the VP rate as a function of v'_i, BJ presented some calculations for I_2Ar (collinear geometry) in Table I of Reference 33. From these data we obtain the ratio $k_{vp}(20)/k_{vp}(15) = 5.6$. Assuming a v^6 dependence in this region ($20^6/15^6 = 5.6$), we arrive at $k_{vp}(21)/k_{vp}(18) = 2.5$, which is in good agreement with the finding of 2.9 reported here. Furthermore, in Reference 30b, BJ quoted a private communication with D.H. Levy who

deduced a v^5 dependence of k_{vp} (unpublished). Such a dependence leads to a ratio $k_{vp}(21)/k_{vp}(18) = 2.2$ which is still in fair agreement with our result.

As in the case of I_2Ne, the VP rate of I_2Ar increases with increasing v'_i, in accord with theory. However, the absolute magnitudes calculated for the VP rates are not in very good agreement with our results and vary significantly with the assumed parameters of the van der Waals potential. These calculations do not account for EP.

Using the values $D_{XB} = 200$ cm^{-1} and $\alpha_{XB} = 1.25$ Å^{-1}, BJ predicted a VP lifetime of about 25 ps for $v'_i = 20$ (collinear geometry).[30] Changing α to 2.02 Å^{-1} led to $\tau(20)<10$ ps,[31] which is far too small; for $v'_i = 21$ the calculated VP time is thus expected to be orders of magnitude shorter than 10 ps. DDW, ADW, and CC calculations yielded comparable results.[44] Calculations of VP of I_2Ar in a nonlinear geometry have, to our knowledge, not yet been performed. According to the results obtained for I_2He (*vide supra*), calculations for a T-shaped geometry, and especially three-dimensional calculations, are expected to lead to a decrease of the VP rates. This trend would then shift the results into the right direction for bridging the gap between theory and experiments.

Gray and Rice[52] performed classical dynamics (CD), Fermi golden rule (FGR), and ARRKM calculations in order to obtain the VP rates of I_2Ar in its *B*-state. They used the same parameters as BJ in Reference 30a and for $v'_i = 2$ they obtained VP times of about 6 ps (CD), 8 ps (FGR) and 4.5 ps (ARRKM). These numbers are consistent despite the differences between the various models, but still appear far too small in comparison with our experimental data. Correcting for the effect of van der Waals stretch excitation (quantum number l') can help the results by only about an order of magnitude, which is not sufficient for quantitative agreement (note that our experiments were performed for $v'_i = 18,21$).

From Figure 4 of the publication by Kokubo and Fujimura,[45] who applied their adiabatic scheme to the VP of I_2Ar (collinear geometry), we extract VP times of about 26

ps ($v'_i = 21$, $l' = 13$), and 11 ps ($v'_i = 21$, $l' = 8$) in the Condon approximation, and of about 4 ps ($v'_i = 21$, $l' = 13$), and 1.3 ps ($v'_i = 21$, $l' = 8$) when non-Condon effects are accounted for. From the same figure, we deduce VP times of about 53 ps ($v'_i = 18$, $l' = 13$) and 21 ps ($v'_i = 18$, $l' = 8$) in the Condon approximation, and of about 9.5 ps ($v'_i = 18$, $l' = 13$) and 2.7 ps ($v'_i = 18$, $l' = 8$) after including non-Condon effects (it would be very interesting to obtain results for $l' = 0$ in this scheme). Clearly, the inclusion of non-Condon effects seems to shorten the lifetimes tremendously, and this appears to be a trend in the wrong direction as noted in the case of I_2Ne discussed above.

3.5 Conclusions

In this chapter, we have presented the results of real-time studies of vibrational predissociation (VP) in I_2X clusters, where X = Ne, or Ar. State-to-state rates were measured, and the results were compared with a number of theoretical findings. The experimentally determined rates in real-time differ from those obtained by linewidth measurements due to the inhomogeneous and other broadening channels as discussed above. The state-to-state rates of VP show a non-linear dependence (increase) on v'_i, or an inverse dependence (decrease) on the energy available for VP over the range of v'_i studied. This non-linear behavior is in qualitative agreement with a number of theoretical models proposed for VP in these systems, and detailed here for comparisons with our experimental results. The theoretical models, however, do not yet provide accurate and unique absolute values of the state-to-state rates, although they appear to be in agreement with each other. For quantitative comparisons with experiments, theory must address the 3-D dynamical aspect (bending, *etc.*) of the problem and the nature of the potential. There are, however, some simple descriptions that emerge.

The overall change of the rates with v'_i can be understood using a simple semiclassical model of full-collision theory. In this model the translational energy is transferred to a vibrational energy, and the reverse case can be considered for the "half-

collision" VP process. In the half-collision, the repulsion occurs in a few hundreds of femtoseconds, and non-adiabatic energy transfer is expected since the vibrational period is ~ 300 fs. The energy flow of the I_2 vibrational excitation to the I_2-Ne coordinate is the bottleneck since, in a kinematic description, the time for bond breakage (at the translational energy of interest) is ~ 1 ps and the inverse rates are typically 50 - 200 ps.

The time scale for rotations is different from both the impulsive dissociation time and the inverse rate times. For example, in $v'_f = 20$ the rotational period is 660 ps for $J =$ 1 and 66 ps for $J = 10$. Thus, if VP is fast compared with rotations, the rotational alignment of nascent I_2* in the dissociation of I_2Ne* will be preserved and rotational recurrences become observable. Analysis of these recurrences gives both the rotational constant of the nascent fragment (*i.e.*, identification of v'_f) and the nascent rotational temperature.[58] As discussed in the text, the observations are also relevant to the theoretical treatment of the effect of rotations on VP. Elsewhere, we have reported details of the theory[59] and applications[60] to dissociation reactions.

For I_2Ar, the above simple picture of VP may still apply, but the problem of breaking the I-I bond in the presence of Ar (electronic predissociation) is far from being completely understood. The rate measurements indicate that both VP and EP are comparable in magnitude and that VP increases with v'_i while EP decreases with increasing v'_i. The simplest explanation is that the Ar couples the B-state surface to a repulsive surface (e.g., $^1\Pi_{1u}$). The problem becomes Landau-Zener type dynamics with the avoided crossing determining the overall rate of forming I+I, as in the case of NaI.[61] This nonadiabatic coupling between the B-state and the repulsive state may be enhanced by Ar due to spin-orbital coupling and the break-down of the Born-Oppenheimer approximation (in I_2 alone there is a weak electronic predissociation caused by hyperfine interactions).[62]

This type of nonadiabatic coupling scheme between the repulsive state (excited above the I+I* dissociation limit) and the B-state (the reverse of the above discussed case)

has been proposed[63] for another interesting problem. When I_2Ar is excited above the I+I* dissociation limit, it produces fluorescence from the bound levels of the *B*-state.[64] The Ar-induced coupling[65] mixes the repulsive potential and the *B*-state potential and thus some fluorescence is expected. It is also possible that the entire dynamics do not involve the repulsive surface, and that the I_2 is "caged"[64] by an Ar atom. As a result of a possible charge-transfer type interaction, it may be that Ar-electrons promote an antibonding I_2 excitation similar to known bimolecular reactions involving I_2. To address these and other questions, further experiments are planned in this laboratory in order to follow the dynamics from the fs (preparation) to the ps (dissociation) time domain. There are other interesting systems, studied by the Janda group[66] and the Lester group[10,67] that these real-time experiments should be extended to, hopefully to relate the nature of (different) bonding to the dynamics.

Acknowledgements

This work was supported by a grant from the National Science Foundation (DMR). Our research group has enjoyed discussions with Profs. E. E. Nikitin and J. A. Beswick during their visits to Caltech, and with Prof. G. Delgado-Barrio on some theoretical problems discussed in this chapter.

3.6 References

1. A. D. Buckingham, P. W. Fowler, and J. M. Hutson, Chem. Rev. **88**, 963 (1988).

2. K. I. Peterson, G. T. Fraser, D. D. Nelson, and W. Klemperer, in *Comparison of Ab Initio Quantum Chemistry with Experiments for Small Molecules: The State of the Art*, R. J. Bartlett ed., Reidel, Dordrecht (1985), pp. 217.

3. L. Khundkar and A. H. Zewail, Annu. Rev. Phys. Chem. **41**, 15 (1990) and references therein.

4 (a). J. J. F. Ramaekers, H. K. van Dijk, J. Langelaar, and R. P. H. Rettschnick, Faraday Discuss. Chem. Soc. **75**, 183 (1983); (b).M. Heppener, A. G. M. Kunst, D. Bebelaar, and R. P. H. Rettschnick, J. Chem. Phys. **83**, 5341 (1985).

5. P. M. Weber and S. A. Rice, J. Chem. Phys. **88**, 6120 (1988).

6. S. A. Wittmeyer, A. J. Kaziska, A. L. Hotyka, and M. R. Topp, Chem. Phys. Lett. **154**, 1 (1989).

7. D. M. Semmes, J. S. Baskin, and A. H. Zewail, J. Chem. Phys. **92**, 3359 (1990).

8. M. R. Nimlos, M. A. Young, E. R. Bernstein, and D. F. Kelley, J. Chem. Phys. **91**, 5268 (1989).

9. (a) M. P. Cassassa, J. C. Stephenson, and D. S. King, J. Chem. Phys. **89**, 1966 (1988); (b). M. P. Cassassa, Chem. Rev. 88, 815 (1988).

10. (a). J. C. Drobits, J. M. Skene, and M. I. Lester, J. Chem. Phys. **84**, 2896 (1986); (b). J. C. Drobits and M. I. Lester, J. Chem. Phys. **86**, 1662 (1987)(c). J. C. Drobits and M. I. Lester, J. Chem. Phys. **88**, 120 (1987).

11. (a). R. E. Miller, J. Phys. Chem. **90**, 3301 (1986); (b). R. E. Miller, Science **240**, 447 (1988).

12. (a). K. C. Janda, Adv. Chem. Phys. **60**, 2011 (1985); (b). F. G. Celli and K. C. Janda, Chem. Rev. **86**, 507 (1986); (c). K. C. Janda and C. Bieler, in *Atomic and Molecular Clusters*, E. R. Bernstein ed., Elsevier, Amsterdam (1990), pp. 455.

13. W. R. Gentry, in *Structure and Dynamics of Weakly Bound Molecular Complexes*, NATO ASI series, A. Weber ed., D. Reidel, Dordrecht (1987), pp. 467.

14. (a). R. M. Bowman, M. Dantus, and A. H. Zewail, Chem. Phys. Lett. **161**, 297 (1989); (b). M. Dantus, R. M. Bowman, and A. H. Zewail, Nature **343**, 737

(1990); (c). M. Gruebele, G. Roberts, M. Dantus, R. M. Bowman, and A. H. Zewail, Chem. Phys. Lett. **166**, 459 (1990).

15. J. J. Breen, D. M. Willberg, and M. Gutmann, A. H. Zewail, J. Chem. Phys. **93**, 9180 (1990).

16. Chapter V. of this thesis.

17. D. H. Levy, Adv. Chem. Phys. **47**, part 1, 323 (1981).

18. W. Sharfin, K. E. Johnson, L. Wharton, and D. H. Levy, J. Chem. Phys. **71**, 1292 (1979).

19. J. E. Kenny, K. E. Johnson, W. Sharfin, and D. H. Levy, J. Chem. Phys. **72**, 1109 (1980).

20. K. E. Johnson, W. Sharfin, and D. H. Levy, J. Chem. Phys. **74**, 163 (1981).

21. J. A. Blazy, B. M. DeKoven, T. D. Russell, and D. H. Levy, J. Chem. Phys. **72**, 2439 (1980).

22. G. Kubiak, P. S. H. Fitch, L. Wharton, and D. H. Levy, J. Chem. Phys. **68**, 4477 (1978).

23. R. E. Smalley, L. Wharton, and D. H. Levy, J. Chem. Phys. **68**, 671 (1978).

24. A. H. Zewail, Acc. Chem Res. **13**, 360 (1980).

25. For a review on the separations of time (T_1 and T_2) for homogeneously-broadened transitions see: M. J. Burns, W. K. Liu, and A. H. Zewail in *Spectroscopy and Excitation Dynamics of Condensed Molecular Systems*, Vol. IV, V. M. Agranovich and R. M. Hochstrasser eds., pp. 301, North Holland, New York (1983).

26 R. S. Mulliken, J. Chem. Phys. **55**, 288 (1971).

27 S. Gerstenkorn and P. Luc, J. Physique **46**, 867 (1985).

28. J. C. D. Brand and A. R. Hoy, Appl. Spectr. Rev, **23**, 285 (1987).

29. P. R. Bevington, *Data Reduction and Error Analysis for the Physical Sciences*, McGraw-Hill, New York (1969) pp. 204.

30. (a). J. A. Beswick and J. Jortner, J. Chem. Phys. **68**, 2277, (1978); (b). J. A. Beswick and J. Jortner, Adv. Chem. Phys. **47**, part I, 363 (1981).

31. J. A. Beswick, J. Jortner, J. Chem. Phys. **69**, 512 (1978).

32. J. A. Beswick, G. Delgado-Barrio, and J. Jortner, J. Chem. Phys. **70**, 3895 (1979).

33. J. A. Beswick and J. Jortner, Molecular Physics, **39**, 1137 (1980).

34. G. E. Ewing, J. Chem. Phys. **71,** 3143 (1979).

35. G. E. Ewing, J. Chem. Phys. **72**, 2096 (1980).

36. G. E. Ewing, Farad. Discuss. Chem. Soc. **73**, 325, 402 (1982).

37. G. E. Ewing, J. Phys. Chem. **90**, 1990 (1986).

38. D. M. Willberg, M. Gutmann, E. E. Nikitin, and A. H. Zewail, Chem. Phys. Lett. **201**, 506 (1993).

39. R. J. Le Roy, M. R. Davies, and M. E. Lam, J. Phys. Chem. **95**, 2167, (1991).

40. G. Delgado-Barrio, P. Villarreal, A. Varade, N. Martin, and A. Garcia, in *Structure and Dynamics of Weakly Bound Molecular Complexes*, NATO ASI series, A. Weber ed., D. Reidel, Dordrecht (1987), pp. 573.

41. G. Delgado-Barrio, *Predissociation in van der Waals Molecules*, Lecture Notes for the "Fourth Europhysics Summer School on Chemical Physics: Molecular Dynamics with Lasers," Murcia, Spain (1989).

42. A. M. Cortina, S. Miret-Artes, P. Villarreal, and G. Delgado-Barrio, J. Mol. Struct. **142**, 513 (1986).

43. E. de Pablo, S. Miret-Artes, P. Moreca, P. Villarreal, and G. Delgado-Barrio, J. Mol. Struct. **142**, 505 (1986).

44. N. Halberstadt and J. A. Beswick, Farad. Discuss. Chem. Soc. **73**, 357 (1982).

45. T. Kokubo and Y. Fujimura, J. Chem. Phys. **85**, 7106 (1986).

46. B. P. Reid, K. C. Janda, and N. Halberstadt, J. Phys. Chem. **92**, 587 (1988).

47. O. Roncero, J. A. Beswick, N. Halberstadt, P. Villarreal, and G. Delgado-Barrio, J. Chem. Phys. **92**, 3348 (1990).

48. R. L. Waterland, M. I. Lester, and N. Halberstadt, J. Chem. Phys. **92**, 4261 (1990).

49. G. C. Schatz, R. B. Gerber, and M. A. Ratner, J. Chem. Phys. **88**, 3709 (1988).

50. J. A. Beswick, G. Delgado-Barrio, P. Villarreal, and P. Moreca, Farad. Discuss. Chem. Soc. **73**, 406 (1982).

51. G. Delgado-Barrio, P. Villerreal, P. Moreca, and G. Albelda, J. Chem. Phys. **78**, 280 (1983).

52. S. K. Gray and S. A. Rice, Farad. Disc. Chem. Soc., **82**, 307 (1986).

53. G. Delgado-Barrio, P. Villarreal, P. Mareca, and J. A. Beswick, J. Comput. Chem. **5**, 322 (1984).

54. (a). S. A. Rice, private communication; (b). G. Delgado-Barrio, private communication.

55. P. Villarreal, S. Miret Artes, O. Roncero, G. Delgado-Barrio, J. A. Beswick, N. Halberstadt, and R. D. Coalson, J. Chem. Phys. **94**, 4230 (1991).

56. (a). D. E. Brinza, C. M. Western, D. D. Evard, F. Thommen, B. A. Swartz, and K. C. Janda, J. Phys. Chem. **88**, 2004 (1984); (b). L. J. van de Burgt, J.-P. Nicolai, and M. C. Heaven, J. Chem. Phys. **81**, 5514 (1984); (c). M. T. Berry, M. R. Brustein, and M. I. Lester, J. Chem. Phys. **92**, 6469 (1990).

57. N. Goldstein, T. L. Brack, and G. H. Atkinson, J. Chem. Phys. **85**, 2684 (1986).

58. D. M. Willberg, J. J. Breen, M. Gutmann, and A. H. Zewail, J. Phys. Chem. **95**, 7136 (1991).

59. A. H. Zewail, J. Chem. Soc., Faraday Trans. 2, **85**, 1221 (1989).

60. (a). M. Dantus, R. M. Bowman, J. S. Baskin, and A. H. Zewail, Chem. Phys. Lett. **159**, 406 (1989); (b). J. S. Baskin, D. Semmes, and A. H. Zewail, J. Chem. Phys. **85**, 7488 (1986).

61. (a). T. S. Rose, M. J. Rosker, and A. H. Zewail, J. Chem. Phys. **88**, 6672 (1988); (b). M. J. Rosker, T. S. Rose, and A. H. Zewail, Chem. Phys. Lett. **146**, 175 (1988); (c). T. S. Rose, M. J. Rosker, and A. H. Zewail, J. Chem. Phys. **91**, 7415 (1989).

62. (a). M. Broyer, J. Vigue, and J. C. Lehmann, J. Chem Phys. **64**, 4793 (1976); (b). H. Levebvre-Brion and R. W. Field, "Perturbations in the Spectra of Diatomic Molecules," Academic Press, Orlando (1986).

63. J. A. Beswick, R. Monot, J.-M. Philippoz, and H. van den Bergh, J. Chem. Phys. **86**, 3965 (1987).

64. (a). J. J. Valentini, and J. B. Cross, J. Chem. Phys. 77, 572 (1982); (b). J. M. Philippoz, R. Monot, and H. van den Bergh, J. Chem. Phys. **93**, 8676 (1990), and references therein.

65. The energy was found to drop by ~ 1000 cm^{-1} to the bound fluorescing levels. We have calculated that in order for this process to compete with dissociation efficiently, the matrix element for the coupling has to be on the order of 400 cm^{-1}.

66. C. R. Bieler, K. E. Spence, and K. C. Janda, J. Phys. Chem. **95**, 5058 (1991), and references therein.

67. M. T. Berry, M. R. Brustein, and M. I. Lester, J. Chem. Phys. **92**, 6469 (1990).

Table 1. The state-to-state rates and lifetimes of I_2Ne vibrational predissociation as a function of v'_i.

v'_i	τ(ps)	$k(v'_i,v'_f) \times 10^9$ s^{-1}
13	216 ± 16	4.6 ± 0.4
14	196 ± 12	5.1 ± 0.3
15	182 ± 20	5.5 ± 0.6
16	160 ± 15	6.3 ± 0.6
17	126 ± 12	7.9 ± 0.8
18	107 ± 9	9.3 ± 0.9
19	87 ± 4	11.5 ± 0.9
20	78 ± 4	12.8 ± 1.0
21	69 ± 6	14.5 ± 0.7
22	58 ± 3	17.2 ± 0.9
23	53 ±3	18.9 ± 1.0

The values reported are typically the average of at least five or six independent measurements. The errors reported are one standard deviation.

Table 2. Some key parameters and definitions (for Morse potentials) used in the theoretical analysis.

D_{XB}	Potential well depth
$\omega_{XB} = \left(\frac{1}{\mu_{X,BC}} \left(\frac{\partial^2 U}{\partial Q^2} \right)_{Q_0} \right)^{1/2}$	Characteristic Morse frequency
$\mu_{X,BC} = \frac{m_X (m_B + m_C)}{m_X + m_B + m_C}$	Reduced mass of the complex
$\alpha_{XB} = \omega_{XB} \left(\frac{\mu_{X,BC}}{2D_{XB}} \right)^{1/2}$	Characteristic inverse length[a]
$\varepsilon_{l'} = -D_{XB} + \hbar\omega_{XB} \left(l' + \frac{1}{2} \right) \left(1 - \frac{\left(l' + \frac{1}{2} \right)}{2K_{XB}} \right)$	Energy of the bound state $\lvert l' \rangle$
$\theta_{\varepsilon'} = \frac{\left(2\mu_{X,BC} \varepsilon' \right)^{1/2}}{\hbar\alpha_{XB}}$	Energy parameter
$K_{XB} = \frac{2D_{XB}}{\hbar\omega_{XB}}$	Anharmonicity
$N = \left(K_{XB} + \frac{1}{2} \right)$	Number of bound states in the Morse potential[b]
$\mu_{BC} = \frac{m_B m_C}{m_B + m_C}$	Reduced mass of B-C

[a] The relationship between a_{XB} and w_{XB} is obtained b explicitly considering $\partial^2 U / \partial Q^2$ from Equation (10).

[b] The value obtained for N in this expression is rounded off to an integer value.

3.7 Figure Captions

1. A schematic of the vibrational predissociation process in a two coordinate space. Shown on the right is the van der Waals stretch coordinate (R) and on the left is the I_2 stretch coordinate (r). The I_2 energy levels correspond to an infinite I_2 – Ne separation. Vibrational predissociation, a bound to a continuum transition, occurs as one quantum of energy is lost from the I_2 stretch to the van der Waals coordinate.
2. Diagram showing the experimental scheme used in measuring the state-to-state rates. The pump laser prepares the metastable cluster in a selected vibronic state which then undergoes vibrational predissociation. The probe laser then excites the nascent I_2^* to an ion-pair state from which the UV fluorescence is detected.
3. Representative transients obtained for three different values of v'_i: v'_i = 13, 18, and 23. The dashed line is the fit to an exponential rise function, from which the value of the state-to-state rate is given.
4. The VP lifetimes obtained from the real-time studies reported in this chapter (solid squares), and the lifetimes estimated from linewidth measurements presented in Reference 22.
5. Shown is a typical transient obtained for the $v'_i = 23/v'_f = 22$ experiments: (top) is a bare I_2 ($v' = 22$)transient obtained for calibration; (middle) is a transient showing the predissociation (τ = 53 ps); and (bottom) the visible cross-correlation of the pump and probe lasers. The dashed lined shows a fit to an exponential rise function.
6. The rate of vibrational predissociation as a function of the vibrational level v'_i excited.
7. The rate of vibrational predissociation as a function of the available energy. The available energy is defined as the difference in energy between the v'_i and v'_i-1 vibrational levels of the B-electronic state of I_2.
8. Theoretical fits of the experimentally determined rates to the models described in the text. The abscissa corresponds to the square root of the kinetic energy of

fragmentation with $l' = 0$. The squares given with the error bars represent the data and the dashed lines correspond to a nonlinear least squares fit of these data to functional forms given by: a) Equation (19), b) Equation (20), and c) Equation (22). See text for discussions.

9. Theoretical fits of the experimentally determined rates to test their v'_i dependance. The squares given with the error bars represent the data and the dashed lines correspond to a nonlinear least squares fit of these data to functional forms given by: a) Equation (25), b) Equation (26), and c) a third order polynomial. See text for discussions.

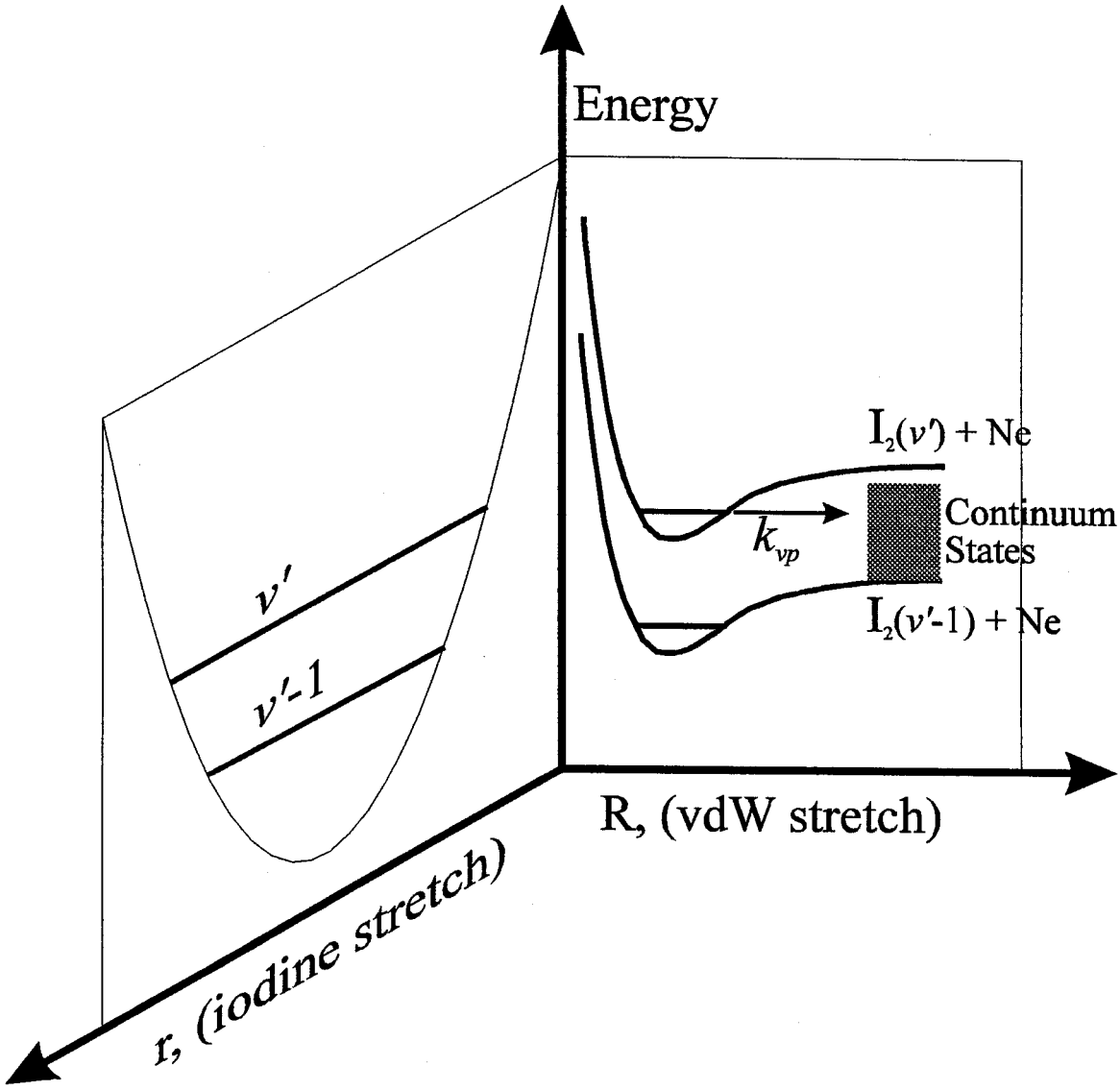
Energy
$I_2(v')$ + Ne
Continuum States
k_{vp}
$I_2(v'-1)$ + Ne
v'
$v'-1$
R, (vdW stretch)
r, (iodine stretch)

Figure 1

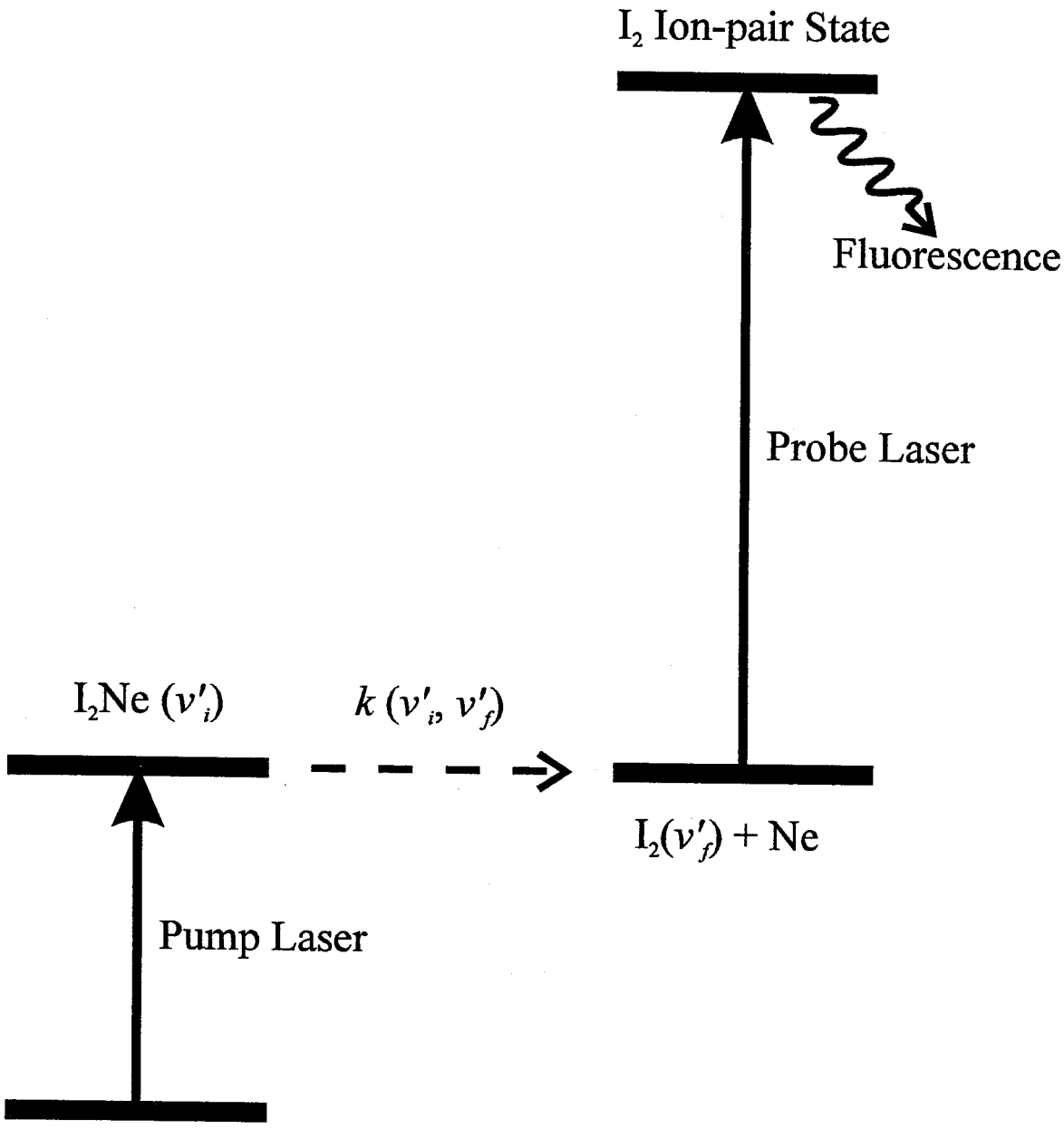
I2 Ion-pair State
Fluorescence
Probe Laser
I2Ne (v'i)
k (v'i, v'f)
I2(v'f) + Ne
Pump Laser

Figure 2

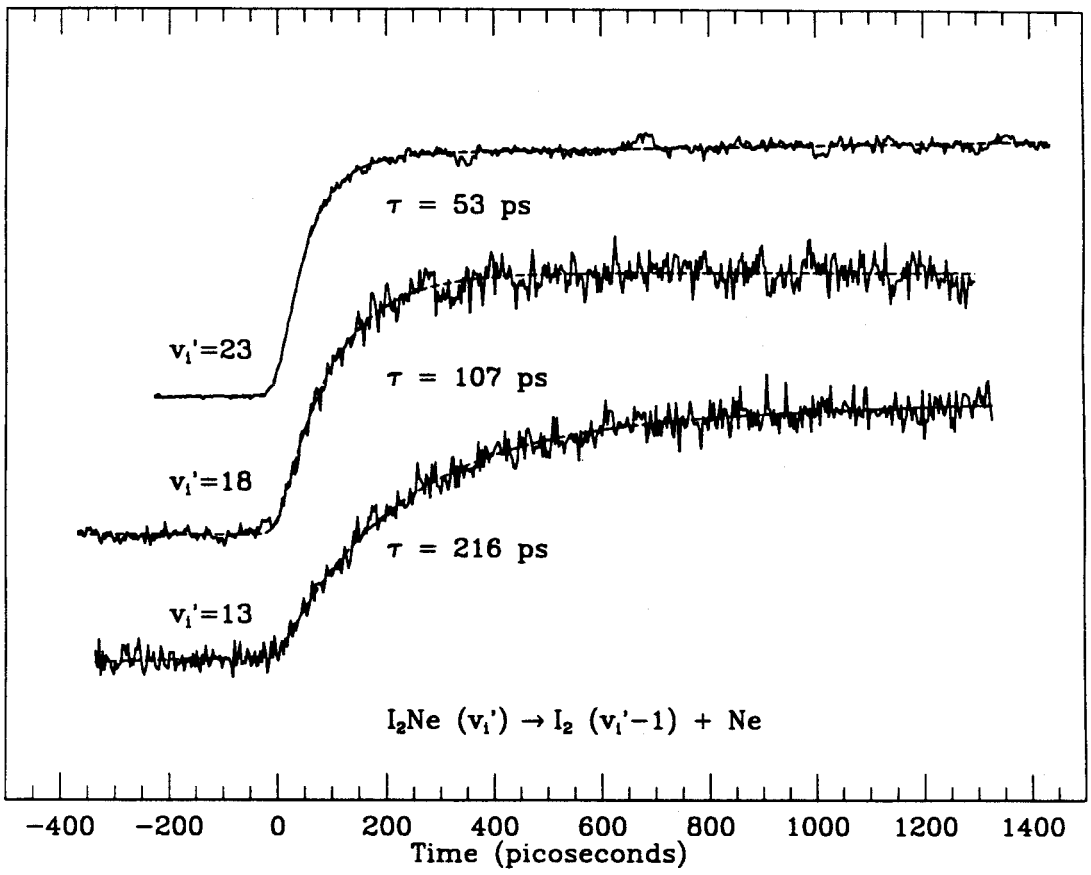
τ = 53 ps
v₁'=23
τ = 107 ps
v₁'=18
τ = 216 ps
v₁'=13
I₂Ne (v₁') → I₂ (v₁'−1) + Ne
−400
−200
0
200
400
600
800
1000
1200
1400
Time (picoseconds)

Figure 3

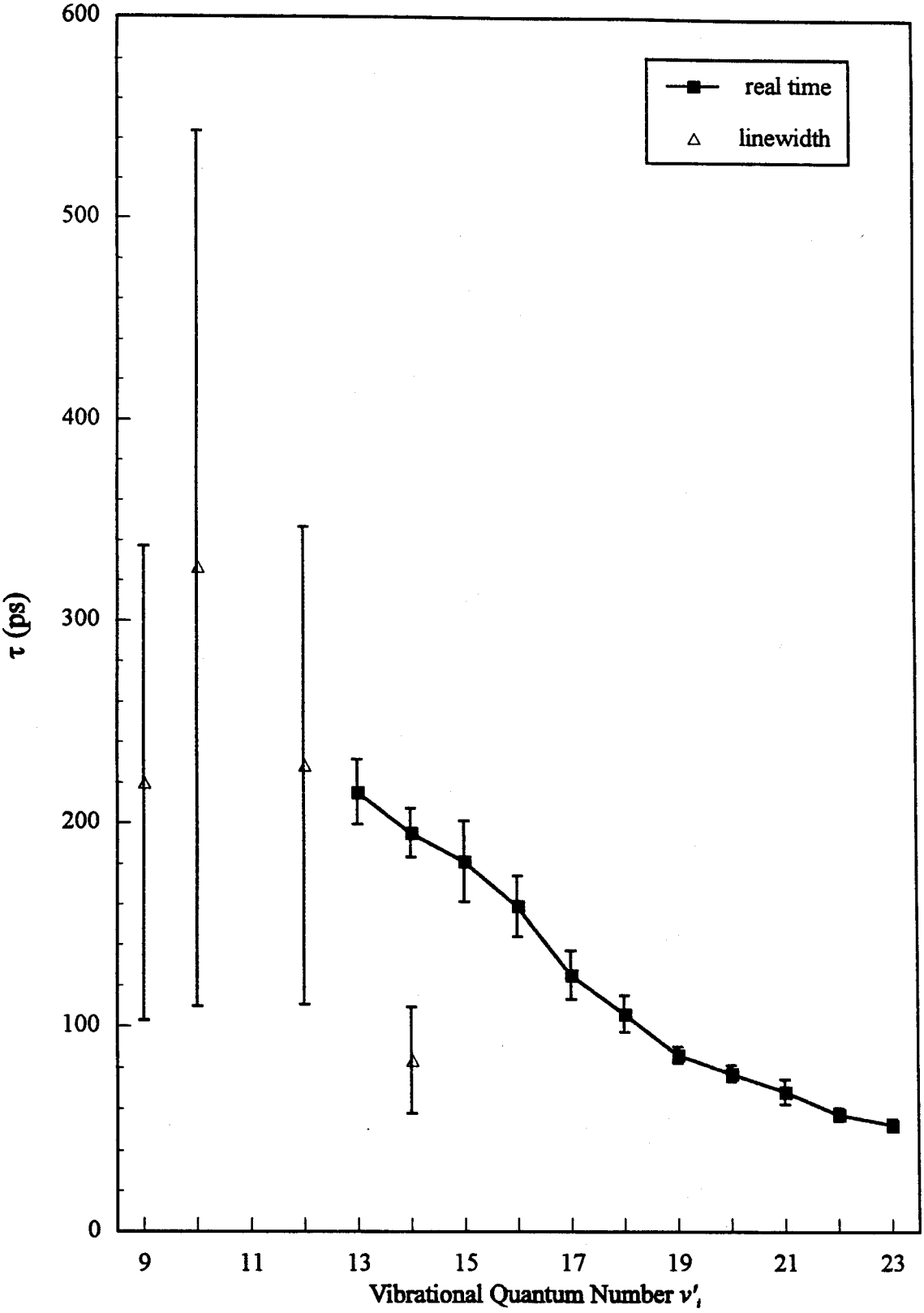
real time
linewidth
τ (ps)
600
500
400
300
200
100
0
9
11
13
15
17
19
21
23
Vibrational Quantum Number v'_i

Figure 4

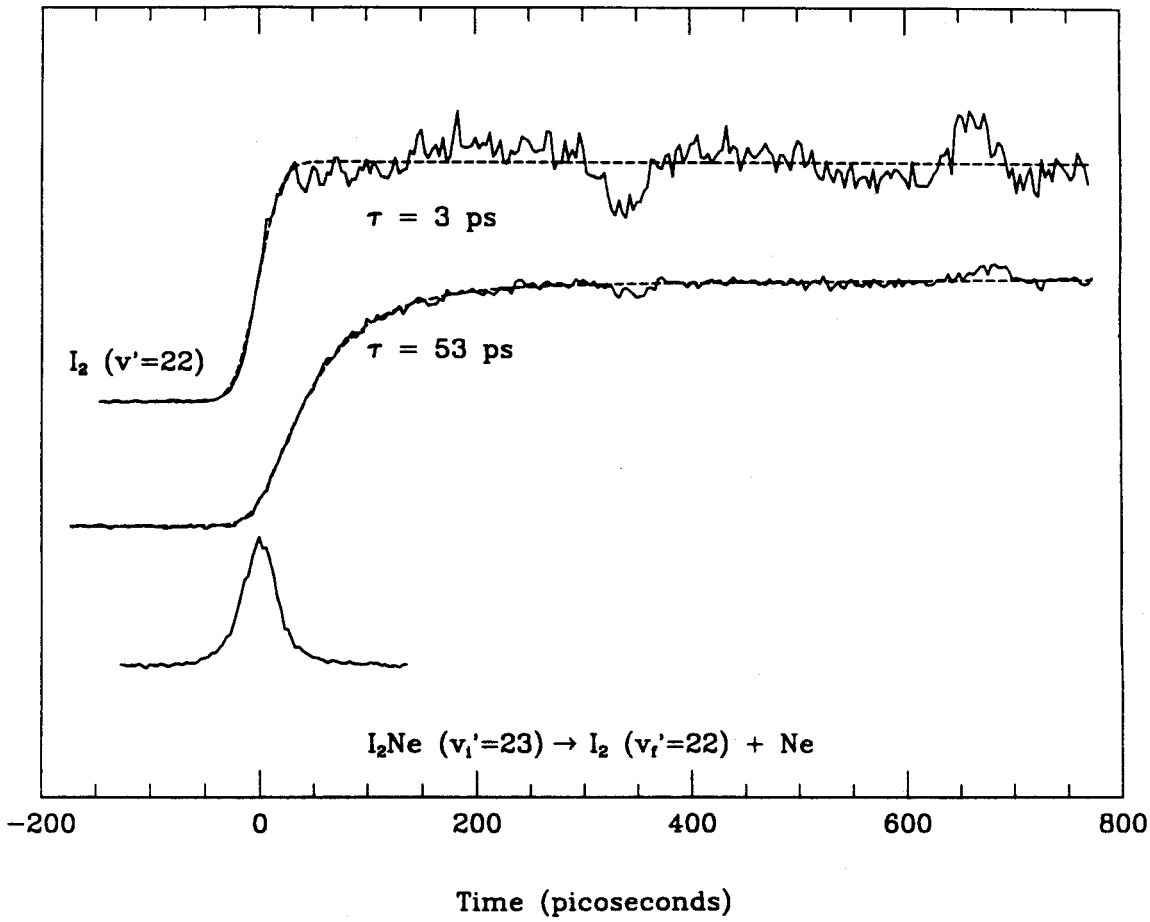
τ = 3 ps
I₂ (v'=22)
τ = 53 ps
I₂Ne (v_i'=23) → I₂ (v_f'=22) + Ne
−200
0
200
400
600
800
Time (picoseconds)

Figure 5

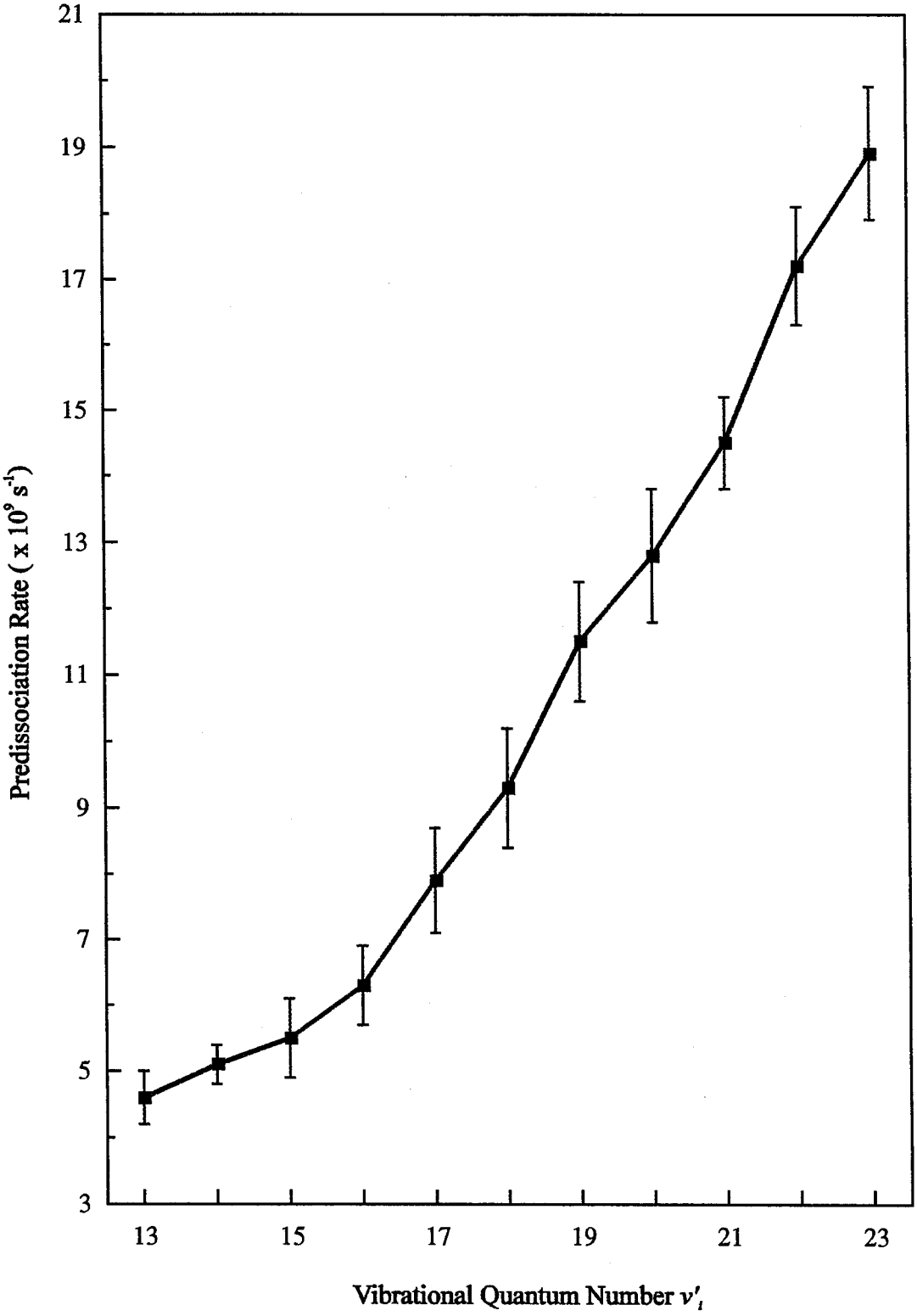
21
19
17
15
13
11
9
7
5
3
Predissociation Rate (x 10⁹ s⁻¹)
13
15
17
19
21
23
Vibrational Quantum Number v'ₗ

Figure 6

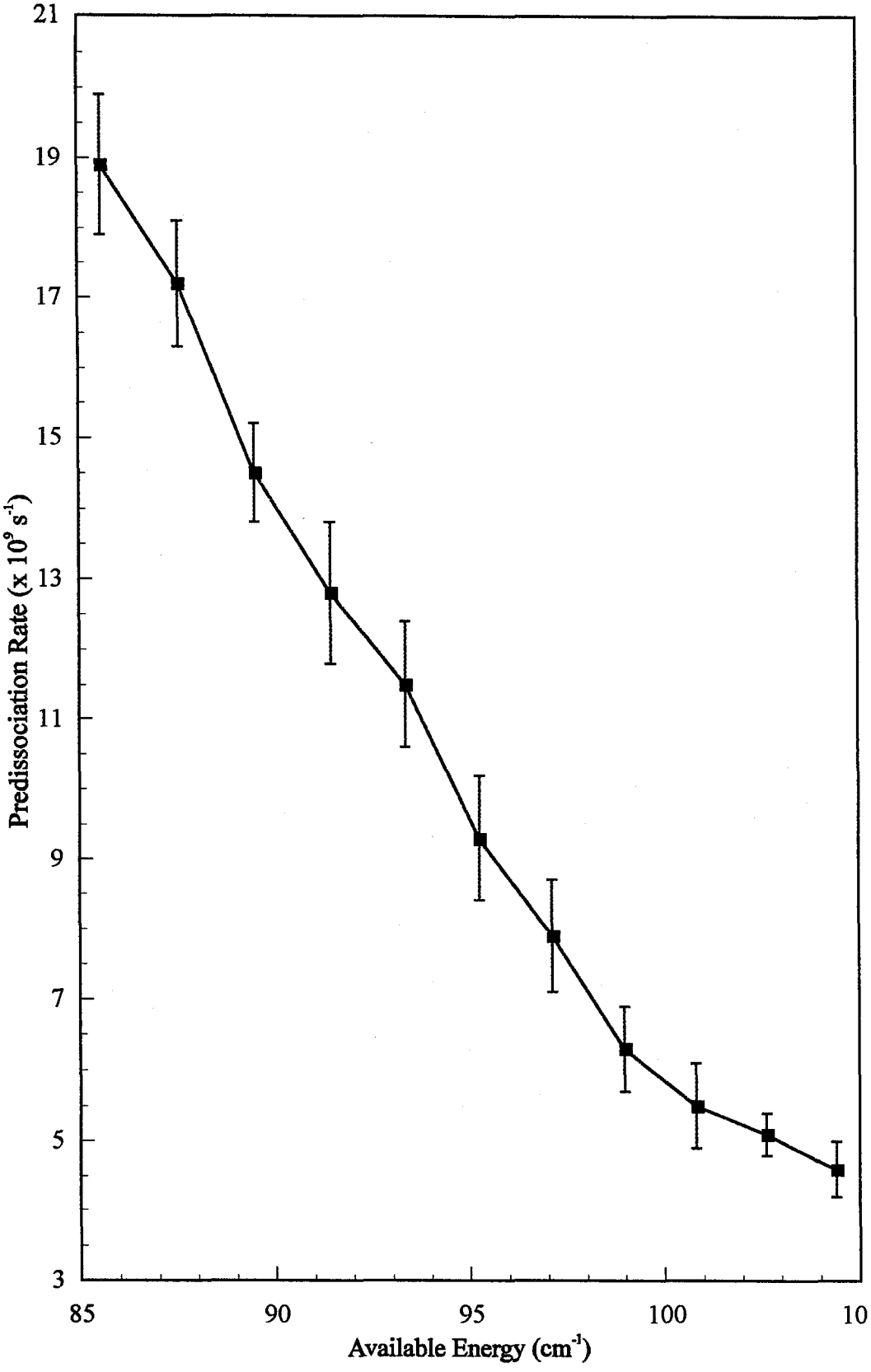
21
19
17
15
13
11
9
7
5
3
Predissociation Rate (x 10^9 s^-1)
85
90
95
100
10
Available Energy (cm^-1)

Figure 7

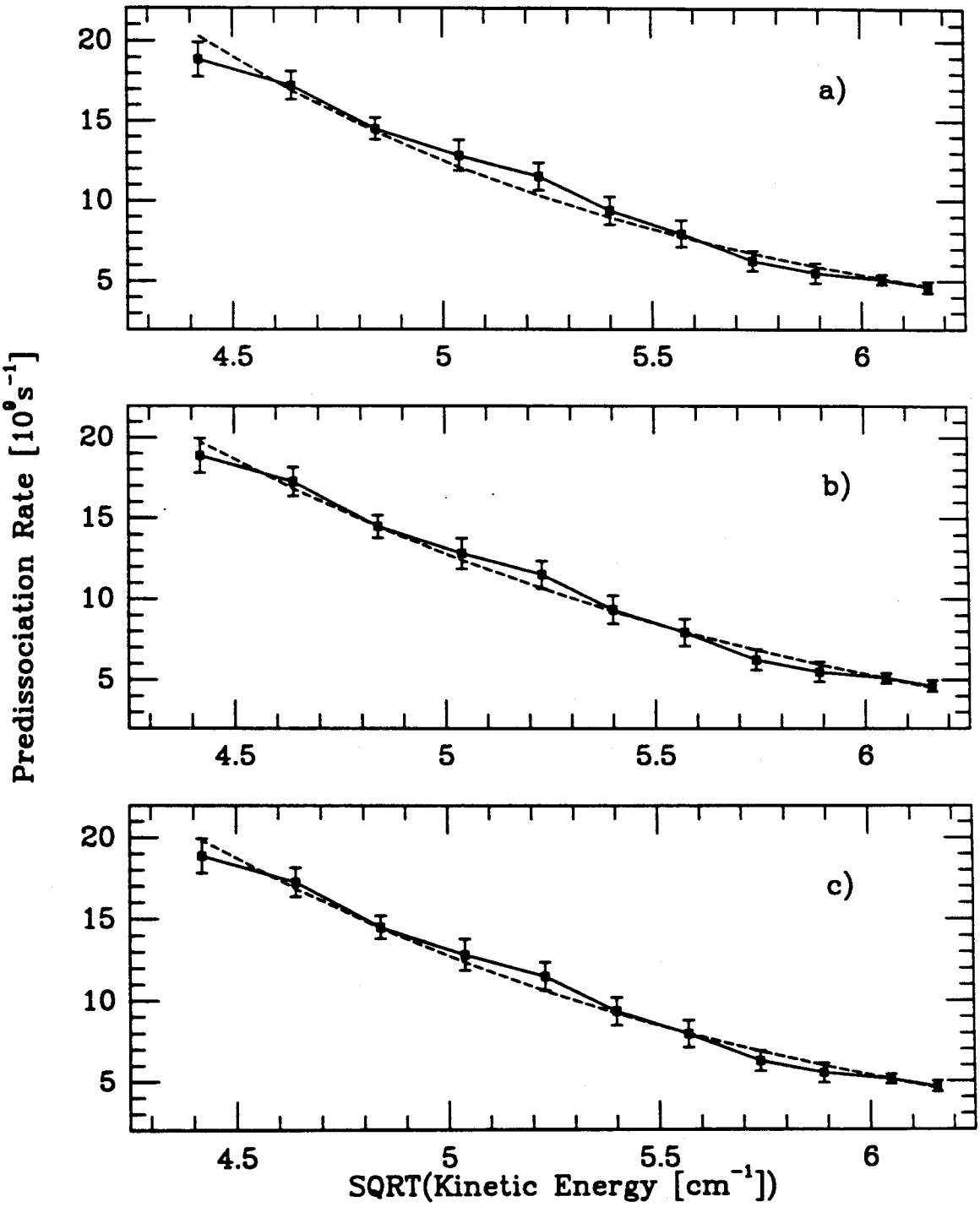
a)
b)
c)
20
15
10
5
4.5
5
5.5
6
Predissociation Rate [$10^9 s^{-1}$]
SQRT(Kinetic Energy [cm^{-1}])

Figure 8

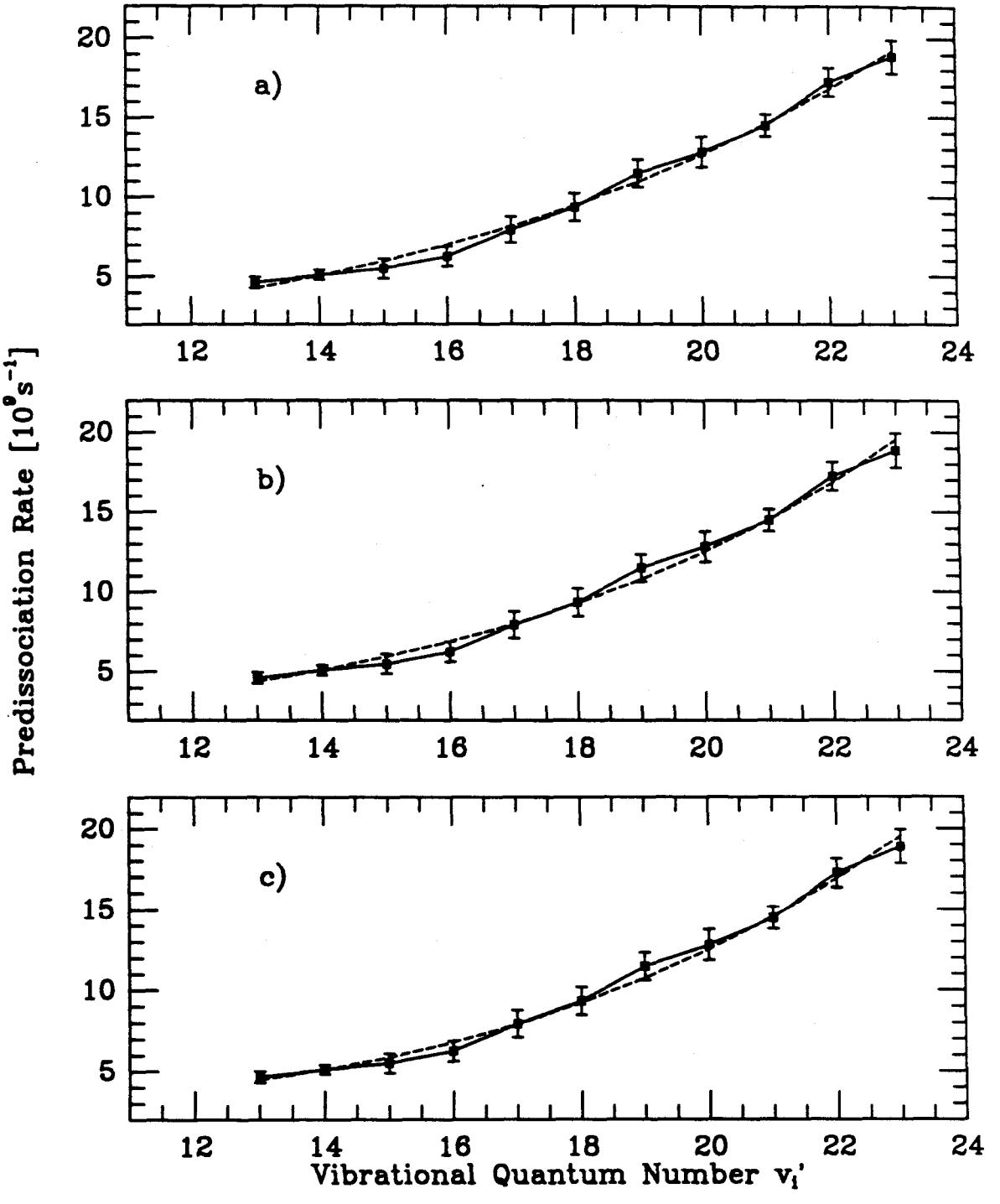
a)
b)
c)
Predissociation Rate [$10^9 s^{-1}$]
Vibrational Quantum Number v_i'
5
10
15
20
12
14
16
18
20
22
24

Figure 9

Chapter IV

Real-Time Dynamics of Clusters II. I_2X_n (n = 1; X = He, Ne, and H_2), Picosecond Fragmentation

4.1 Introduction

Chapter III, henceforth referred to simply as (III), presented our picosecond time-resolved studies of the dynamics of I_2Ne and I_2Ar clusters. In this chapter studies on the I_2He system are presented, as well as on the I_2H_2 and I_2Ne systems. Here, as in (III), the primary goal of these investigations is to understand the intramolecular vibrational-energy redistribution (IVR) and vibrational predissociation (VP) processes that occur within these clusters. For the simplest case as shown in Equation (1), the state-to-state rate of the reaction, $k(v'_i, v'_f)$, describes the dynamics of VP from the bound I_2 stretch (v'_i quantum number) potential to the translational continuum of the I_2 and X motion.

$$I_2^*X(v'_i) \xrightarrow{k(v'_i, v'_f)} I_2^*(v'_f) + X, \qquad (1)$$

The asterisk denotes the excited electronic B state, and X = He, Ne, Ar, or H_2, all with n=1. Our study of I_2X_n with n=2-4 will be discussed in the following chapter.

The experiments are performed using the picosecond pump-probe/molecular beam methodology.[2] The initial picosecond pump pulse prepares the cluster in a specific initial vibronic quantum state, $B(v'_i)$, of the complex. Energy transfer out of the iodine stretching coordinate into the van der Waals mode results in the fragmentation of the cluster. The picosecond probe pulse detects the nascent I_2 in its final $B(v'_f)$ vibronic state. For the cases of I_2He and I_2Ne, the energy of one quantum of the I_2 stretch mode exceeds the van der Waals binding energy, and the final I_2 fragment is liberated with v'_f=v'_i-1. The excess energy is converted into translational kinetic energy of the fragments and rotational excitation of the nascent I_2.

The measured rise of I_2 fragments in v'_f directly gives the state-to-state rate of VP. Since these rates are measured over a wide range of the initial quantum number v'_i, a number of theoretical models can be tested for their prediction of the absolute rates and their dependence on v'_i. The work on the I_2He system was performed with two primary

objectives in mind. First, in the extensive and pioneering work of Levy and coworkers[3] I_2He is the best spectroscopically characterized of all the I_2X clusters. The rotational structure of the complex was resolved and Levy and coworkers were able to obtain both the structure[4] of the complex and the linewidths.[5] From the linewidth measurements, assuming homogeneous broadenings, they deduced VP lifetimes[5] over the same range of v'_i levels that were measured in the set of experiments described in this chapter. Therefore, I_2He is an ideal system for comparison of the VP lifetimes obtained by both frequency and time-resolved methods.

Secondly, the I_2He results and those of the I_2Ne system provide two independent and calibrated sets of data which allow comparison with theoretical models of VP for the effects of mass and energy. The majority of these theoretical studies, including a quantum mechanical treatment of VP for a non-linear configuration, have focused on the I_2He system.

For example, the "energy-gap" model of Beswick and Jortner[6] predicts that the VP rate is dependent on the energy difference between the van der Waals bond energy and the vibrational level spacing of the I_2 stretching mode. Evidence from previous studies indicates that I_2He and I_2Ne clusters have similar structures, *i.e.*, "T"-shaped, and that both decay via one primary channel (unlike I_2Ar which undergoes electronic as well as vibrational predissociation). Therefore, in comparing the VP rates of I_2He and I_2Ne, aside from the He/Ne mass ratio, the major difference should be in their respective van der Waals potential well depths. This theory and others shall be considered below.

This chapter is organized as follows: the experimental methodology is described in Section 4.2, and the results are presented in Section 4.3. In Section 4.4 the dynamics of this system are discussed in the context of several proposed classical and quantum mechanical theories. Concluding remarks are presented in Section 4.5.

4.2 Experimental

The experiments were performed using a combination of picosecond laser and molecular beam techniques. Detailed descriptions of the experimental methodology and apparatus were presented in Chapter II, and will not be repeated here. The following is a brief summary and discussion of additional experimental conditions particular to the study of the I_2He system.

As in (III), two-color picosecond pulses were combined in a pump-probe configuration using a Michelson interferometer. The pump and probe beams were spatially overlapped on a dichroic beamsplitter and then gently focused (100 cm lens) to intersect the expansion 19 mm ($X/D = 125$) downstream from the nozzle. The probe was tuned to the $f \leftarrow B(v'_f)$ transition of the nascent I_2. Ultraviolet fluorescence from the ion-pair f state was detected and measured as a function of the time delay between the pump and probe pulses. Prior to the measurement of VP, the pump laser was tuned to the corresponding bare iodine $B(v'_f) \leftarrow X(v'_i = 0)$ transition while keeping the probe laser the same for the $f \leftarrow B(v'_f)$ transition. This established the overlap of the pump and probe pulses in both time and space, and set the proper conditions for probing nascent I_2. Temporal resolution in experiments of this nature is limited only by the cross-correlation between the pump and probe laser pulses. For the experiments reported here, the cross-correlations were approximately Gaussian in profile and the FWHM values were typically 40 ± 3 ps.

In order to enhance I_2He and I_2H_2 cluster formation in the molecular beam, high backing pressures (up to 160 psig) were required and a pulsed solenoid valve (150 mm diameter; General Valve series 9) with a 150 μm nozzle was used exclusively. The various clusters studied in this set of experiments, I_2He, I_2Ne, I_2Ar, and I_2H_2, were all formed in free jet expansions of helium (99.997% purity, Liquid Air), or neon (99.996% purity, Spectra Gases Inc.) with iodine (99.999% purity, Aldrich) seeded at room temperature vapor pressure. The carrier gases for I_2He and I_2Ne clusters, were neat

helium and neat neon respectively. Stagnation pressures for the I_2Ne experiments were typically 60 psig, while for the I_2He experiments they were 130-160 psig. [For I_2Ar see (I)]. The I_2H_2 experiments were performed with a mixture of ~3 % H_2 in helium at a stagnation pressure of approximately 160 psig. The ratio for this mixture was chosen to maximize the cluster signal.

Selective excitation of the desired cluster was extremely important as the expansion contained both bare iodine and the larger I_2X_n clusters. The spectroscopic studies of Levy and co-workers[3] proved invaluable in this regard. It was shown that for the I_2Ne_n clusters, where $n < 7$, the $B(v'_i) \leftarrow X(v'' = 0)$ transition is blue-shifted ($n \times 6.65$ cm^{-1}) from the corresponding bare I_2 transition. For I_2He_n clusters, the blue shift was shown to be $n \times 3.78$ cm^{-1}.

The picosecond lasers used in the experiments had a bandwidth of ~3 cm^{-1}; thus it was possible to tune the pump laser and selectively excite a given cluster to a given $B(v'_i)$ vibronic state. However, since the blueshift for the I_2He cluster is only 3.78 cm^{-1}, one may expect the "tail" of the pump laser to overlap the bare iodine $B(v'_i) \leftarrow X(v''=0)$ transition. If this were the case, the probe laser could, in principle, excite transitions from both the "incidental" bare iodine in the v'_i vibronic state and the nascent iodine in the v'_f state (produced by VP). Thus the I_2He (v'_f) transient would be contaminated with bare I_2 (v'_i) signal. To test for this contribution, the experiment was repeated for every I_2He (v'_i) level under identical conditions, except that the pure He carrier gas was replaced with pure Ne. Bare I_2 signal contamination in the transient would be unaffected by which of the two gases was used in the expansion. Since these test experiments showed no signal when He was replaced by Ne, the integrity of the observed I_2He transients was confirmed.

Another possible difficulty might arise because the transitions for I_2He and I_2Ne for a given v' are only 2.87 cm^{-1} apart. Given the bandwidth of the laser, it is possible to excite one species' transition while tuned to the maximum of the other. However, since

only neat helium or neon were used, I_2He and I_2Ne are not present in the molecular beam together during a single experiment.

4.3 Results

The state-to-state lifetimes and rates for the I_2Ne and I_2Ar systems have been presented in (III) and are listed again in Table 1 for comparison with the results for the I_2He system. Figure 1 shows a typical transient of I_2He and Figure 2 shows transients of the I_2He and I_2Ne system for the quantum number $v'_i = 22$. The time constants (τ) were determined by fitting the transients to an exponential rise convoluted with a Gaussian system response function. The fitting procedure was based on a Marquardt non-linear least-squares fitting routine,[7] and no parameters were fixed other than the cross-correlation bandwidth. A baseline slope factor was included when fitting some of the transients, particularily for those with low v'_i values which required longer scans. For both the I_2He and the I_2Ne fits, the zero of time was consistent with those obtained from bare I_2 control scans; there is no evidence of an induction period within the time resolution of our experiments. The measured values of τ as a function of v'_i for I_2He are shown in Figure 3 (and listed in Table 1), along with the values obtained by Levy from linewidth measurements.[5] Note that the reported values of τ are the average of a number of independent measurements for a given v'_i; the reported errors are one standard deviation.

The rates of vibrational predissociation $k(v'_i, v'_f)$ in equation (1) are taken as the inverse of the measured τ values (see Table 1). The v'_i dependence of $k(v'_i;v'_f)$ is shown in Figure 4 for both the I_2He and I_2Ne systems.

As with I_2Ne, [see (III)], rotational recurrences were observed in the I_2He transients. These recurrences correspond to the nascent I_2^* (v'_f). For all of the recorded transients, the pump and probe lasers had parallel polarizations; the observed recurrences were in accord with this arrangement.[8] The recurrences indicate that VP is sufficiently fast such that rotational coherence was retained in the products. Hence, there is a separation

in the timescales of VP and the rotational motion, a point of interest which has been discussed in (III).

Preliminary investigations of the vibrational predissociation rates in the I_2H_2 system have also been undertaken. A transient is shown in Figure 5 for v'_i=17 and v'_f=16. Levy and coworkers[9] reported a value of D_e= 74.4 cm^{-1} for this cluster, which indicates a stronger bond than either the helium or neon bonds. The "energy-gap law"[6] (*vide infra*) would, therefore, predict a comparatively larger VP rate,and this is the case. The VP lifetime for the I_2H_2 cluster at v'_i=17 is ~29 ps, while for I_2He or I_2Ne (Table 1) the times are 128 ps and 126 ps. The $I_2H_2(v'_i=17)$ lifetime of 29 ps is smaller than the 40 ps cross-correlation width of our laser system, and the lifetime is expected to decrease with increasing v'_i. Further measurements of I_2H_2 VP rates will thus require shorter pulse laser systems.[2]

In Figure 3, one can see a discrepancy between our real-time results for the τ of I_2He, and those values infered from the high-resolution spectroscopy measurements of Levy and coworkers. The linewidth measurements of the I_2He transitions give values of τ consistently shorter than the values obtained in our work, indicating that these transitions are broader than the intrinsic homogeneous VP width. As discussed in Reference 5, the rotational spectrum was not completely resolved in the high-resolution experiments and corrections had to be made for overlapping rotational bands as well as for Doppler broadening. Furthermore, the linewidth was obtained by fitting only the high-frequency side of the R-branch head. Given that the high-resolution spectroscopic data for I_2He required significant deconvolutions, it is reasonable to expect these discrepancies with our real-time measurements,[see (III) for the I_2Ne case]. It should be noted however, that both the real-time, and the high-resolution sets of data show similar nonlinear dependence of τ on v'_i.

4.4 Discussion

4.4.1 Real-time vs. Linewidth Measurements

As discussed previously,[1] homogeneous and inhomogeneous broadenings must be separated experimentally in order for linewidth measurements to give accurate rate values. Even if the transition is homogeneously broadened, pure dephasing[10] can lead to additional line broadening, although this effect is relatively minor in small systems near 0 K. A more serious problem results from the fact that the linewidth has no direct relationship to the rate of bond breakage if there is a dynamical process prior to the dissociation. This has been shown in other vdW complexes of large molecules.[11]

For small vdW clusters, such as I_2X, the system may have discrete level structure (an equivalent of the so-called intermediate level structure in radiationless transition theory[12]), and one should address the question of preparation of the state. In a recent communication,[13] Halberstadt, Beswick, Roncero, and Janda (HBRJ) discussed the "discrepancy" between time-resolved versus frequency-resolved measurements of the VP rate in relation to the preparation question. In order to understand this problem it is useful to consider the nature of the dynamics in a VP process.

In the simplest approach, VP is the result of coupling between the intramolecular (halogen stretch) and the intermolecular (vdW stretch) motion of the XBC cluster [here, X denotes the vdW-bound rare gas atom (*e.g.*, He), and BC represents the diatomic molecule (*e.g.*, I_2)]. The coupling is between the zero-order states which are direct products of BC stretch wave functions and the vdW stretch wave functions. These zero-order states are not eigenstates of the full Hamiltonian. If the BC stretch states are denoted by v', the bound vdW stretch states by l', and the vdW translational continuum states by ε', then there are two types of zero order states: $|v'_i, l'\rangle$ and $|v'_f, \varepsilon'\rangle$. The vdW continuum states are indexed according to their translational kinetic energy, which is determined by the following relationship:

$$\varepsilon' = E_{BC}(v'_i) - E_{BC}(v'_f) + \varepsilon_{l'}. \qquad (2)$$

$E_{BC}(v')$ is the energy of the BC v' state and $\varepsilon_{l'}$ is the vibrational energy of the vdW level $|l'\rangle$ corresponding to v'_i. For l'=0, $\varepsilon_{l'} = -D_0$(XB) as shown in Table 2. The effect of rotational excitation in nascent fragments has been neglected in Equation (2) . VP arises essentially from the coupling between a zero-order bound state, e.g., $|v'_i, 0\rangle$, and the quasi-degenerate translational continuum $|v'_f, \varepsilon'\rangle$. This discrete state/continuum coupling gives rise to a lifetime for the metastable resonance state and to homogeneous broadening of the initially prepared state. The zero-order picture for a system corresponding to I_2Ne or I_2He is shown in Figure 6a. The propensity rule for these systems is given by $v'_f = v'_i - 1$.

HBRJ consider[13] the Cl_2Ar system in its electronic B state. In this case, the propensity rule for VP is from v'_i to $v'_f = v'_i - 2$. The schematic vdW potential diagram is shown in Figure 6(b), and is to be contrasted with the corresponding picture for I_2He and I_2Ne in Figure 6(a). HBRJ found that at v'_i=10, the ground state vdW vibration is strongly coupled to energetically high lying (discrete) vdW vibrations of the v'=9 Cl_2 stretch level in Cl_2Ar. These states then, in turn, couple to the vdW translational continuum of the Cl_2 v'_f= 8 stretch level. The authors proposed a two-step mechanism, which is adopted in part from Reference 14. IVR in the sparse limit is assumed to be the first step. Dissociation from the levels obtained by mixing the zero-order light state $|s\rangle$ [direct product of the Cl_2 stretch (v'_i=10) and the corresponding vdW ground state] with the dark states $\{|k\rangle\}$ [a direct products of the Cl_2 stretch (v'=9) with corresponding high lying discrete vdW states] to the translational continuum $\{|\varepsilon'\rangle\}$ of the vdW states of the Cl_2 stretch v'_f= 8 occurs as the second step (VP1). HBRJ assumed that the light state predominantly couples to the dark states, which are in turn weakly coupled to the continuum; thus the direct coupling between the light state and the continuum (VP2) may

not be observed. This is the classic IVR problem and the preparation of the state is important for observation of the dynamics (phase-shifted quantum beats and decay).[15]

As noted by the authors,[13] a frequency domain experiment employing a CW laser with a very narrow bandwidth prepares the system in a molecular eigenstate, and not in a zero-order state. The linewidth Γ of this "scattering resonance" reflects the predissociation lifetime τ of a mixed state ($|s\rangle$ and $\{|k\rangle\}$) because the laser bandwidth is too small to observe IVR effects. The connection of τ to Γ is given by

$$\tau = \frac{\hbar}{\Gamma}. \qquad (3)$$

A time-resolved experiment with a coherent bandwidth prepares the system in a non-stationary (coherent) superposition of molecular eigenstates (e.g., in a zero-order state, $|s\rangle$). The $|s\rangle$ state then evolves to reveal the dynamics of both IVR and VP. In the case discussed by HBRJ, such a time-resolved experiment, spanning an energy band that includes at least one dark state, would give a combination of an IVR "rate" (with possible recurrences[15] in the sparse limit) and a VP rate, VP1. Thus, if the rises are fitted to a single exponential, an effective rate, which is slower than the pure VP1 rate, may result. As the VP rates reported for I_2Ne in (III) (and also those for I_2He reported in this chapter) are consistently smaller than those obtained from linewidth measurements, HBRJ concluded that I_2Ne might undergo IVR in the sparse limit, similar to Cl_2Ar.

Inspection of Figure 6(a) however, shows that the initial state $|s\rangle$ can only couple to the vdW translational continuum according to the propensity rule valid for I_2Ne and I_2He, *i.e.*, $v'_f = v'_i - 1$. The initial state prepared by the short laser pulse thus directly couples to the continuum; the only possible route for VP in I_2Ne and I_2He. This is also consistent with the fact that quantum beats, which may arise if IVR is in the sparse limit and precedes VP, are not observed. Also, as discussed below, the energy-gap law (in relative terms)

holds at least qualitatively for both I_2He and I_2Ne. A violation of the energy-gap law was, however, observed in Cl_2Ar (see Reference 13) for which the propensity rule is $v'_f = v'_i - 2$.

It is thus concluded that our real-time results give the VP rates, and the linewidth measurements provide an upper limit because of the reasons discussed above and in (III). However for I_2He it should be noted that, due to the good resolution of the rotational bands and the careful deconvolution of the linewidths,[5] the values for τ obtained from the high-resolution experiment have only a 30% discrepancy with our real-time results. Furthermore, the v'_i dependence of τ is still apparent. The situation is very different for more complex systems, such as I_2X_n of Chapter V, because the dynamics are controlled by more than one channel of VP.

4.4.2 Comparison with the Energy-Gap Law (EGL)

In order to rationalize the VP rates of triatomic vdW clusters, some simplifying rules have been devised theoretically. In particular, the EGL, derived by Beswick and Jortner,[6] and the momentum-gap law, derived by Ewing,[16] have been of considerable value in offering an understanding of the dependance of VP rates on v'_i. Beswick and Jortner[6] derived the EGL from an analytic expression obtained by (approximately) treating VP within the Fermi golden rule approach. After assuming a collinear configuration of the cluster and linearizing the vdW Morse potential with respect to the intramolecular coordinate, they obtained an expression for the halfwidth $\Gamma/2$. In (III), the EGL approach is discussed along with the dependence of Γ on the intramolecular (iodine), and intermolecular (iodine-rare gas) potentials. Γ is expressed as:

$$\Gamma = \frac{\pi}{4}\hbar\omega_{BC}\frac{\mu_{XBC}}{\mu_{BC}}v_i' \times \frac{(2K_{BC}-2v_i'+1)(2K_{BC}-2v_i'-1)}{[2K_{BC}(2K_{BC}-v_i')]}$$

$$\times \frac{\sinh(2\pi\theta_{\varepsilon'})}{\cos^2(\pi K_{XB})+\sinh^2(\pi\theta_{\varepsilon'})}\left|\tilde{\Gamma}(K_{XB}+\frac{1}{2}-i\theta_{\varepsilon'})\right|^2$$

$$\times \frac{2K_{XB}-2l'-1}{l'!\tilde{\Gamma}(2K_{XB}-l')} \qquad (4)$$

where $\tilde{\Gamma}$ denotes the gamma function. The symbols used in this equation and in the following expressions are explained in Table 2, and detailed in (III). BC denotes the halogen molecule and X the vdW-bound rare gas atom. The vdW potential is assumed to be of Morse-type. For large values of θ_ε equation (4) can be simplified to give:[6]

$$\Gamma = 2\pi^2\hbar\omega_{BC}\frac{\mu_{XBC}}{\mu_{BC}}v_i' \times \frac{(2K_{BC}-2v_i'+1)(2K_{BC}-2v_i'-1)}{[2K_{BC}(2K_{BC}-v_i')]}$$

$$\times \frac{N-l'-1}{l'!(2N-l'-1)!}\theta_{\varepsilon'}^{2N-1}\exp(-\pi\theta_{\varepsilon'}). \qquad (5)$$

In the limit when $\theta_{\varepsilon'} >> 1$ (by orders of magnitude) and $v'_i < K_{BC}$, the exponential in equation (5) dominates and the EGL can be expressed as:

$$\Gamma \propto v_i' \exp(\gamma v'_i), \qquad (6)$$

where

$$\gamma = \pi\frac{[\mu_{XBC}(\hbar\omega_{BC}/2)]^{1/2}}{K_{BC}(\hbar\alpha_{BC})}. \qquad (7)$$

With the vdW potential parameters obtained by Levy and coworkers from their spectroscopic work,[17] θ_ε can be calculated for v'_i=20: $\theta_\varepsilon(I_2He)$=10.36, and $\theta_\varepsilon(I_2Ne)$=3.54 [cp. (III)]. For both systems, θ_ε is clearly greater than one, but only for I_2He does the approximation made in order to apply equation (5) (i.e., $\theta_\varepsilon >> 1$), appear to be justified. This is borne out by actually calculating the VP time using equations (4) and (5). For I_2He (v'_i=20), equation (4) yields 1.5 μs and equation (5) yields 23 μs. For I_2Ne (v'_i=20), equation (4) leads to 2.6 ps and equation (5) gives 2.8 ns [cp. (III)]. The results for I_2He are closer in value to each other than those for I_2Ne, perhaps justifying approximation (5) for the He system.

In order to compare the v'_i dependence of the experimental VP rates with the behavior predicted by the EGL, our results are fitted to the functional form:

$$\frac{1}{\tau} \propto v_i' \exp(\gamma v_i'). \qquad (8)$$

For I_2He, this yields γ=0.0579 which corresponds to a Morse length parameter of $\alpha = 1.81$ Å^{-1}; for I_2Ne, γ=0.0936, corresponding to α=2.43 Å^{-1} [cp. (III)]. The fits, shown together with our experimental data in Figure 7 do indeed demonstrate the expected trend α(He) < α(Ne). This expectation is based on the *effective* Morse potential parameters derived by Levy and coworkers from careful spectroscopic work on I_2He and I_2Ne in the electronic *B* state.[17] Note that while the overall behavior is correctly described by the fits to equation (8), the absolute magnitudes of the rates derived by the EGL [equations (4), (5)] are orders of magnitude different from the experimental result

The data was also fitted to the simpler exponential expression

$$\frac{1}{\tau} \propto \exp(\gamma v_i'). \qquad (9)$$

These fits, shown in Figure 8, lead to γ=0.1098 for I_2He (corresponding to α=0.95 Å^{-1}), and to γ=0.1493 for I_2Ne (corresponding to α=1.52 Å^{-1}). The change in α between I_2Ne and I_2He is still the same, so it appears that the intermolecular term (the exponential) dominates the behavior of the v'_i dependence.

In order to compare the v'_i behavior in our data with those obtained from linewidth measurements, the functional form for I_2He used by Levy and coworkers is invoked:[5]

$$\frac{1}{\tau} = A(v_i')^2 + B\ (v_i')^3. \qquad (10)$$

The values obtained by Levy and coworkers, fitting the halfwidths of the observed bands (not $1/\tau$), were A=5.55 × 10^{-4} and B=1.74 × 10^{-6}, which when translated into equation (10) (i.e., $1/\tau$ instead of $\Gamma/2$) give A=2.09 x 10^7 and B=6.555 x 10^5. For the purpose of a more accurate comparison, the $1/\tau$ data deduced from Reference 5 was refitted using a Marquardt nonlinear least squares algorithm.[7] Instead of the above values, we arrived at A=2.646 × 10^7 and B=3.969 × 10^5. These results were reproduced using a Simplex routine.[18] Replacing the correct (error-weighted) χ^2 by the sum of squared differences between the observed and the calculated data, however, led to the results that Levy and coworkers reported. Thus, it seems that the fits that these authors performed were unweighted, leading to slightly different results. In order to keep the comparison consistent, only the values obtained from the weighted fits of the linewidth data will be used, (A=2.646 × 10^7 and B=3.969 × 10^5).

The parameters obtained for the real-time experimental data of I_2He were A = 2.423 × 10^7 and B=1.594 × 10^5. A comparison of the two fits together with the corresponding experimental data is shown in Figure 9. It appears that for the fits in this study, the quadratic term dominates with respect to the cubic term, which is slightly

different from the fits to the linewidth data,[5] when considering the relative *A/B* values. This may be due to the fact that the latter data were obtained for vibrational levels up to 26. If the data for levels 12-16 and 24-26 are discarded, the coefficient for the cubic term becomes even higher than when fitting to the full data set; the quadratic term is nearly equal to that in our data. Thus, the VP rates given in Reference 5 still appear to rise a little faster with respect to v'_i than that obtained from the real time data, but the differences are minor. It is concluded that while the linewidth data lead to consistently larger VP rates than the real-time results, both show a very similar nonlinear behavior with respect to v'_i. An analogous fit of the real-time data of I_2Ne (v'_i=13-23) gives $A=9.890 \times 10^6$ and $B=1.111 \times 10^6$ and is depicted in Figure 10. These results show that the VP rates of I_2Ne rise (with v'_i) faster than those of I_2He, as expected from theory.

This faster rise for the I_2Ne system cannot, however, be explained only by the simple reduced mass considerations (see Reference 19 for a discussion). In order to observe the mass effect, the molecular properties which characterize the dimensionless parameter θ_ε (α and ε'), given above and in Table 2, must not change appreciably between the I_2He system and the I_2Ne system. In addition, the effect of the reduced mass appearing in the preexponential factor [see equation (5)] should be negligible. If these conditions and the assumptions leading to equation (5) (*e.g.*, collinear configuration of the cluster) are met, then it is predicted[19] that the VP rate, at least for high quantum numbers l', becomes larger when the mass of the rare gas atom is decreased. This is exactly opposite to the behavior observed within the range of v'_i quantum numbers covered in our experiments. The contradiction is not too surprising as the potential parameters are appreciably different for the I_2He and the I_2Ne systems. However, a logarithmic correlation between the VP time and the parameter $\theta_\varepsilon = (2\mu_{XBC}\,\varepsilon')^{1/2}/\alpha_{XB}\hbar$ itself, as proposed by Ewing[16] (momentum-gap law), appears to point along the right direction, although the actual values of the correlation are not reproduced at all. With the values for α and D_0 obtained by Levy and coworkers[17] [$\alpha(I_2He) = 0.41$ Å^{-1}, $D_0(I_2He) = 14.2$ cm^{-1};

$\alpha(I_2Ne) = 1.5$ Å^{-1}, $D_0(I_2Ne)$=66 cm^{-1}] we calculate for v'_i=20 that $\theta_\varepsilon(I_2He)$ is about 2.9 $\theta_{\varepsilon'}(I_2Ne)$ (*vide supra*), wheras $\ln[t_{VP}(I_2He)] = 1.04 \ln[\tau_{VP}(I_2Ne)]$. When $\alpha(I_2He) = 1.14$ Å^{-1}, a value used in most theoretical calculations for the I-He Morse potential (*vide infra*), and the values of all other parameters are kept the same, one obtains a value of 1.04 instead of 2.9 for θ_ε.

4.4.3 Comparison with Classical and Quantum Calculations

A comparison is made in (III) of the experimental results for I_2Ne with the numerical calculations performed by a number of research groups. Here, the focus is on the I_2He system. Calculations of the VP rates of I_2He in its electronic *B* state have been performed for collinear and nonlinear cluster geometries. As the T-shaped configuration of I_2He is most likely,[4] only the numerical results for a nonlinear configuration will be considered.

The results of any calculation addressing VP of vdW systems crucially depend on the parameters used for the assumed sum of two halogen-atom/rare-gas-atom Morse potentials (the form of the long range part of the vdW potential does not appear to be very important).[20] These Morse potential parameters should be compared to the *effective* ones deduced by Levy and coworkers;[17] from fits of spectroscopic data they obtained the following parameters for a Morse potential (I_2He, *B* state): D_{XB}= 13.6-14.8 cm^{-1} and an effective α=0.4-0.42 Å^{-1}. When comparing these α values with those used in theory (most often α_{XB}=1.14 Å^{-1} and D_{XB} = 18 cm^{-1}) one must keep in mind the difference: the α values used in theory are those for each of the two atom-atom potentials, whereas the values obtained from experiment[17] are for a single effective Morse potential along the vdW stretch coordinate.

The first calculation which employed a fixed T-shaped configuration was performed by Beswick and Jortner in 1978.[21] They calculated VP rates within the close-coupling framework, i.e., by numerically solving the coupled differential equations

obtained by invoking a basis set expansion in the Schrodinger equation and calculating the appropriate scattering matrix elements. With D_{XB}=7 cm^{-1} and α=1.25 $Å^{-1}$, they obtained a VP time of ca. 835 ps for v'_i=20 (l'=0), whereas changing D_{XB} to 25 cm^{-1} yielded a value of 67 ps, closer in magnitude to our experimental result of 94 ps. The I_2 stretch vibration was treated with a harmonic approximation, and the calculated results depended on the potential parameters.

Beswick, Delgado-Barrio, and Jortner[20] included the anharmonicity of the I_2 stretch vibration into their close-coupling formalism. They obtained for v'_i=20 (l'=0, D_{XB}=7 cm^{-1}, α = 1.24 $Å^{-1}$) a VP time of ca. 240 ps, thus drastically reducing the above result of 835 ps obtained with the same parameters but without the anharmonicity of the intramolecular mode. Changing D_{XB} to 13 cm^{-1} led to a VP time of 80 ps, also close to our experimental result of 94 ps.

In 1980, Beswick and Delgado-Barrio[22] added a treatment of rotations into the DDW scheme. The rotations were treated within the infinite-order sudden approximation (IOSA). From Figures 3 and 4 of Reference 22, the following results for v'_i=20 (l'=0) can be extracted: With D_{XB}=7 cm^{-1} and α=1.24 $Å^{-1}$, the VP time was calculated to be ca. 775 ps; with D_{XB}=18 cm^{-1} and α=1.14 $Å^{-1}$, the result was 265 ps. These authors also calculated the rotational excitation of the fragment I_2 during VP and found it to be very minor, indicating a vibrational-translational process.

Recently, a three-dimensional quantum wave packet calculation of VP in I_2He was reported by Zhang and Zhang.[23] They also found that, while the rotational state distribution of the nascent I_2 is independent of v'_i and is restricted to low rotational levels, the rates become much smaller when compared with the results of the two-dimensional (non-rotating, fixed T-shaped geometry) calculations. The Morse potential parameters the authors used were D_{XB}=18 cm^{-1} and α=1.24 $Å^{-1}$. From Figure 1 of Reference 23, a VP time of about 115 ps can be extracted for v'_i=20, which is close to our experimental value of 94 ps.

In order to facilitate the computational effort and to be able to treat larger systems, quasiclassical trajectory methods were introduced for the calculation of VP lifetimes. A classical approximation seems inappropriate for this inherently quantum mechanical process since I_2 releases energy into the vdW bond via quantized doses rather than by continuous relaxation. Nevertheless, a quasiclassical trajectory calculation by Delgado-Barrio and coworkers[24] was performed for I_2He (v'_i=23, l'=0, no bending excitation, overall angular momentum J=0) which gave rise to a VP time of about 65 ps (extracted from Figure 2 of Reference 24). They used D_{XB}=18 cm^{-1} and α=1.14 $Å^{-1}$. This result is identical with the VP time measured for v'_i=23 in our experiment.

Recently, statistical methods based on quasiclassical trajectory calculations were developed by Davis, Gray, Rice, and coworkers.[25-30] Within the framework of these methods, which invoke concepts from nonlinear dynamics, "intermolecular bottlenecks" in phase space are defined as dynamic transition states of fragmentation. The rates of VP are obtained by calculating the flux of phase points across the intermolecular bottleneck. These methods work better at higher v'_i values. For low v'_i levels, the rates across "intramolecular bottlenecks", which lie within the intermolecular ones, become rate limiting and gain importance.

Davis and Gray[26] calculated the VP rates of T-shaped I_2He (two coordinate system) by considering the flux of phase points across the exact intermolecular bottleneck. Using D_{XB}=18 cm^{-1}, α=1.14 $Å^{-1}$ they obtained, for v'_i=20, a VP time of 14 ps. A numerical (classical trajectory) simulation led to a value of 31 ps. Including one intramolecular bottleneck, they obtained a statistically calculated VP time of 31 ps which matches the result of the numerical simulation.

The alternative RRKM (ARRKM) method[27] considers an approximate intermolecular bottleneck. Gray, Rice, and Davis calculated the VP time of T-shaped I_2He[28] for v'_i=20; using D_{XB}=18 cm^{-1}, α=1.14 $Å^{-1}$, they obtained 6.5 ps. With a calculation of the flux of phase points across the approximate intermolecular bottleneck,

they obtained a VP time of 8 ps. These results appeared to be in fairly good agreement with those obtained employing the exact intermolecular bottleneck. Inclusion of rotations into the ARRKM method leads, however, to a considerable deviation of the results when compared with classical trajectory calculations and experimental data. For v'_i=20, and with the overall angular momentum fixed at J=0, Gray, Rice and Davis calculated a VP time of 3.5 ps.[27]

Very recently, Zhao and Rice[29,30] extended the ARRKM method by defining rovibrational state-dependent bottlenecks which take into account the actually excited initial state. The method emerging from these considerations has been termed modified RRKM (MRRKM) theory. Using the same parameters, *i.e.*, D_{XB}=18 cm^{-1}, α=1.14 Å^{-1}, they performed several MRRKM calculations[30] for both I_2He and I_2Ne. For v'_i=20, the VP time for I_2He (when only the intermolecular bottleneck is accounted for and the geometry is fixed, nonrotating, and T-shaped) was calculated to be 13.5 ps. Allowing for rotations, but keeping the overall angular momentum J=0, these authors calculated a VP time of 41 ps. They also calculated the VP time considering only the intramolecular bottleneck and keeping the cluster in a fixed T-shaped configuration and obtained 20 ps. Including the intermolecular bottleneck yielded 22 ps. Finally, after allowing for rotation, keeping J=0, and taking into consideration the intra and intermolecular bottlenecks, they obtained a VP time of 62 ps, which is closer to the experimental value of 94 ps.

As noted above, the influence of rotations is significant. Even though the rotational excitation of the departing I_2 fragment is negligible, the inclusion of rotations has a profound effect on the calculation of the absolute rates. It appears that VP rate calculations have to take into account such effects. The influence of overall rotations on microcanonical rates has been observed experimentally[31] and calculated theoretically[32] in other cases where a chemical bond is broken to form two fragments (*e.g.*, $NCNO \longrightarrow NC + NO$). The effect is more dramatic near threshold energies. Further quantum calculations using the wave packet approach are underway[33] and it would be

interesting to include the effect of rotations. Also, it seems worthwhile to study in depth the applicability of classical models to these systems where quantum effects are expected to influence the dynamics.

Table 3 summarizes the comparison of results of all theories available and the experimental results reported here, focusing on $v'_i = 20$ for the above discussion.

4.5 Conclusions

The present chapter addressed two main issues concerning the picosecond dynamics of vibrational predissociation (VP) in small van der Waals (vdW) clusters. First, by studying the VP of I_2He in real-time, results were presented for a rare system where linewidth-deduced and real-time VP rates are directly comparable. From this comparison, it was found that the linewidth-deduced data led to consistently higher rate values. The discrepancy is more pronounced for I_2Ne, and for larger clusters (chapter V) the linewidth measurements cannot separate the dynamics of the two VP pathways. These results were discussed in relation to the origin of the line broadening and to the question of preparation of the state. The VP rate dependence on the quantum number of the I_2 stretch vibration in I_2He was measured and both methods display the highly nonlinear behavior.

Secondly, the experimental results on I_2He and I_2Ne were compared with a variety of theoretical approaches (classical, quantum and semiclassical) in an attempt to understand the forces controlling the dynamics. Theories for calculating VP rates of small vdW clusters are quite advanced, and it is important to critically examine the predictions of the different approaches. The repulsive force of the potential of the vdW interaction plays a key role and the theoretical results depend crucially on such input parameters.

While theories agree with each other on the quantum state dependence of the rates, they differ in their prediction of the absolute rate values by orders of magnitude. The dependence of the state-to-state rates on the initial vibrational quantum number can be understood using the energy-gap law as well as a number of other numerical methods.

The energy-gap law, however, does not provide the absolute rate. A simple model[34] can deduce such dependencies by considering the repulsive force of the potential in the reverse problem of T-V transfer (full collision).

Methods based on classical concepts are now used to calculate VP rates. Why methods such as the MRRKM by Rice and coworkers[29,30] deduce rates in quantum systems (defined by the initial quantum number of the vibrations and their discrete energies) is an interesting question. If generalized and tested against quantum calculations, these methods could prove useful for larger systems with increased numbers of degrees-of-freedom, a transition made in Chapter V of this thesis, where n is greater than one for I_2He_n and I_2Ne_n.

4.6 References

1. D. M. Willberg, M. Gutmann, J. J. Breen, and A. H. Zewail, J. Chem. Phys. **96**, 198 (1992).

2. L. Khundkar and A. H. Zewail, Annu. Rev. Phys. Chem. **41**, 15 (1990) and references therein.

3. D. H. Levy, Adv. Chem. Phys. **47**, part I, 323 (1981) and references therein.

4. R. E. Smalley, L. Wharton, D. H. Levy, J. Chem. Phys. **68**, 671 (1978).

5. K. E. Johnson, L. Wharton, and D. H. Levy, J. Chem. Phys. **69**, 2719 (1978).

6. J. A. Beswick and J. Jortner, Adv. Chem. Phys. **47**, part I, 363 (1981) and references therein.

7. P. R. Bevington, *Data Reduction and Error Analysis for the Physical Sciences*, McGraw-Hill, New York (1969) pp. 204.

8. D. M. Willberg, J. J. Breen, M. Gutmann, and A. H. Zewail, J. Phys. Chem. **95**, 7136 (1991).

9. J. E. Kenny, T. D. Russell, and D. H. Levy, J. Chem. Phys. **73**, 3607 (1980).

10. A. H. Zewail, Acc. Chem Res. **13**, 360 (1980).

11. D. M. Semmes, J. S. Baskin, and A. H. Zewail, J. Chem. Phys. **92**, 3359 (1990).

12. For a review see: J. Jortner and S. Mukamel in *The World of Quantum Chemistry*, R. Daudel and B. Pullman eds., Reidel, Dordrecht (1976), pp. 205.

13. N. Halberstadt, J. A. Beswick, O. Roncero, K. C. Janda, J. Chem. Phys. **96**, 2404 (1992).

14. W. R. Gentry, in *Structure and Dynamics of Weakly Bound Molecular Complexes*, NATO ASI series, A. Weber ed., D. Reidel, Dordrecht (1987), pp. 467.

15. P. M. Felker and A. H. Zewail, Adv. Chem Phys. **70**, part I, 265 (1988).

16. (a). G. E. Ewing, J. Chem. Phys. **71**, 3143 (1979); (b). G. E. Ewing, J. Chem. Phys. **72**, 2096 (1980); (c). G. E. Ewing, Farad. Discuss. Chem. Soc. **73**, 325, 402 (1982); (d). G. E. Ewing, J. Phys. Chem. **90**, 1990 (1986).

17. J. A. Blazy, B. M. DeKoven, T. D. Russell, and D. H. Levy, J. Chem. Phys. **72**, 2439 (1980).

18. This program was based on an algorithm from M. Caceci and W. P. Cacheris, BYTE, pp. 340, (May 1984).

19. J. A. Beswick and J. Jortner, J. Chem. Phys. **68**, 2277 (1978).

20. J. A. Beswick, G. Delgado-Barrio, and J. Jortner, J. Chem. Phys. **70**, 3895 (1979).

21. J. A. Beswick and J. Jortner, J. Chem. Phys. **69**, 512 (1978).

22. J. A. Beswick and G. Delgado-Barrio, J. Chem. Phys. **73**, 3653 (1980).

23. D. H. Zhang, and J. Z. H. Zhang, J. Phys. Chem. **96**, 1575 (1992).

24. G. Delgado-Barrio, P. Villerreal, P. Mareca, and G. Albelda, J. Chem. Phys. **78**, 280 (1983).

25. M. J. Davis, J. Chem. Phys. **83**, 1016 (1985).

26. M. J. Davis, and S. K. Gray, J. Chem. Phys. **84**, 5389 (1986).

27. S. K. Gray, and S. A. Rice, Farad. Discuss. Chem. Soc. **82**, 307 (1986).

28. S. K. Gray, S. A. Rice, and M. J. Davis, J. Phys. Chem. **90**, 3470 (1986).

29. M. Zhao, and S. A. Rice, J. Chem. Phys. **96**, 3542 (1992).

30. M. Zhao, and S. A. Rice, J. Chem. Phys. **96**, 6654 (1992).

31. L. R. Khundkar, J. L. Knee, and A. H. Zewail, J. Chem. Phys. **87**, 77 (1987).

32. J. Troe, Ber. Bunsenges. Phys. Chem. **92**, 242 (1988).

33. S. K. Gray, private communication.

34. D. M. Willberg, M. Gutmann, E. E. Nikitin, and A. H. Zewail, Chem. Phys. Lett. **201**, 506 (1993).

Table 1. The measured (in real-time) state-to-state rates and lifetimes for the I_2He and the I_2Ne systems.*

v'_i	I_2He τ (ps)	I_2He VP rate ($\times 10^9$ s^{-1})	I_2Ne τ (ps)	I_2Ne VP rate ($\times 10^9$ s^{-1})
13			216 ± 16	4.6 ± 0.4
14			196 ± 12	5.1 ± 0.3
15			182 ± 20	5.5 ± 0.6
16			160 ± 15	6.3 ± 0.6
17	128 ± 2	7.8 ± 0.2	126 ± 12	7.9 ± 0.8
18	115 ± 9	8.7 ± 0.7	107 ± 9	9.3 ± 0.9
19	101 ± 4	9.9 ± 0.4	87 ± 4	11.5 ± 0.9
20	94 ± 4	10.6 ± 0.5	78 ± 4	12.8 ± 1.0
21	82 ± 4	12.2 ± 0.6	69 ± 6	14.5 ± 0.7
22	75 ± 6	13.3 ± 1.0	58 ± 3	17.2 ± 0.9
23	65 ± 5	15.6 ± 1.2	53 ± 3	18.9 ± 1.0

*In this table, the reported errors represent one standard deviation for a number of independent measurements.

Table 2. Definitions and expressions used in the theoretical calculations of vibrational predissociation rates.

D_{XB}	Potential well depth
$\omega_{XB} = \left(\frac{1}{\mu_{X,BC}} \left(\frac{\partial^2 U}{\partial Q^2} \right)_{Q_0} \right)^{1/2}$	Characteristic Morse frequency
$\mu_{X,BC} = \frac{m_X (m_B + m_C)}{m_X + m_B + m_C}$	Reduced mass of the complex
$\alpha_{XB} = \omega_{XB} \left(\frac{\mu_{X,BC}}{2 D_{XB}} \right)^{1/2}$	Characteristic inverse length
$K_{XB} = \frac{2 D_{XB}}{\hbar \omega_{XB}}$	Anharmonicity of the vdW vibration
$\varepsilon_{l'} = -D_{XB} + \hbar \omega_{XB} \left(l' + \frac{1}{2} \right) \left(1 - \frac{\left(l' + \frac{1}{2} \right)}{2 K_{XB}} \right)$ $= \frac{\hbar^2 \alpha_{XB}}{2 \mu_{X,BC}} \left(K_{XB} - l' - \frac{1}{2} \right)^2$	Energy of the bound state $\lvert l' \rangle$
$\theta_{\varepsilon'} = \frac{\left(2 \mu_{X,BC} \varepsilon' \right)^{1/2}}{\hbar \alpha_{XB}} = \frac{2 \left(D_{XB} \varepsilon' \right)^{1/2}}{\hbar \omega_{XB}}$	Energy parameter
$N = \left(K_{XB} + \frac{1}{2} \right)$	Number of bound states in the Morse potential[a]
$\mu_{BC} = \frac{m_B m_C}{m_B + m_C}$	Reduced mass of B-C
ω_{BC}	Frequency of the B-C stretch vibration
$K_{BC} = \frac{\omega_{BC}}{2 (\omega x_e)_{BC}}$	Anharmonicity of the B-C stretch vibration

[a] The value obtained for N in this expression needs to be rounded off to an integer value.

Table 3. Theoretical predictions of the vibrational predissociation lifetime of I_2He (v'_i = 20, I' =0). The experimental value from this work is 94 ± 4 ps.

Method[a,b]	D_{XB} (cm^{-1})	α_{XB} ($Å^{-1}$)	τ (ps)	2D/3D[c]	Ref.
Close coupling	7	1.25	835	2D	21
(I_2 stretch is treated	25	1.25	67	2D	
harmonically)					
Close coupling	7	1.24	240	2D	20
(I_2 stretch is treated	13	1.24	80	2D	
anharmonically)					
DDW + IOSA	7	1.24	775	3D	22
	18	1.14	265	3D	
Quantum Wave Packet	18	1.14	115	3D	23
Classical Trajectory	18	1.14	65 (v'_i=23)	3D	24
Classical Trajectory	18	1.14	31	2D	26
Flux across exact	18	1.14	14	2D	
intermolecular bottleneck					
ARRKM	18	1.14	6.5	2D	28
Flux across approximate	18	1.14	8	2D	
intermolecular bottleneck					
ARRKM	18	1.14	3.5	3D	
MRRKM	18	1.14	13.5	2D	30
(intermolecular bottleneck)	18	1.14	41	3D	
MRRKM	18	1.14	20	2D	
(intermolecular bottleneck)					
MRRKM	18	1.14	22	2D	
(intermolecular and	18	1.14	62	3D	
intramolcular bottleneck)					

[a] Abbreviations in this table are explained in the text.

[b] Calculations according to Equation (4) in the text are not included in this table as this equation was derrived analytically for a linear complex.

[c] 2D corresponds to a fixed *T*-shaped geometry not allowing for rotational or bending motion, 3D differs from 2D by inclusion of rotational and bending motion.

4.7 Figure Captions

1. Shown is a typical transient obtained for the $v'_i = 22/v'_f = 21$ experiments: (top) is a bare I_2 ($v' = 22$) transient obtained for calibration; (middle) is a transient showing the predissociation ($\tau = 53$ ps); and (bottom) the visible cross-correlation of the pump and probe lasers. The dashed line shows a fit to an exponential rise function.
2. Transients of I_2He and I_2Ne predissociation obtained when the same vibronic level ($v'_i = 22$) is excited. The dashed lines show fits to an exponential rise function convoluted with a Gaussian system response. The VP lifetimes are found to be 75 ± 6 ps for I_2He, and 58 ± 3 ps for I_2Ne.
3. The VP lifetimes obtained from the real-time studies reported in this chapter (squares), and the lifetimes estimated from linewidth measurements (triangles) presented in Reference 5.
4. The rate of vibrational predissociation for I_2He and I_2Ne as a function of the vibrational level v'_i excited.
5. Shown is a typical transient obtained for the VP of I_2H_2 ($v'_i = 17/v'_f = 16$): (top) is a bare I_2 ($v' = 16$) transient obtained for calibration; (middle) is a transient showing the predissociation; and (bottom) the visible cross-correlation of the pump and probe lasers. The dashed lined shows a fit to an exponential rise function convoluted with a Gaussian system response
6. (a) A schematic of the vdW potential for VP in the I_2He and I_2Ne systems along the intermolecular coordinate. The vdW translational continuum corresponding to v'_f is shown as a block. (b) Same as (a) but for Cl_2Ar. The zero-order states are not explicitly labeled. For details, see text.
7. Theoretical fits of the real-time VP rates to the energy-gap-law expressed in Equation (8). The experimental data and the reported error bars are also shown. The open squares are for I_2Ne and the filled squares are for I_2He. The vibrational levels on the abscissa correspond to v'_i.

8. Same as Figure 7 except that the fits are made to the simple exponential function given in Equation (9).
9. Theoretical fits of the real-time VP rates and the linewidth deduced VP rates (Reference 5) for I_2He to Equation (10). The experimental data together with reported error bars are given. The real-time data are shown as filled squares and the linewidth data as open squares. The vibrational levels on the abscissa correspond to v'_i.
10. Theoretical fits of the real-time VP rates of I_2He and I_2Ne to Equation (10). The experimental data and the reported error bars are shown. The open squares are for I_2Ne and the filled squares are for I_2He. The vibrational levels on the abscissa correspond to v'_i.

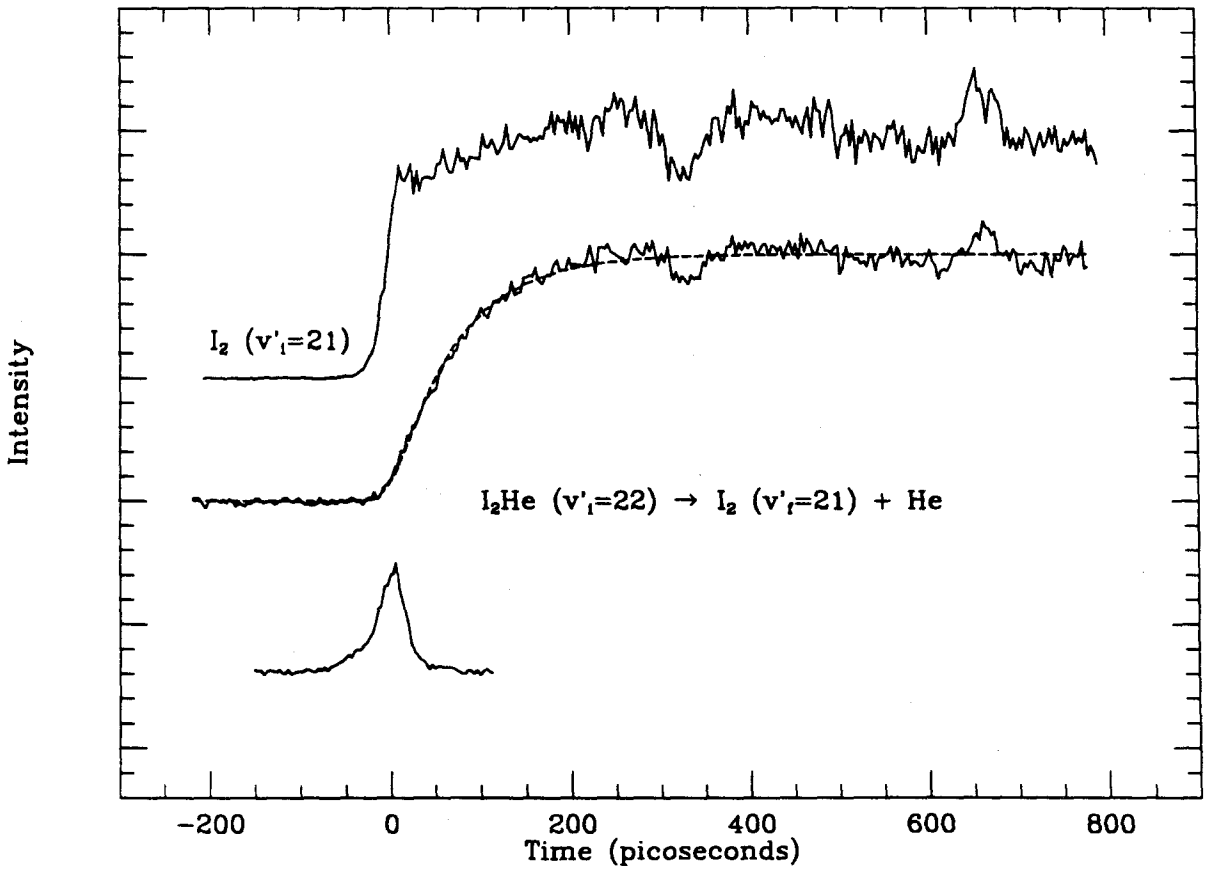
Intensity
I_2 (v'_i=21)
I_2He (v'_i=22) → I_2 (v'_i=21) + He
−200
0
200
400
600
800
Time (picoseconds)

Figure 1

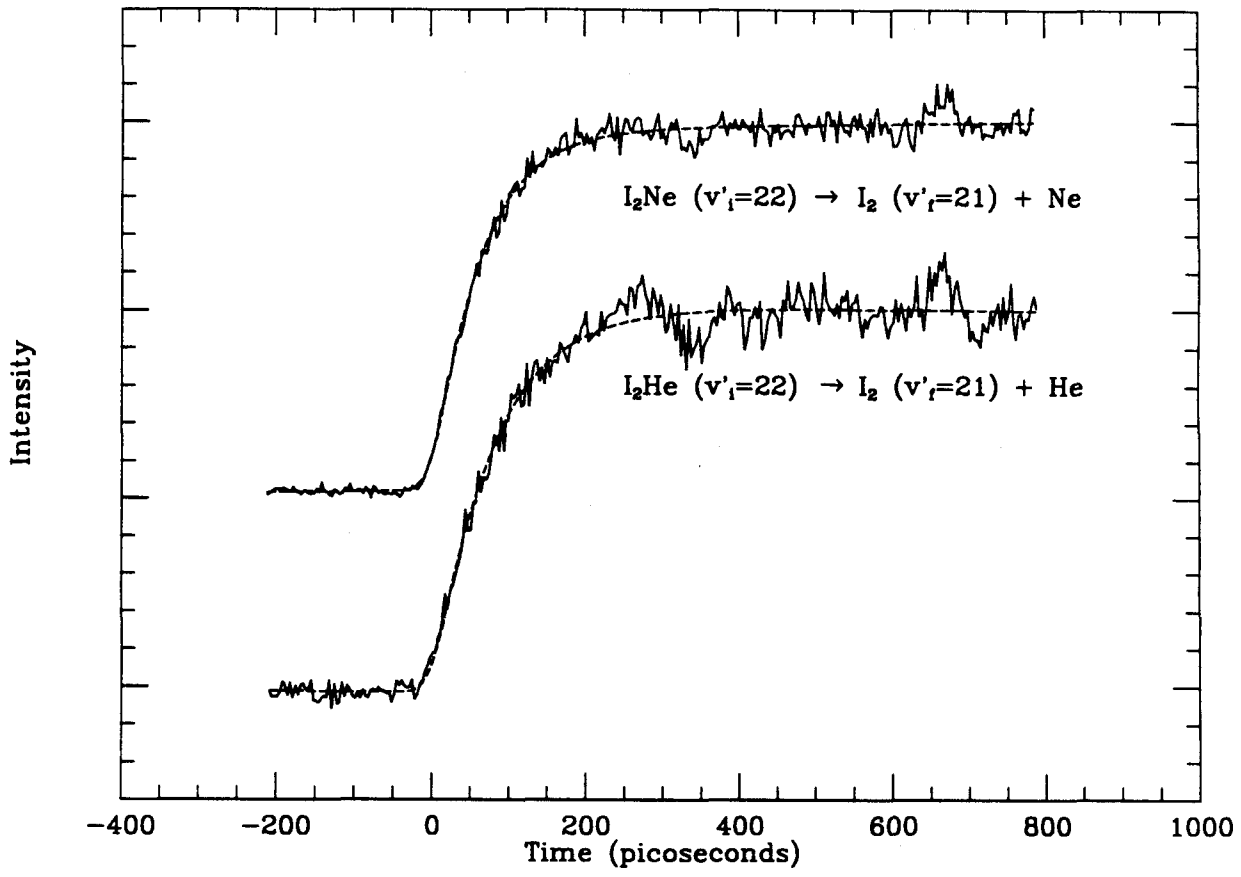
Intensity
I_2Ne (v'_i=22) → I_2 (v'_f=21) + Ne
I_2He (v'_i=22) → I_2 (v'_f=21) + He
−400
−200
0
200
400
600
800
1000
Time (picoseconds)

Figure 2

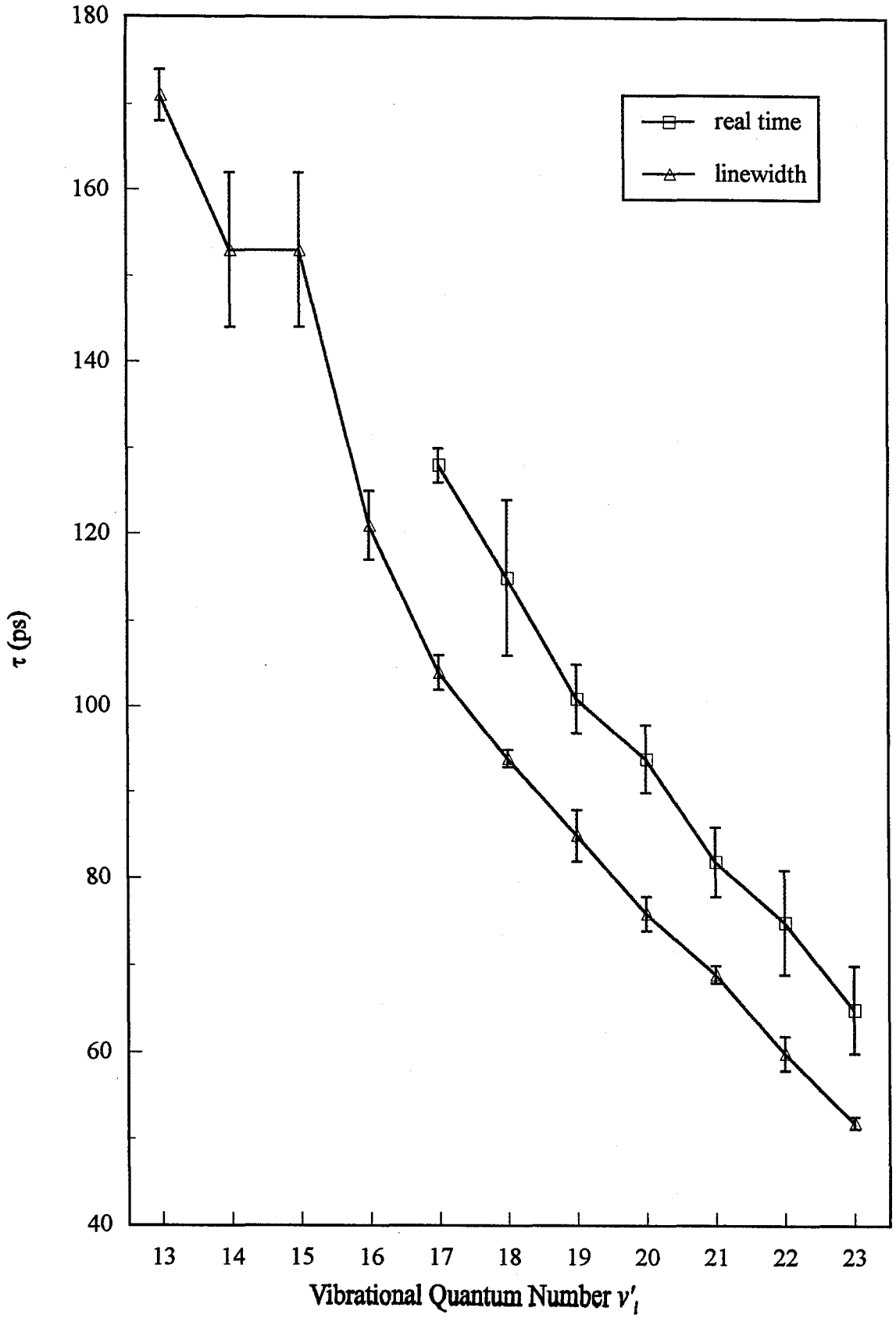
real time
linewidth
τ (ps)
180
160
140
120
100
80
60
40
13
14
15
16
17
18
19
20
21
22
23
Vibrational Quantum Number v'_1

Figure 3

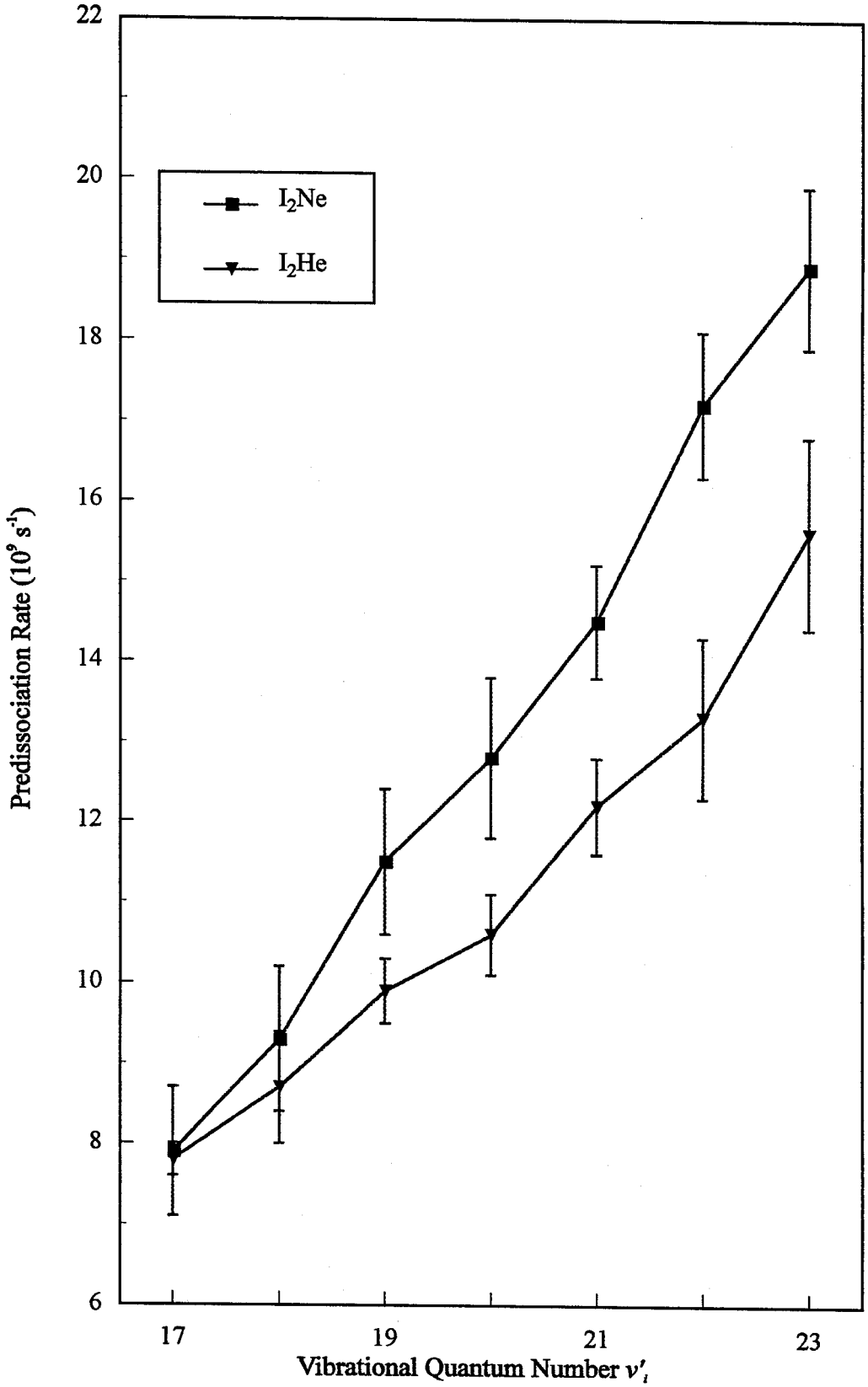
22
20
18
16
14
12
10
8
6
I2Ne
I2He
Predissociation Rate (10^9 s^-1)
17
19
21
23
Vibrational Quantum Number v'i

Figure 4

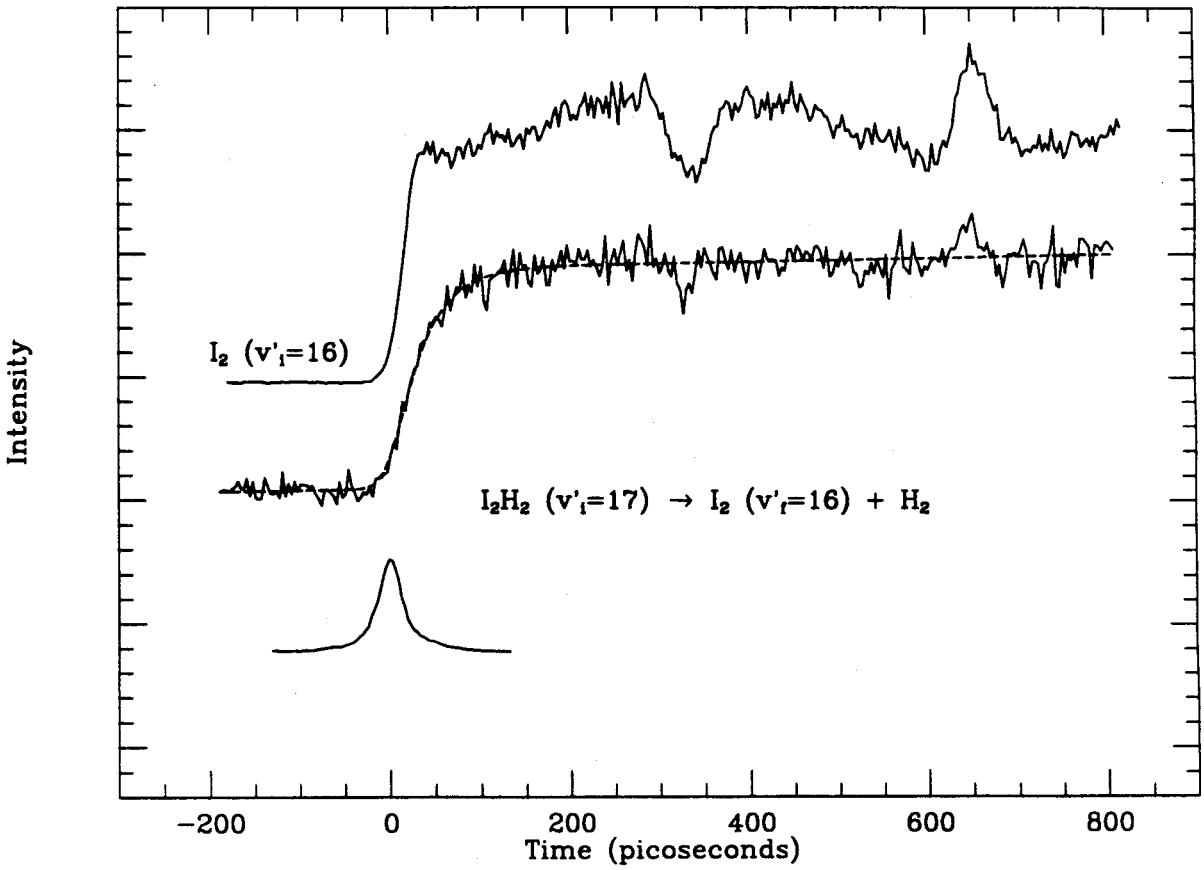
Intensity
I_2 (v'_i=16)
I_2H_2 (v'_i=17) → I_2 (v'_i=16) + H_2
−200
0
200
400
600
800
Time (picoseconds)

Figure 5

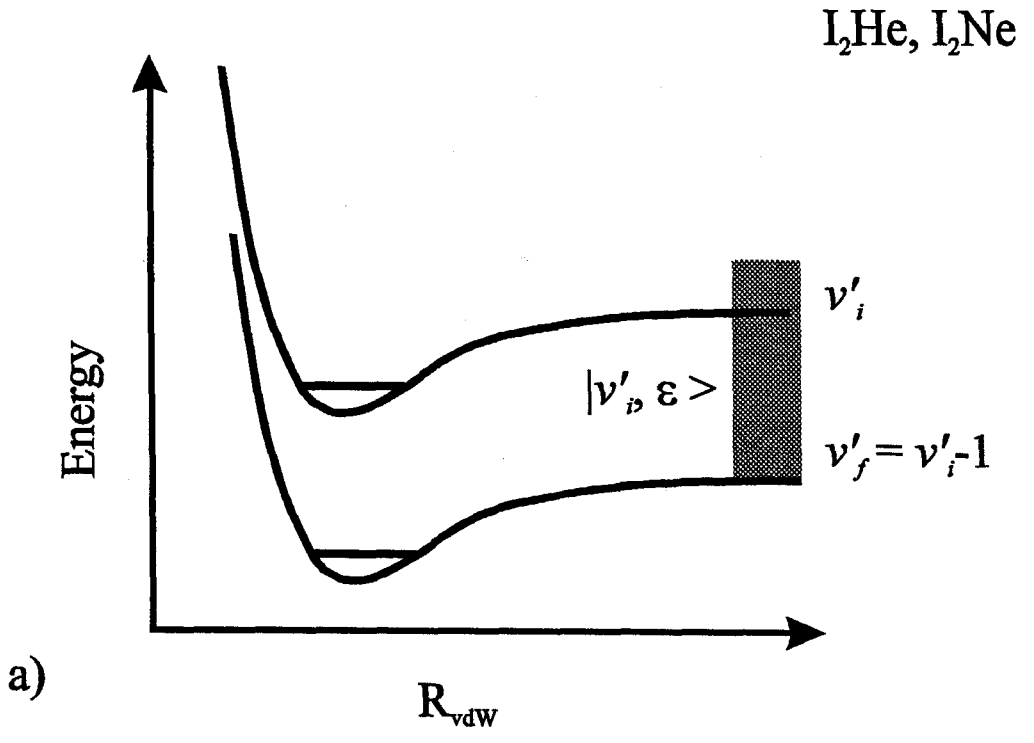
I2He, I2Ne
Energy
v'i
|v'i, ε >
v'f = v'i-1
a)
RvdW

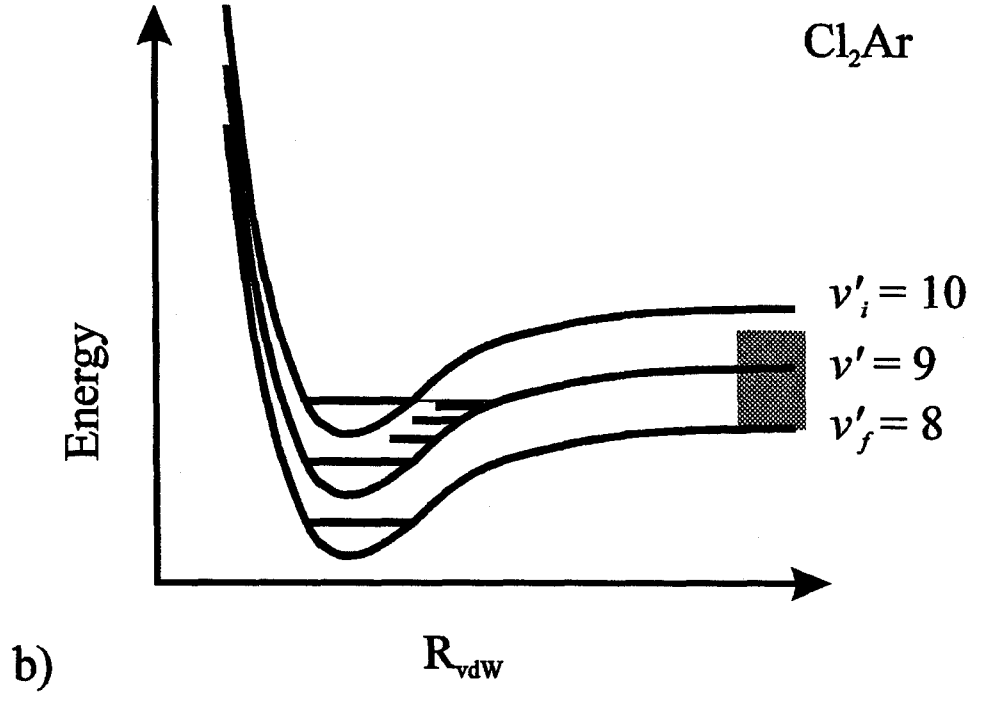
Cl2Ar
Energy
v'i = 10
v' = 9
v'f = 8
b)
RvdW

Figure 6

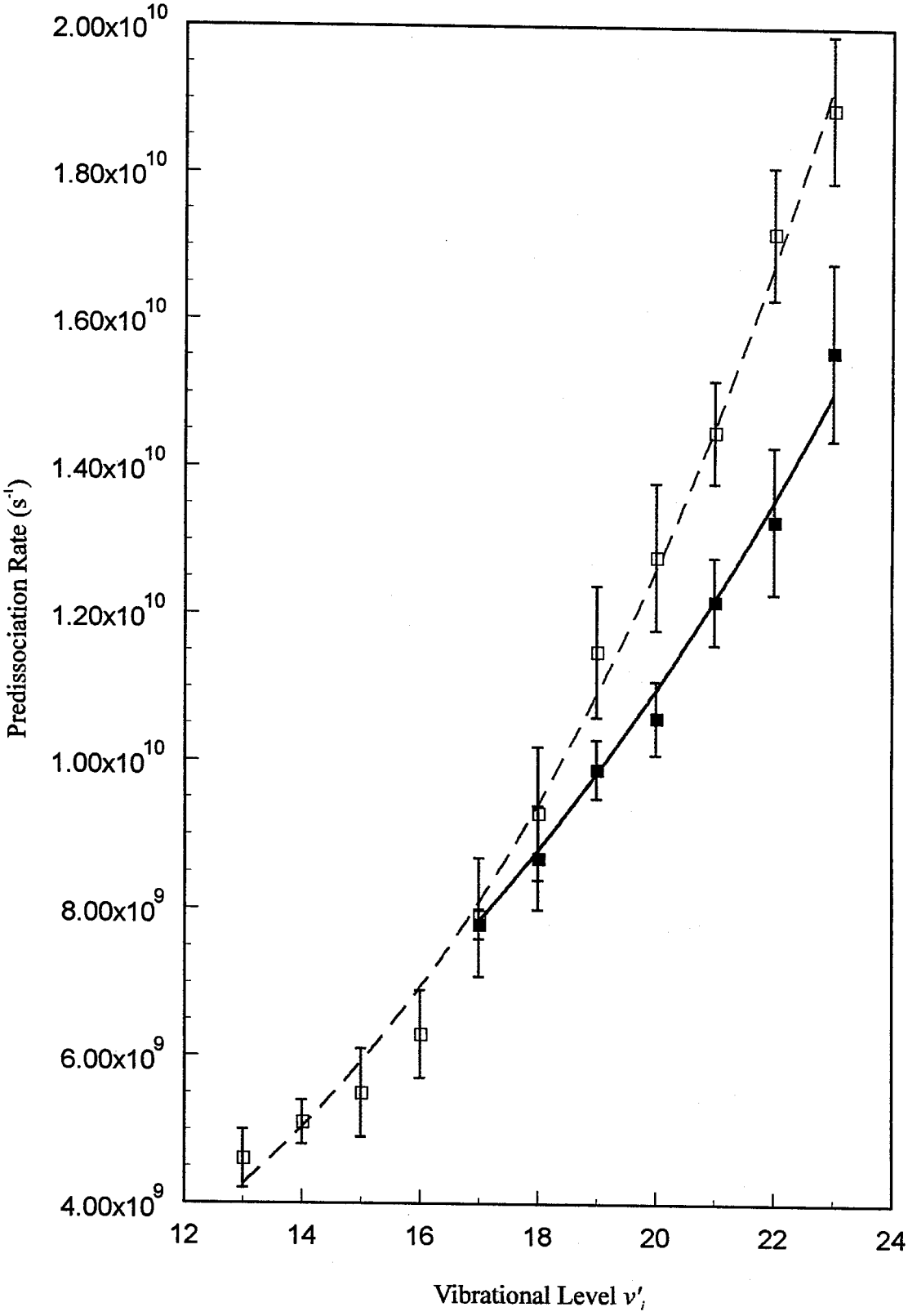
2.00x10^10
1.80x10^10
1.60x10^10
1.40x10^10
1.20x10^10
1.00x10^10
8.00x10^9
6.00x10^9
4.00x10^9
Predissociation Rate (s^-1)
12
14
16
18
20
22
24
Vibrational Level v'_i

Figure 7

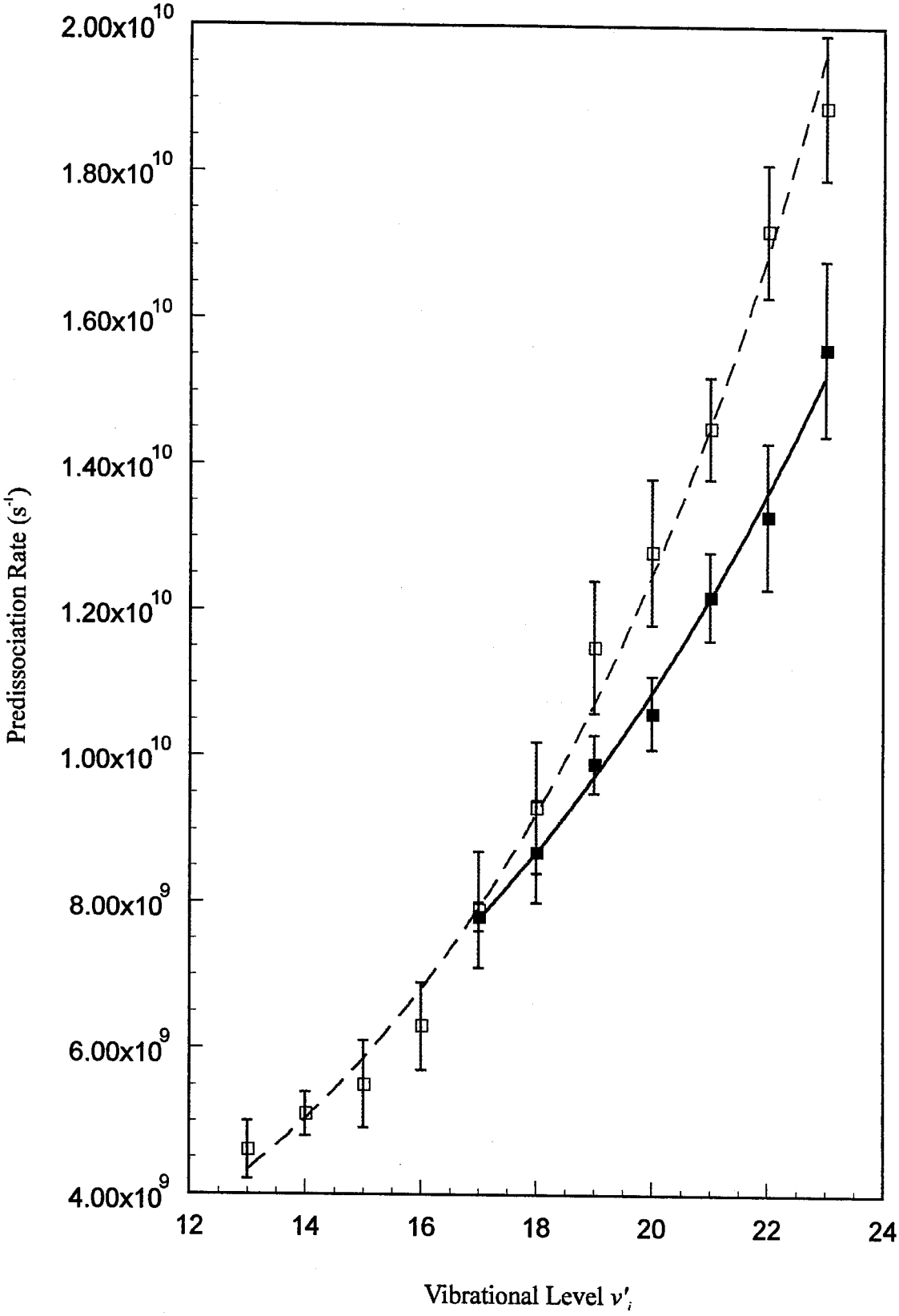
2.00x10^10
1.80x10^10
1.60x10^10
1.40x10^10
1.20x10^10
1.00x10^10
8.00x10^9
6.00x10^9
4.00x10^9
Predissociation Rate (s^-1)
12
14
16
18
20
22
24
Vibrational Level v'_i

Figure 8

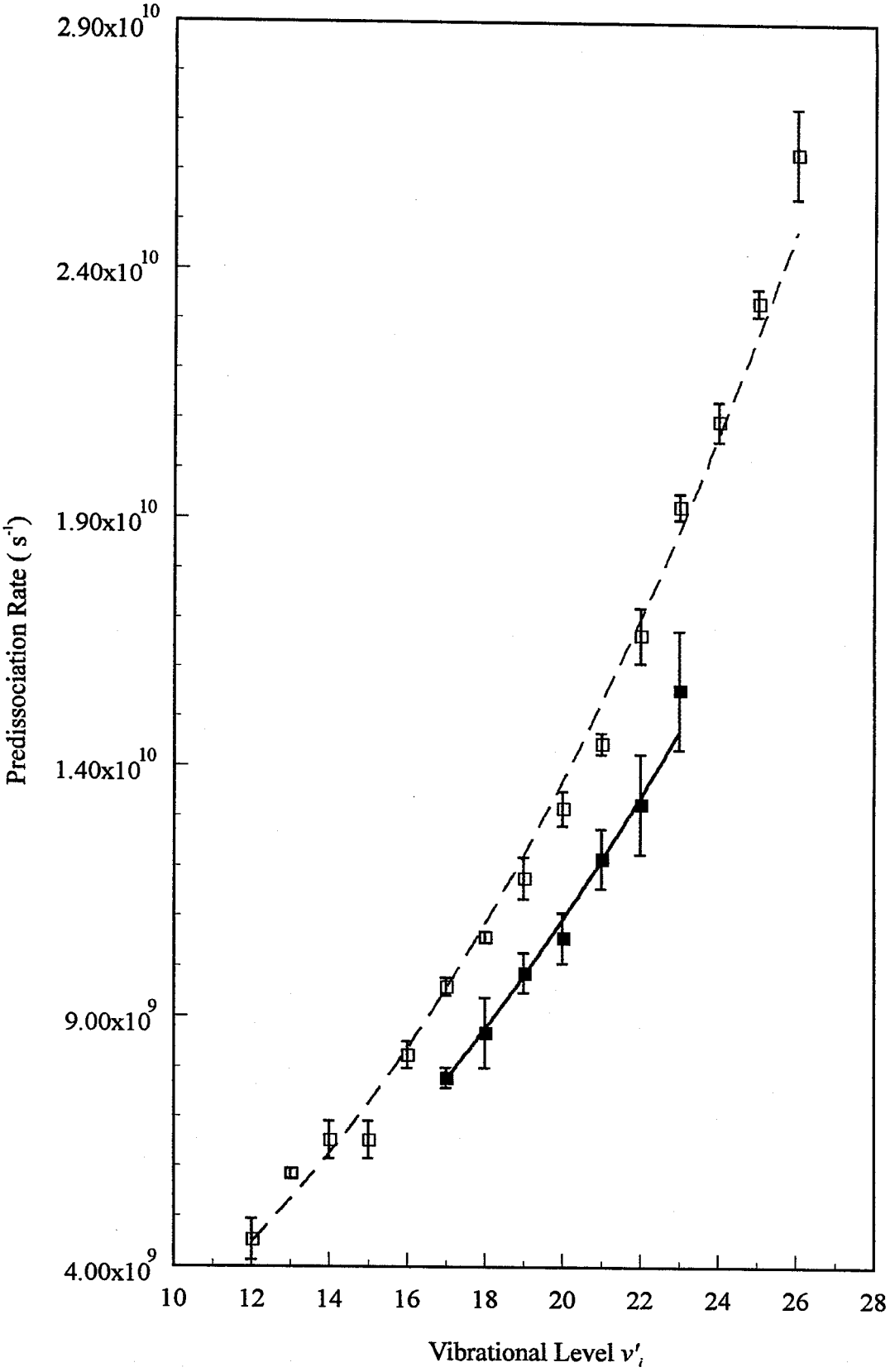
2.90x10^10
2.40x10^10
1.90x10^10
1.40x10^10
9.00x10^9
4.00x10^9
Predissociation Rate (s^-1)
10
12
14
16
18
20
22
24
26
28
Vibrational Level v'_i

Figure 9

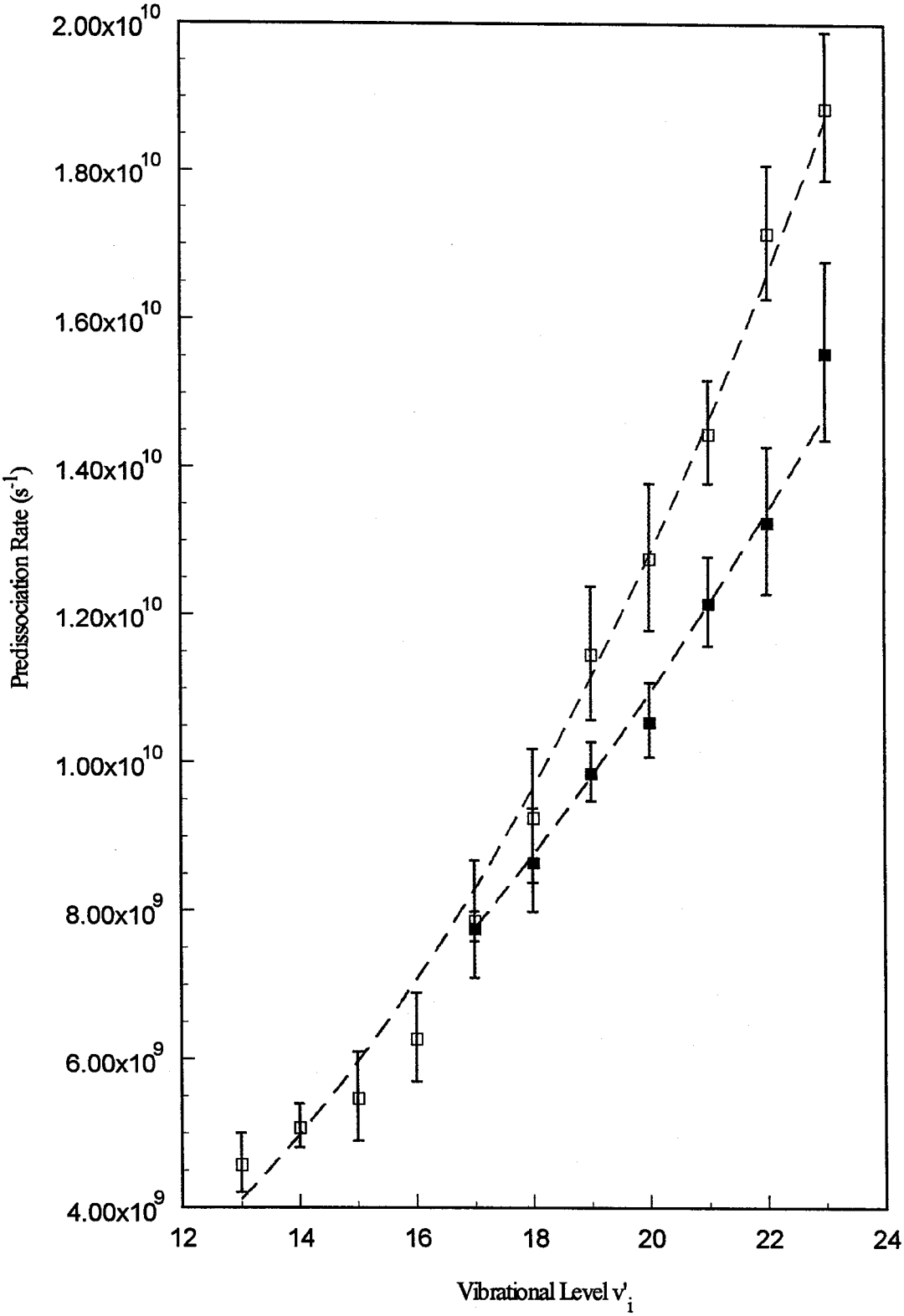
2.00x10^10
1.80x10^10
1.60x10^10
1.40x10^10
1.20x10^10
1.00x10^10
8.00x10^9
6.00x10^9
4.00x10^9
Predissociation Rate (s^-1)
12
14
16
18
20
22
24
Vibrational Level v'_i

Figure 10

Chapter V

Real-Time Dynamics of Clusters III. I_2Ne_n (n = 2 - 4), Picosecond Fragmentation and Evaporation

5.1 Introduction

The reaction dynamics of size-selected van der Waals (vdW) clusters form a basis for understanding the interplay between intramolecular vibrational-energy redistribution (IVR), and the direct fragmentation by vibrational predissociation (VP). For the case at hand, halogen-rare gas clusters, there are two interesting regimes for the dynamics which are determined by the effective size of the cluster. For small clusters, the "small-molecule" description of the dynamics may apply as in the case of I_2He, Ne, and Ar (n = 1), discussed in chapters (III)[1] and (IV).[2] In this case the dynamics of VP are governed only by the coupling between the initially prepared metastable bound state and the final dissociation continuum.

For the larger clusters, the density-of-states plays an important role in the dynamics, reaching, perhaps, the statistical limit of the "large molecule." The initially prepared state in this case couples not only to the mode(s) of the reactive coordinate(s), but also to non-reactive "bath modes" whose number increases with n. The transition from one regime to the other is interesting to explore, both theoretically and experimentally.

There are two inclusive mechanisms by which a large cluster (n>1) can undergo fragmentation. The first is by direct fragmentation, where the cluster ejects rare gas atoms in discrete, sequential, steps. The second mechanism is by indirect fragmentation, where the cluster undergoes energy redistribution first, followed by ejection of the rare gas atoms. Consider for example I_2Ne_2. The two possibilities for direct fragmentation by VP are:

$$I_2^*Ne_2(v_i') \longrightarrow I_2^*(v_i' - 2) + 2Ne \qquad (1)$$

or,

$$I_2^*Ne_2(v_i') \longrightarrow I_2^*Ne(v_i' - 1) + Ne \qquad (2a)$$

$$I_2^*Ne\,(v_i' - 1) \longrightarrow I_2^*(v_i' - 2) + Ne, \qquad (2b)$$

where v'_i is the vibrational quantum number of the initial iodine stretch. These direct pathways in equations (1) and (2) contrast a path in which energy is dissipated to the modes of the surrounding atoms/I_2 cluster. Because of the presence of the two neons, energy redistribution from the I_2 stretch to nonreactive modes could compete with direct VP, leading to a new channel:

$$I_2^*Ne_2(v_i') \longrightarrow I_2^*Ne_2^{\diamond}(v_i' - 1). \qquad (3)$$

The thermally excited cluster (denoted by $\diamond$) may then loose the Ne atoms by VP or by evaporation, this is the mechanism of indirect fragmentation.

Frequency domain studies of electronically excited dihalogen rare gas clusters have been carried out on the systems I_2He_n,[3] I_2Ne_n,[4] Br_2Ne_n,[5] Cl_2Ne_n,[6] and $IClNe_n$,[7] where $n>1$. In order to resolve the dynamics in real-time and separate the different channels, the state-to-state rates of VP and vibrational relaxation must be measured. As shown in (III) and (IV), linewidth measurements can only give an upper limit of the rate for the first step of the dynamics. A goal which can in principle be reached by the time-resolved studies is to determine the rates of the individual steps by probing the reaction intermediates directly.

This chapter focuses on studies in real-time of the state-to-state rates in I_2Ne_n (n = 2,3,4). To probe the dynamics, we use the following pump-probe/molecular beam methodology.[8] A picosecond pump pulse prepares the cluster under consideration in a well-defined vibrational state v'_i of the I_2 stretch mode (in the electronic B-state). The decay of this metastable state into the final dissociation continuum,

$$I_2^*Ne_n(v_i') \longrightarrow I_2^*(v'_f = v_i' - m) + n\,Ne \qquad (4)$$

is followed by monitoring the I_2 final state, using a time delayed picosecond probe pulse in resonance with the final quantum state. This way the absolute rates are measured for the different channels [denoted by m in equation (4)] of each cluster, and also their dependence on the initial quantum number of the I_2 stretch vibration. For I_2Ne_2, we discuss detailed results of the $m = 3$ channel for the selected states v'_i, and we propose a mechanism for the reaction. For clusters with larger n we identify the effective rate for energy dissipation which critically depends on n and v'_i.

Lineberger's group[9] has elegantly demonstrated the dependence of the dynamics in the $I_2^-(CO_2)_n$ system on the cluster size using these pump-probe methods. There are also theoretical models by Amar and Weerasinghe[10] which elucidate the mechanism of the fragmentation processes for different n. The size selection in these experiments were made using mass resolution since the system under consideration, I_2^-, has a net charge. For neutral clusters, the selection is made using the particular spectroscopic transitions of each cluster, as we discuss here (see also Reference 9).

From the pioneering work of Levy and coworkers[4] on I_2Ne_n (n = 1-7) one knows quite accurately the spectroscopic shifts. Furthermore, for n>1 the product state distribution of nascent I_2 is characterized by different vibrational states, v'_f. As one quantum of the I_2 stretch vibration corresponds to ~125 cm^{-1} and the vdW binding energy in I_2Ne is ~ 66 cm^{-1} (D_0),[11] the first observed channel for nascent I_2 from I_2Ne_2 is $m = 2$. The $m = 3$ channel is of comparable efficiency for v'_i around 20 (Reference 4). In I_2Ne_3 the most efficient channel is not, as would be expected by energetic reasoning, the $m = 3$ channel (which was still observed), but the higher $m = 4$ channel. Even $m = 5$ was observed. The larger n becomes, the more preferrable are the higher channels with m>n. From this behavior it was concluded* that VP becomes less efficient as the cluster size increases.

This chapter is organized as follows: In Section 5.2 a very brief description of the experimental methodology is presented; for more details see Chapters(III) and (IV). In Section 5.3 an account of the results is presented, and are disscussed in relation to the mechanism of fragmentation and evaporation. Comparisons with recent theoretical calculations are also discussed. This chapter is concluded in Section 5.4.

5.2 Experimental

5.2.1 Apparatus

The picosecond laser system and the molecular beam apparatus, used in these experiments, were described previously. Here, the experiments were performed by selectively exciting the cluster under consideration from the ground state $X(v'' = 0)$ to the desired $B(v'_i)$ state by tuning the pump laser pulse. Similarily, the probe was tuned to the transition of interest and laser-induced fluorescence was detected as a function of the delay between the pump and probe pulses. The pump pulse energy was ~ 5 μJ and that of the probe pulse, after frequency doubling, was ~ 0.2 μJ. Both pulses had approximately Gaussian profiles with a bandwidth (FWHM) of ca. 3 cm^{-1}. The cross-correlation measured between both laser pulses (the probe pulse was not frequency doubled) were fitted to a Gaussian with a width (FWHM) of 40 ± 3 ps over the entire frequency range used in these studies.

Selective excitation of a given cluster was possible because of the relatively large spectral shift between the $B(v'_i) \leftarrow X(v'' = 0)$ transition of I_2Ne_n and that of I_2Ne_{n-1}. The shift is larger than the band width of our laser pulses; for $n < 7$, the shift, for I_2Ne_n, is approximately $n \times 6.5$ cm^{-1} ($v'_i = 20$).[4,12]

The I_2Ne_n clusters were formed by seeding a free jet expansion of Ne (99.996% purity, Spectra Gases) with iodine (99.999% purity, Aldrich). The backing pressure was typically about 75 psig and X/D was ~ 75 (X is the distance downstream from the nozzle,

and D is the nozzle diameter). For the pulsed solenoid valve used here, the D = 150 μm and the repetition rate was 100 Hz.

5.2.2 Data Analysis

In order to obtain the rates of the different steps involved, care had to be taken in fitting the data to a single or double exponential rise The fitting routine we used[13] was based on a nonlinear least squares fit, Marquardt algorithm.[14] The fitting parameters contained the inverse rate constant(s), the zero of time (T_0), the baseline height, and the fwhm of the cross correlation (Δ). Depending on the individual transients we also took into account the possible existence of long time signal sloping at the asymptote. Δ was fixed at the measured value and the other parameters were obtained from the fits. As these observed slopes (due to slight misalignment of the pump and probe overlap over very long distances, *i.e.*,, very long times) varied randomly within groups of scans of the same v'_i, they were not believed to reveal any additional dynamical features.

For I_2Ne_2 the fits to single exponential rise functions led to consistent rates within each group of scans, but as shown in Figure 1 the results fitted the actual transients poorly (see discussion in Section 5.3). Forcing the fits to single exponentials showed only little changes with parameters. For example, varying Δ from 27 ps to 53 ps, the inverse rate constant τ was fitted between 98 ps and 104 ps and T_0 shifted within 2.5 ps for the transient shown in Figure 1A. However, the residuals show systematic deviations of the transient from a single exponential behavior; T_0 is shifted to rather high values relative to the origin of the experimental transient (more than 25 ps) and the single exponential rate values lack a physically sound interpretation (see Section 5.3).

Fits to double exponential rise functions, however, reproduced the measured transients well. The double exponential fits, which showed good signal to noise ratios and essentially no pronounced slopes at long times, yielded two different rate constants whose values could be interpreted in line with what is known about the I_2Ne (n = 1) results and

the theoretical predictions. If the transients exhibit poor signal-to-noise ratios and/or considerable slopes, the deduced rates approached each other in value. As expected, the uniqueness of the fits was eroded. There are four reasons which support the exclusion of fits exhibiting nearly identical rate values for a two-step reaction:

(i) the statistical correlation between both inverse rate constants was very high compared to those fits that showed different inverse rate constants,

(ii) the calculated deviations of the fitted inverse rate constants were very large (>100%) compared to those fits with different rates,

(iii) the fitted VP time for the second step deviates strongly from the corresponding VP time measured for I_2Ne and reported in Chapter III (see discussion in Section 5.3),

(iv) theoretical calculations predict that the first step of the consecutive bond breakage is much faster than the second one (see discussion in Section 5.3).

In order to show that the double exponential fits are robust with respect to changes in the fixed parameters (*i.e.*, Δ), two transients were chosen and Δ was fixed at various arbitrary values between 27 ps and 53 ps (note that the experimentally measured cross-correlation gives $\Delta = 40$ ps). A double exponential fit to the transient shown in Figure 1B ($v'_i = 21$) using $\Delta = 40$ ps gave the two inverse rate constants $\tau_1 = 42$ ps and $\tau_2 = 80$ ps. Varying Δ led to changes in T_0 between -3 ps and +4 ps, *i.e.*, only about 10% of Δ. τ_1 was between 33 ps ($\Delta = 53$ ps) and 49 ps ($\Delta = 27$ ps), a quite acceptable range, particularly when considering that τ_1 is close to the width of the cross correlation. τ_2 was between 75 ps ($\Delta = 27$ ps) and 84 ps ($\Delta = 53$ ps), well within the experimental error bar and within 10% of the above 80 ps value. As can be seen from Figure 1B, this transient shows an upward slope, so fixing the slope parameter to a value of zero should give an unreasonable fit. This is indeed the case, as doing so leads to $\tau_1 = 15$ ps and $\tau_2 = 115$ ps.

In order to check for any effects of the slope parameter on the fitted inverse rates, we performed another check on a transient which displayed no obvious slope. This

transient belonged to the $v'_i = 17$ group. Inclusion of the slope parameter and setting Δ = 40 ps led to values of $\tau_1 = 82$ ps and $\tau_2 = 155$ ps. Varying Δ as above and retaining the slope parameter led to T_0 changes between -2 ps and +3 ps, τ_1 between 75 ps ($\Delta = 53$ ps) and 86 ps ($\Delta = 27$ ps), and τ_2 between 160 ps ($\Delta = 27$ ps) and 165 ps ($\Delta = 53$ ps). The same procedure, setting the slope parameter to zero, gave the following results: With Δ = 40 ps, T_0 shifted +1 ps and the inverse rate constants were $\tau_1 = 77$ ps and $\tau_2 = 162$ ps. Varying D led to T_0 shifts between -1 ps and +3 ps, τ_1 between 72 ps ($\Delta = 53$ ps) and 80 ps ($\Delta = 27$ ps), and τ_2 between 160 ps ($\Delta = 27$ ps) and 165 ps ($\Delta = 53$ ps). All these values are well within our experimental error bars and demonstrate the reliability of the accepted double exponential fits.

For the larger clusters ($n = 3$ and $n = 4$) all transients were fit to an effective single exponential rise function as discussed in Section 5.3. Even though these results did not fit the actual transients well (the higher n the larger the discrepancy of the simulation), they consistently provided an effective rate, and showed a late onset of the rise in contrast to the experimental transients (on the order of 30 ps). The fitted inverse rate constants were consistent and stable against variations in Δ as discussed above.

5.3 Results and Discussion

Figure 2 shows some of the transients obtained for the I_2Ne_n (n = 1,2,3,4) clusters. Transients are presented for: Figure 2A, I_2Ne (v'_i = 17,19,21);[1] Figure 2B, I_2Ne_2 (v'_i = 17,19,21; m = 2 channel); Figure 2C, I_2Ne_3 (v'_i = 19,21,23; m = 4 channel); and Figure 2D, I_2Ne_4 (v'_i = 22, m = 5 channel). By visual inspection of these transients it can be seen that the temporal behavior within the same cluster size changes significantly with v'_i. The observed rate increases as v'_i increases for all clusters studied. Furthermore, it can also be seen that the effective rates (vida infra) decrease with increasing cluster size for each vibrational level v'_i studied. The latter observation would appear to be in contrast

with the lifetime deduced from linewidth measurements;[4] the authors reported a shortening of the lifetime when going from I_2Ne to I_2Ne_2 (cp. Table 4 in Reference 4).

The above mentioned contradiction, however, is easily resolved (vide infra) when one considers the fact that rates deduced from linewidth measurements, if homogeneous, only reflect the first step of a complicated multi-step process, e.g., the fast component in a biexponential process. Such complications in large clusters have been discussed by Levy and coworkers.[4]

The following conclusions can be drawn from the time-resolved studies:

1.The overall rates (not only the first step) depend strongly on v'_i.

2.The overall rates slow down with increasing cluster size in I_2Ne_n.

3.The dynamics in larger clusters involve a multi-step process which cannot be resolved by linewidth measurements.

In what follows the process of direct fragmentation will be considered, particularily focusing on the I_2Ne_2 system. Following this, larger clusters will be considered, to address the issue of direct fragmentation and energy redistribution as n increases.

5.3.1 Direct Fragmentation, Redistribution, and Evaporation

Sequential bond breaking in a cluster can be first considered by assuming a local mode description of the reaction coordinate. With this model, Kellman derived propensity rules of VP in I_2Ne_2 clusters.[15] If bond breaking occurs mainly sequentially, the VP process is described within the framework of this model simply by neglecting inter-mode coupling. Kellman separated the Hamiltonian as follows:

$$H = H_0 + V + V_{mc}, \tag{5}$$

where

$$V = \sum_{i=1}^{n} V(r, R_i). \qquad (6)$$

Here, H_0 is the zero-order local mode hamiltonian. V_{mc} gives the correction to the local mode approximation, *i.e.*, the correlation effects due to mode coupling. The coupling (V) is between the I_2 stretch mode, along the intramolecular coordinate r, and the vdW stretch modes, along the intermolecular reaction coordinates R_i.

The zero-order eigenfunctions of H_0 are the bound states $|v', l'_{i1}(1), l'_{i2}(2), \ldots, l'_{in}(n)\rangle$, where v' denotes the quantum number of the I_2 stretch mode and $l'_{ik}(k)$ represents the local vdW vibrational state i with respect to the k^{th} Ne atom (it essentially denotes the vdW stretch mode, possibly including bending modes). If correlation is included (e.g., by applying perturbation techniques) the corresponding wave function, according to its leading term, is written as[15] $|\Psi[v', l'_{i1}(1), \ldots, l'_{in}(n)]\rangle$.

For a sequential process, a change of one quantum of the I_2 stretch mode at a time will be considered. For the first step, one such quantum has sufficient energy to dissociate one Ne atom, assuming that the binding energy of n Ne atoms (n<7, see Reference 4) is n times as large as that of one Ne atom. In the local mode picture the metastable bound state $|\Psi[v', l'_{i1}(1), \ldots, l'_{in}(n)]\rangle$ can couple to n zero-order continua:

$$|\Psi[v'-1, \varepsilon'(1), l'_{j2}(2), \ldots, l'_{jn}(n)]\rangle,$$

$$|\Psi[v'-1, l'_{k1}(1), \varepsilon'(2), l'_{k3}(3), \ldots, l'_{kn}(n)]\rangle, \ldots,$$

$$|\Psi[v'-1, l'_{m1}(1), \ldots, l'_{mn-1}(n-1), \varepsilon'(n)]\rangle,$$

where ε' denotes the kinetic energy of the recoiling fragments, *i.e.*, I_2Ne_{n-1} + Ne.

There is also the possibility of non-reactive energy redistribution to the cluster modes which results in heating. The redistribution can lead to VP or to evaporation of the Ne atoms, (probably) by a statistical energy channeling to the reaction coordinate. In order to avoid dissociation, the energy has to be shared by the different cluster modes, below the dissociation energy. As the coupling operator is assumed to be a one particle

operator, correlated bound wave functions have to be considered to allow for excitation of more than one local mode. The coupling for non-reactive energy redistribution is then between the initial metastable state and bound levels. In a golden rule description, the rate for non-reactive energy redistribution from I_2 to the cluster modes in I_2Ne_n can be written as:

$$k^r\left(n\middle|v_i',\{l'\}\right) \propto \left|\left\langle \Psi\left[v_i',l'_{i1}(1),\ldots,l'_{in}(n)\right]\middle|V\middle|\Psi\left[v'_j,l'_{k1}(1),\ldots,l'_{kn}(n)\right]\right\rangle\right|^2 \rho, \tag{7}$$

where ρ is the relevant density of states.[16] v'_i (v'_j) denotes the initially excited (final) I_2 stretch level and $\{l'\}$ describes all vdW vibrations involved. In writing equation (7) we have assumed that IVR is not restricted,[17] *i.e.*, dissipative, and that coherence effects are absent. This has been shown not to be the case even for large molecules,[18] but perhaps is justified here, if we assume that the low-energy modes of the clusters form a quasicontinuum. This "kinetic limit description" of IVR has been discussed elsewhere.[19]

The rate for the direct one-quantum VP, $I_2Ne_n \rightarrow I_2Ne_{n-1}$, from the v'_i state can now be expressed as follows:[20]

$$\begin{aligned} k^{VP}\left(n,n-1\middle|v_i',\{l'\}\right) &\propto \left|\left\langle \Psi\left[v_i',l'_{i1}(1),\ldots,l'_{in}(n)\right]\middle|V\middle|\Psi\left[v_i'-1,\varepsilon'(1),l'_{k2}(2),\ldots,l'_{kn}(n)\right]\right\rangle\right|^2 +\ldots \\ &+\left|\left\langle \Psi\left[v_i',l'_{i1}(1),\ldots,l'_{in}(n)\right]\middle|V\middle|\Psi\left[v_i'-1,l'_{m1}(1),\ldots,l'_{mn-1}(n-1),\varepsilon'(n)\right]\right\rangle\right|^2. \end{aligned} \tag{8}$$

Assuming that correlation effects are negligible (*i.e.*, a pure local mode picture), equation (8) reduces to:

$$k^{VP}\left(n,n-1\left|v_i',\{l'\}\right.\right) \propto \left|\left\langle \Psi[v_i', l'_{i1}(1)] \middle| V(r,R_1) \middle| \Psi[v_i'-1, \varepsilon'(1)] \right\rangle\right|^2 + \ldots + \left|\left\langle \Psi[v_i', l'_{in}(n)] \middle| V(r,R_n) \middle| \Psi[v_i'-1, \varepsilon'(n)] \right\rangle\right|^2 . \quad (9)$$

If the initial state is prepared such that all vdW vibrations are identical [*e.g.*, in the ground vibrational state $l'_{ik}(k) = 0$], equation (9) can be simplified to give:

$$k^{VP}\left(n,n-1\left|v_i',l_1'\right.\right) = nk^{VP}\left(1,0\left|v_i',l_1'\right.\right) \propto n\left|\left\langle v_i', l'_1(1) \middle| V(r,R_1) \middle| v_i'-1, \varepsilon'(1) \right\rangle\right|^2 . \quad (10)$$

As reported in (III), $k^{VP}\left(1,0\left|v_i',l_1'\right.\right)$ refers to the rate constant of VP in I_2Ne. If the nonreactive channel competes with VP, the first step of the reaction involves a total rate given by:

$$K\left(n\left|v_i',\{l'\}\right.\right) = k^{VP}\left(n,n-1\left|v_i',\{l'\}\right.\right) + k^{r}\left(n\left|v_i',\{l'\}\right.\right). \quad (11)$$

Although some approximations have been invoked in obtaining equation (10), it leads to a single concept concerning the first step of VP: If no nonreactive energy redistribution is present, the VP time for the first step will roughly scale as $1/n$ that of the corresponding VP process in I_2Ne. Thus, by comparing the rate of the first step of VP in I_2Ne_n with n times that of the corresponding VP rate in I_2Ne one should obtain an estimate of the importance of the nonreactive channel. In the quasiclassical trajectory calculations of Delgado-Barrio and coworkers,[21] discussed below, the difference between K and k^{VP} is attributed to IVR, the energy redistribution that describes k^r. It should be noted that in nonreactive energy dissipation, it is possible to have energy redistribution maintaining the total energy of the I_2X_n systems constant (IVR) or lowering the I_2 energy

with the solvent acquiring kinetic energy [vibrational relaxation (VR) in this case equivalent to VP].

The above discussion considered direct coupling to the reaction coordinates (or to modes that possess a component along the reaction coordinates), and coupling to modes that are not the reaction coordinates or elements of the dissociative continuum. The latter energy redistribution is IVR, and if IVR is involved, the energy transferred to these nonreactive modes can still be channelled into the reaction coordinates and we have IVR possibly preceding "statistical evaporation." Also, IVR can preceed another VP fragmentation as discussed by Semmes et al.[22] Finally, we notice that in equation (8), if all n atoms are fragmented by VP simultaneously, the I_2 vibrational energy must be changed by n quanta at once, a highly improbable process, certainly for harmonic and even anharmonic systems. That is why in these VP systems, unlike chemical bond breakage,[23] the propensity is more toward a sequential mechanism.

In order to obtain the dynamics of VP for the first step let us now consider the first member of this cluster family, I_2Ne_2.

5.3.2 The I_2Ne_2 Cluster

In this case, the scheme for direct VP and energy dissipation can be written as:

$$\begin{array}{l} I_2^* Ne_2(v_i') \xrightarrow{k_1^{VP}} I_2^* Ne(v_i' - 1) \xrightarrow[(m = 2 \text{ channel})]{k_2^{VP}} I_2^*(v_i' - 2), \\ \downarrow k^r \end{array} \tag{12a}$$

$$\begin{array}{l} I_2^* Ne_2^{\#}(v_i' - 1) \xrightarrow{k_1^{VP}} I_2^* Ne\ (v_i' - 2) \xrightarrow[(m = 3 \text{ channel})]{k_2^{VP}} I_2^*(v_i' - 3), \\ \downarrow \langle k \rangle \\ \text{Evaporation.} \end{array} \tag{12b}$$

Here the redistribution leads to a hot cluster, and IVR precedes VP for the $m = 3$ channel. The number of m-channels in this scheme should be sufficient as the yield of higher channels is negligible.[4] Note that the fact that we detect I_2 in $m = 3$ for I_2Ne_2 indicates that direct VP [equation (12a)], which involves the expected two quanta change for two neon atoms, must not be the only channel. k^r is significant as discussed below.

According to equation (12a), the transient buildup of I_2 from I_2Ne_2 should exhibit a biexponential behavior, and for the $m = 2$ channel this build-up is simply given by:

$$Signal(t) \propto \left\{1 - \frac{1}{k_2^{VP} - K_1}\left[k_2^{VP} \exp(-K_1 t) - K_1 \exp(-k_2^{VP} t)\right]\right\}, \qquad (13)$$

where $K_1 = k_1^{VP} + k^r$. If the simple relation in equation (10) holds with $k^r = 0$, then $K_1 = k_1^{VP} = 2k_0^{VP}(1)$, where $k_0^{VP}(1)$ refers to the corresponding VP time of I_2Ne reported in (III). To obtain the rate constants of both steps it is important to achieve experimental data with a high signal-to-noise ratio (see Section 5.2).

Figure 1 shows a representative transient ($v'_i = 21$) for the $m = 2$ channel of I_2Ne_2, fitted to a single exponential rise (A) and to a double exponential rise (B). As discussed in Section 5.2, a comparison of these fits shows that a one-step mechanism (single exponential) is not appropriate for describing the dynamics of VP in this system. The single exponential fit in Figure 1A gives $\tau = 101$ ps. The double exponential fit is in better accord with the experimental transient and gives $\tau_1 = 42$ ps and $\tau_2 = 80$ ps. Similar comparisons for all our experimental transients ($v'_i = 17$-21), which exhibit good signal-to-noise ratios, confirm this observation; the results are shown in Table 1. The fits for $v'_i > 21$ did not prove to be very reliable due to the fact that the time constant of the first step is considerably shorter than the measured cross-correlation width (see section 5.2). It is concluded that the mechanism of VP in I_2Ne_2 involves at least a two-step process and sequential bond breaking is dominant.

In Table 1 the results for various v'_i values are shown and in Table 2 these values are compared with the predictions of the model. The expected rate constant for the first step is $2k_0^{VP}(1)$ (for $v'_f = v'_i\text{-}1$) and for the second step it is $k_0^{VP}(1)$ (for $v'_f = v'_i\text{-}2$). The tabulated rate constants of $2k_0^{VP}(1)$ (for $v'_f = v'_i\text{-}1$) and $k_0^{VP}(1)$ (for $v'_f = v'_i\text{-}2$) are derived according to the sequential bond breaking mechanism [equation (10) for step 1, and VP of I_2Ne from v'_i-1 as step 2] using the values reported in (III) for I_2Ne (n = 1).

From Table 2 it can be seen that the simple considerations leading to equation (10) appear to be in line with these results; however, for v'_i = 18 a slight and for v'_i = 17 a significant slow-down of the first step is observed. The fitted rate constants of the second step agree fairly well with the rates we measured for I_2Ne. (It should be noted that in comparing the time constants of the second step with the values reported in (I), v'_i has to be stepped down by one as predicted from the above analysis). A comparison of these findings is shown in Figure 3. The agreement especially for the lower v'_i is rather good.

There is a problem, however. Considering scheme (12), the product ratio can easily be calculated applying simple kinetics. The time-dependent build-up of the population of $I_2(v'\text{-}2)$ divided by the initial population of excited $I_2Ne_2(v')$ clusters, $P(t)$, is given by:

$$P = \frac{k_1^{VP}}{K_1} - \frac{k_1^{VP} k_2^{VP}}{k_2^{VP} - K_1}\left\{\frac{\exp[-K_1 t]}{K_1} - \frac{\exp[-k_2^{VP} t]}{k_2^{VP}}\right\}. \qquad (14)$$

Letting $t \rightarrow \infty$ leads to the product state (v'_i-2) population:

$$P = \frac{k_1^{VP}}{K_1} = \frac{k_1^{VP}}{k_1^{VP} + k^r}. \qquad (15a)$$

As only two channels are considered, the sum of P and the product state (v'_i-3)population, Q, must be one, yielding

$$Q = \frac{k^r}{K_1} = \frac{k^r}{k_1^{VP} + k^r}. \tag{15b}$$

Thus, the branching ratio for the two channels is simply

$$\frac{\text{probability}\,(m=2)}{\text{probability}\,(m=3)} = \frac{k_1^{VP}}{k^r}. \tag{16}$$

The time constants we obtained for the first step (see Tables 1 and 2) would imply that the m = 3 channel is relatively unimportant. As discussed above, the first step in I_2Ne_2 is about twice as fast as the corresponding VP in I_2Ne and this means that k^r should be negligible. This finding would be in contradiction with our detection of nascent I_2 in the m = 3 channel and the results of Levy and coworkers[4] who found that the branching into the channels m = 2 and m = 3 occurs with about equal probability for v'_i = 21,22. It is not expected that this branching ratio will change by orders of magnitude when going to the other v'_i levels under study. Thus, according to equation (16), k^r and k_1^{VP} should be about equal in magnitude and k_1 should have a value about four times as large as the corresponding VP rate constant of I_2Ne [see equations (10) and (11)].

The discrepancy can be understood by considering a slight revision of the above scheme (12). The local mode picture restricts the extent of the energy flow from the I_2 stretch coordinate into the reactive vdW coordinates. What is necessary to consider is the cluster modes, which take into account the fact that the motions of these atoms are correlated. I_2Ne_2 now becomes a "large" system with 6 modes. These clusters are quite "floppy" with low-frequency large amplitude modes. In fact, Janda's group[24] described Cl_2He_2 as a liquid-like cluster, and, using the instantaneous normal mode analysis, Adams

and Stratt[25] obtained a phonon spectrum for Ar_2. Therefore, instead of the two local mode reaction coordinates, R_1, and R_2, for the two I_2-Ne distances, we consider the reactive and nonreactive coordinates with possible IVR to either of them.

For I_2Ne (n = 1) there is only one VP pathway. For I_2X in general,e.g., X = Ar, there is a possibility for IVR preceding VP, depending on the Δv energy release relative to the energy of the vdW bond. For I_2Ar, a coherent pulse can prepare a coherent superposition of states and energy can flow (IVR) first from $|v,0\rangle$, the zero-order state, which carries some oscillator strength, to $|v-1,l\rangle$ and/or $|v-2,l\rangle$, which in turn undergo VP to the $|v-3,\varepsilon\rangle$ continuum. If, on the other hand, an eigenstate is prepared, these sequential dynamics will not be observed and VP from a mixed state $\alpha|v,0\rangle+\beta|v-1,l\rangle+\gamma|v-2,l\rangle$ will be observed. Such a dynamical behavior of coherent energy redistribution has been observed in IVR experiments, even in large molecules.[17,18] (Incoherent preparation of states can lead to averaging out of these IVR resonance effects[17,26]). Janda's group[27] has shown the importance of this issue of the preparation of state in Cl_2Ar and Gray[28] has found (theoretically) such an IVR process in I_2Ar. For the I_2Ne cluster, the energetics (Δv = -1, gives < 100 cm^{-1}, $D_0 \sim$ 66 cm^{-1}) do not allow for such a mechanism, in contrast to I_2Ar or Cl_2Ar where there are bound intermediate (v-k) states [see Chapter (IV), Figures 6,7]. For I_2Ar, Δv = -1 gives < 100 cm^{-1}, $D_0 \sim$ 235 cm^{-1} (Ref. 11); for Cl_2Ar, Δv = -1 gives < 200 cm^{-1}, D_0~178 cm^{-1} (Ref. 29).

In the case of I_2Ne_2 (or larger clusters) reactive (mixed) modes are not necessarily pure local (l) modes and their energetics may allow for such a behavior. These (Q) modes are a superposition of the local modes, and some can have the required dissociation energy. We will consider IVR in these clusters to be direct, if such modes form intermediate bound or quasi-bound levels for the initial state to interact with. Thus, IVR could preceed direct VP and this is now evident in a number of cases, e.g., IVR prior to isomerization[30] and IVR prior to VP in large molecule vdW clusters.[22]

Let us now expand on this and consider I_2Ne_2. The correlated cluster modes (as opposed to local modes) with high-lying energy levels can serve as accepting modes for one quantum of the I_2 stretch from the initial state $|v,0\rangle$. Some of these cluster modes will contain the reaction coordinate(s), i.e., strongly couple to either or both of the energetically accessible translational continua (loss of one Ne atom). Other modes will not efficiently couple to the reaction coordinates and thus be able to "trap" one quantum of the I_2 stretch and possibly undergo further coupling to other cluster modes. In a very simplified picture in analogy to an ABA potential hypersurface) one may think of a reactive mode containing an antisymmetric stretch motion of the Ne atoms with respect to the center of the I_2 bond, which is connected to the continuum by "overstretching" to one side. A nonreactive mode may, for example contain the corresponding symmetric stretch motion of the two Ne atoms and be able to trap one quantum of the I_2 stretch (resonance). A (symmetric) cluster mode involving both rare gas atoms can also explain a non-vanishing probabability for multiple continua (dissociation of two Ne atoms at once in a two quantum process) and some formation of Ne_2 as calculated in Reference 21.

In this picture, the first step of the I_2Ne_2 cluster dynamics will evolve into either a reactive mode (k^{rr}) or a nonreactive mode (k^{nr}):

$$I_2Ne_2(v_i') \begin{cases} \xrightarrow{k^{rr}} I_2Ne_2(v_i'-1,r) \\ \xrightarrow{k^{nr}} I_2Ne_2(v_i'-1,nr) \end{cases} . \qquad (17)$$

(The asterisks on I_2 used before have been dropped for simplicity). This would then give the branching into the reactive (r) and nonreactive (nr) channels. If the reactive mode is excited in an energetically high lying level, dissociation into the continuum could occur extremely fast (k_{diss}) leaving I_2Ne, which subsequently could undergo "normal" VP as reported in (III) for I_2Ne. We note that the system is no longer one-dimensional in R and a highly excited and "bound" reactive mode can "see" a translational continuum, the

second dimension. Again, the situation is reminiscent of ABA systems on electronic (here, vibrational) potential hypersurfaces with a trajectory at the saddle point bound in the symmetric and unbound in the antisymmetric coordinate.

Following IVR from the v'_i state to the (v'_i-1,r) state the process can be written as:

$$I_2Ne_2(v'_i-1,r) \xrightarrow{k_{diss}} I_2Ne\ (v'_i-1) \xrightarrow{k^{VP}} I_2(v'_i-2), \quad (m=2) \qquad (18)$$

which is similar in form to equation (12), but now the branching of m = 2/m = 3 can be accounted for by IVR. Considering IVR [precursor in equation (18)], the build-up of nascent I_2 according to equation (18) is triple exponential. However, the dissociative step is expected to be extremely fast (<10 ps) and with our experimental time resolution at the moment, a double exponential build-up is predicted. k^{rr} strongly depends on v'_i due to the anharmonicity of the I_2 stretch; the energy-gap between this mode and the accepting (low frequency) cluster modes will become smaller and thus the coupling will increase with v'_i. k^{rr} is similar to k^{VP} of the first step with two differences. First, to break the I_2-Ne bond, the IVR process of k^{rr} is followed by the very fast dissociation process and the "rate determining step" is the initial v'_i to v'_i-1 process (VP). Second, the coupling is from the I_2 stretch to now a "mixed" reactive mode and k^{VP} somewhat different from $2k_0^{VP}(1)$. From Table 2 we see differences as large as 25%.

The second step in the effective double exponential of equation (18) should then reflect VP of I_2Ne (see (I) and Table 2) from $I_2Ne(v'_i-1)$ to yield $I_2(v'_i-2)$. These predictions are in good agreement with our observations (see Table 2).

A consequence of the above analysis is a prediction about the m = 3 channel. For this channel, k^{nr} is a key for involving the nonreactive modes. As the energy of one quantum of the I_2 stretch is trapped in the cluster modes, further mode coupling to other cluster modes is possible. A second quantum of the I_2 stretch can then be transferred to

the cluster modes, either into the reactive channels or the nonreactive channels. Transfer into the reactive channels would lead to the subsequent process described above. Transfer into nonreactive modes would leave the cluster "hot" and statistical dissociation (evaporation) is possible. The number of redistribution and evaporation pathways would increase with cluster size as more nonreactive modes would become available for energy storage and higher m quantum channels would become dominant as observed for larger clusters.[4]

The $m = 3$ channel in I_2Ne_2 should then show a multiple exponential behavior and be effectively slower than the $m = 2$ channel. The overall rate will depend on v'_i through k^{nr} as discussed for the reactive channel. The branching will be determined by k^{rr}/k^{nr}, and according to the above discussion both rate constants will have to be about equal. This is plausible as both describe similar processes, vibrational/rotational energy redistribution.

An example of our results for the $m = 3$ channel is displayed in Figure 4 which shows a pair of transients, both for $v'_i = 21$; the top one corresponds to the $m = 2$ channel of I_2Ne_2 whereas the bottom one is for $m = 3$. The results indicate that the kinetics for both channels are very different; the $m = 3$ channel shows a significantly slower overall rate than the $m = 2$ channel (for $m = 2$, "τ" = 103 ps ± 4 ps, while for $m = 3$, "τ" = 145 ps ± 11 ps; the transients were fitted to single exponential rise functions). So it can be concluded that the higher m quantum channels of VP in I_2Ne_n clusters are slower with respect to the lower m quantum channels consistent with the above model of reactive and nonreactive division of the cluster modes.

Calculations of the vibrational predissociation of I_2Ne_2 have been performed by two groups, Schatz, Buch, Ratner, and Gerber (SBRG)[31] and Garcia-Vela, Villarreal, and Delgado-Barrio (GVD).[21] Both groups performed their calculations for the $v'_i = 28$ level. The calculations of SBRG were restricted to I_2Ne_2 in a collinear configuration. These authors did quasiclassical trajectory (QCT) calculations as well as classical time-dependent self-consistent field (TDSCF) calculations which agreed fairly well with each other.

SBRG obtained the lifetimes from a simple two-step VP process. For each step a single exponential decay was assumed.

The QCT calculations yielded a lifetime of 5 ps for the first step and a lifetime of 13 ps for the second step. The result that the first step was calculated to be more than twice as fast as the second step (cp. the simple estimate for a two-step VP in part A above) was interpreted in terms of an acceleration of the first step, mediated by I_2 bouncing back from the second Ne atom and hitting the first Ne atom hard so it leaves the cluster faster than if no second Ne atom was present. SBRG also calculated the action losses during VP whose values divided by $\hbar$ can be related to the number of I_2 stretch quanta lost. For the first step SBRG found action losses of 2.29 $\hbar$ corresponding to nascent $I_2Ne(v'_i\text{-}2)$. For the second step they observed non-transient fragments I_2Ne losing 0.98 $\hbar$ [corresponding to the product $I_2(v'_i\text{-}3)$] which have the above quoted lifetime of 13 ps and transient fragments I_2Ne which dissociate immediately with an action loss of 0.002 $\hbar$ (corresponding to the product $I_2(v'_i\text{-}2)$). So, according to SBRG, the m = 2 channel should be almost single exponential and correspond to a double continuum process where both Ne atoms are lost more or less simultaneously.

The m = 3 channel should then show double exponential kinetics corresponding to sequential bond breakage. We also observe a slow-down of the first step with respect to the second, which, however, can easily be explained even by the simple considerations discussed in part A (the simple two step process). The first step involves twice the rate of I_2Ne prepared in v'_i and the second rate is the one for VP of I_2Ne prepared in v'_i-1. As shown in (I), VP of I_2Ne increases with increasing v'_i, thus the first step must clearly be faster than twice the second step. An impulsive picture using a collinear geometry is not necessary in order to explain these results, especially since the structure of I_2Ne_2 is most likely nonlinear as discussed in Reference 4. I_2He is known to be nonlinear.[32] As the kinetics we observe are at least double exponential, a simultaneous bond breakage as

inferred from the calculations of SBRG does not seem to play a major role for the $m = 2$ channel.

GVD,[21] on the other hand performed QCT calculations on the first VP step of I_2Ne_2 ($v'_i = 28$) in a nonlinear configuration confined to the following motions: I_2 stretch, Ne center-of-mass (I_2) stretch, van der Waals bend along a plane perpendicular to the I_2 moiety. GVD calculated a VP time of 7.36 ps for the first step which is about 1.5 times longer than the result obtained by SBRG. This lifetime is 2.85 ps larger than expected by equation (10). Thus GVD observe a slow-down. They interpret this slow-down in terms of IVR processes occurring in larger clusters due to the presence of accepting cluster modes. This interpretation is consistent with our model discussed above, however, the slow-down they observe is quite large compared to our experimental findings as we only observe a significant slow-down for $v'_i = 17,18$. GVD did not report any action losses during VP for their calculations, and therefore a distinction between the $m = 2$ and the $m = 3$ channel does not seem to have been made. Thus, the slow-down calculated could be exaggerated by the fact that both channels are somehow mixed in these calculations and the $m = 3$ channel leads to longer lifetimes. GVD also found some probability for double continuum transitions (loss of two Ne atoms at once) and formation of Ne_2 which is in line with our cluster mode discussion above.

5.3.3 The I_2Ne_n ($n = 3,4$) Clusters

In order to compare the dynamics of the various clusters I_2Ne_n an effective overall rate of VP is introduced. So far only the nascent I_2 fragment in the dominant channel has been probed, and since the number of possible pathways increase with n, the situation becomes very complicated. The simplest way of defining such an effective rate is by fitting all measured transients to single exponential rise functions which leads to an effective overall rate constant k_{eff}. Such a fit cannot, of course, describe any subtleties of the detailed kinetics but should at least provide a rate determining step to the transition

from the initially excited metastable cluster state v'_i to the product state v'_f of nascent I_2. The k_{eff} values along with the corresponding times τ_{eff} are listed in Table 3. Values which are calculated from equation (10) and then are fitted to a single exponential rise (k^c_{eff}, τ^c_{eff}) are also given. These values refer to a simple n-step sequential bond breakage and the necessary data for VP of I_2Ne are taken from (III). Figure 5 shows the experimental rate constants k_{eff} vs. v'_i for the different clusters. For I_2Ne_2 both the $m = 2$ and the $m = 3$ channels are shown. Included for comparison are the results for I_2Ne. The calculated values k^c_{eff} are also plotted in this figure.

In Table 3a the results[1] for I_2Ne are shown for comparison, in Table 3b the data for I_2Ne_2 ($m = 2$ channel) is presented. As discussed in the previous part, the calculated values and the observed ones agree well and do not show evidence for a significant slow-down of the rates except for $v'_i = 17,18$.

Table 3c shows the corresponding results for I_2Ne_2 ($m = 3$ channel). All rates measured for this channel are significantly smaller than the calculated ones. From the table, and Figure 5, it can be seen that a simple two-step mechanism is not at all appropriate in describing the $m = 3$ channel dynamics. The slow-down of the measured rates with respect to the calculated ones is evident and can be understood using the concepts discussed above. It is consistent with the idea that k^r is increasing and more channels are opened to the nonreactive modes. As with I_2Ne_2, the slow-down becomes more significant for the lower values of v'_i.

In Table 3d the results for I_2Ne_3 ($m = 4$ channel) and for I_2Ne_4 ($m = 5$ channel) are shown. The trend observed in I_2Ne_2 is continued for the higher clusters; the slow-down of the rates with respect to the calculated ones implies that IVR steps precede the actual bond breakage and overall VP becomes relatively slow (Figure 5). Increasing the cluster size provides an increasing density of bath states making IVR processes more and more efficient; the time spent for enough energy to get into the reactive vdW coordinates becomes longer. In addition higher VP channels are observed[4] the larger the cluster gets,

as more and more energy is dissipated into the internal cluster modes. Furthermore, as the number of bath states of the intermediate fragments becomes larger with increasing size of the parent cluster, additional IVR processes within these fragments lead to an efficient slow-down of the overall VP rate.

QCT calculations for the higher clusters I_2Ne_n (n up to 9) have also been performed for the first step of VP ($v'_i = 28$) by GVD.[21] Comparing to the simple n-step process [cp. equation (10)], the authors found decreasing rates with increasing cluster size which they interpreted in terms of increasing IVR due to the increasing number of storage modes. These results are in line with our observations for the overall rates of the higher clusters. It should be mentioned, however, that GVD did not distinguish between the different channels of VP; so their lifetime results should be viewed as channel-averaged.

Since IVR increases with n, the larger clusters may be described by a statistical $k(E)$ for the evaporation of Ne atoms. One can use standard RRKM theory, phase space theory (PST) or the Engelking model[33] to obtain $k(E)$. The problem, however, is that even in the simplest RRK expression

$$k^n(E) = \nu \left[\frac{E - E_0^n}{E} \right]^{s_n - 1}, \qquad (19)$$

one needs to know the effective number of modes s_n for the different clusters. The energy threshold E_0^n, and the frequency factor are easier to obtain. The transition state should be close to the product (exit channel), and PST may be more adequate. It is interesting to note that for $n = 1$ [υ taken to be the vdW stretch frequency[11] corresponding to 25 cm^{-1}, $E_0 = D_0 = 66$ cm^{-1}, $E = 91$ cm^{-1} ($v'_i = 20$, $\Delta v = -1$)], we obtain $k(E) = (18\ ps)^{-1}$ when the I_2 stretch is included ($s_n = 3$), and $k(E) = (5\ ps)^{-1}$ when the I_2 stretch is excluded ($s_n = 3$).

For any serious estimate of $k(E)$, the density of states[34] must be considered carefully in such floppy systems. Amar has adressed these points in his calculations of evaporation rates in $Br_2^-(CO_2)_n$.[10] The neutral cluster I_2Ne_n is an ideal system to calculate $k(E)$ and this is currently under investigation. Since the rates are measured and the rare gas/I_2 potential parameters have been deduced, the neutral clusters I_2Ne_n should be ideal systems to compare theory with experiments in hope of quantifying the nature of the modes involved in IVR, VP, and evaporation.

5.4 Conclusions

In this chapter real-time studies are presented on the picosecond fragmentation and evaporation of I_2Ne_n (n = 2-4) clusters. The pathways for direct vibrational predissociation (VP), and for the onset of energy redistribution with increasing cluster size have been examined. The elementary VP process and its dependence on the stretch quantum number of $I_2(v'_i)$ has been observed. The process can be understood as a direct coupling, employing the repulsive force between I_2 and Ne, from the I_2 stretch (in v'_i) to the continuum of states of (v'_i-1).

As the cluster size increases, we observe the onset of IVR, and the rate of VP decreases with n. IVR accesses reactive and nonreactive modes and this leads to direct fragmentation or statistical-type evaporation, respectively. Similar to previous IVR studies in real-time, the question of the preparation of state becomes important in establishing IVR as a precursor to VP. The evidence comes from careful examination of I_2Ne_2 steps whose transient results show a double exponential build-up of nascent iodine. With this simple model we can understand the rates, their dependence on v'_i and product state distributions.

As n increases further, the situation is more complex, and an effective rate constant is introduced, which is inclusive of all of the fragmentation steps. This rate constant has been experimentally shown to decrease as n increases, and as v'_i decreases. Although IVR

increases with n (and this leads to more channels "m" in nascent iodine with $m>n$, the statistical "average" rate decreases as energy takes more time to find the reaction coordinate (larger effective density of states).

These halogen-rare gas systems are quite interesting and there remain a number of theoretical and experimental problems to be addressed. Experiments on a shorter time scale are in progress. Also of interest are comparisons with results for the same system, but at high rare gas densities.[34,35] Little is known about the theoretical predictions of structure and the dynamics for large n, and hopefully with the aid of experiments, theoretical studies can quantify the behavior with v'_i and n. In the reference 36, we focus on one such question, the role of direct excitation to the reaction coordinate.

5.5 References

1. D. M. Willberg, M. Gutmann, and A. H. Zewail, J. Chem. Phys. **96**, 198 (1992).

2. M. Gutmann, D. M. Willberg, and A. H. Zewail, J. Chem. Phys. **97**, 8037 (1992).

3. W. Sharfin, K. E. Johnson, L. Wharton, and D. H. Levy, J. Chem. Phys. **71**, 1292 (1980).

4. J. E. Kenny, K. E. Johnson, W. Sharfin, and D. H. Levy, J. Chem. Phys. **72**, 1109 (1980).

5. B. A. Swartz, D. E. Brinza, C. M. Western, and K. C. Janda, J. Chem. Phys. **88**, 6272 (1984).

6. S. R. Hair, J. I. Cline, C. R. Bieler, and K. C. Janda, J. Chem. Phys. **90**, 2935 (1989).

7. J. C. Drobits and M. I. Lester, J. Chem. Phys. **86**, 1662 (1987).

8. L. Khundkar and A. H. Zewail, Annu. Rev. Phys. Chem. **41**, 15 (1990), and references therein.

9. M. L. Alexander, N. E. Levinger, M. A. Johnson, D. Ray, and W. C. Lineberger, J. Chem. Phys. **88**, 6200 (1988); D. Ray, N. E. Levinger, J. M. Papanikolas, and W. C. Lineberger, J. Chem. Phys. **91**, 6533 (1989); J. M. Papanikolas, J. R. Gord, N. E. Levinger, D. Ray, V. Varsa, and W. C. Lineberger, J. Phys. Chem. **95**, 8028 (1991).

10. F. G. Amar, and B. J. Berne, J. Phys. Chem. **88**, 6720 (1984); L. Perera and F. G. Amar, J. Chem. Phys. **90**, 7354 (1989); F. G. Amar and L. Perera, Z. Phys. D **20**, 173 (1991); F. G. Amar and S. Weerasinghe in *Mode Selective Chemistry, Proceedings of the 24th Jerusalem Quantum Chemistry Symposium*, B. Pullman and J. Jortner eds., (Kluwer, Amsterdam, 1991).

11. J. A. Blazy, B. M. DeKoven, T. D. Russell, and D. H. Levy, J. Chem. Phys. **72**, 2439 (1980).

12. D. H. Levy, Adv. Chem. Phys. **47**, part I, 323 (1981).

13. Program written by M. Gruebele.

14. P. R. Bevington, *Data Reduction and Error Analysis for the Physical Sciences*, McGraw-Hill, New York (1969), pp. 204.

15. M. E. Kellman, Chem. Phys. Lett. **76**, 225 (1980).

16. Only the continuum states are assumed to be energy normalized [see Equation (4) in (III) and Equation (8) here where ρ does not appear explicitly]. Equation (7) is for discrete states and thus the density of states ρ appears explicitely.

17. P. M. Felker and A. H. Zewail, Adv. Chem. Phys. **70**, part I, 265 (1988), and references therein.

18. P. M. Felker and A. H. Zewail, J. Chem. Phys. **82**, 2975 (1985); D. R. Demmer, J. W. Hager, G. W. Leach and S. C. Wallace, Chem. Phys. Lett. **136**, 329 (1987); X. Song, C. W. Wilkerson, J. Lucia, S. Pauls and J. P. Reilly, Chem. Phys. Lett. **174**, 377 (1990); P. G. Smith and J. D. McDonald, J. Chem. Phys. **92**, 1004 (1990); J. M. Smith, C. Lakshminarayan and J. L. Knee, J. Chem. Phys. **93**, 4475 (1990); A. J. Kaziska and M. R. Topp, Chem. Phys. Lett. **180**, 423 (1991).

19. See Reference 17 for the correspondence and the limits between the quantum treatment of IVR and the kinetic equation approach.

20. A superscript VP is used for k^{VP} [instead of k_{VP} as in (III)] because of the multiple steps involved in the VP processes discussed here; these steps are labelled by subscripts, for example, k_1^{VP}.

21. A. Garcia-Vela, P. Villarreal, and G. Delgado-Barrio, J. Chem. Phys. **94**, 7868 (1991).

22. D. H. Semmes, J. S. Baskin, and A. H. Zewail, J. Chem. Phys. **92**, 3359 (1990).

23. M. Dantus, R. M. Bowman, M. Gruebele, and A. H. Zewail, J. Chem. Phys. **92**, 3359 (1989).

24. W. D. Sands, C. R. Bieler and K. C. Janda, J. Chem. Phys. **95**, 729 (1991).

25. J. E. Adams and R. M. Stratt, J. Chem. Phys. **93**, 1332 (1990).

26. A. H. Zewail, Ber. Bunsenges. Phys. Chem. **89**, 264 (1985).

27. N. Halberstadt, J. A. Beswick, O. Roncero, and K. C. Janda, J. Chem. Phys. **96**, 2404 (1992).

28. S. K. Gray, Chem. Phys. Lett. (in press).

29. D. D. Evard, J. I. Cline, K. C. Janda, J. Chem. Phys. **88**, 5433 (1988).

30. J. A. Syage, P. M. Felker, and A. H. Zewail, J. Chem. Phys. **81**, 4706 (1984).

31. G. C. Schatz, V. Buch, M. A. Ratner, and R. B. Gerber, J. Chem. Phys. **79**, 1808 (1983).

32. R. E. Smalley, L. Wharton, and D. H. Levy, J. Chem. Phys. **68**, 671 (1978).

33. P. C. Engelking, J. Chem. Phys. **85**, 3103 (1986); **87**, 936 (1987).

34. M. Dantus, R. M. Bowman, A. Mokhari and A. H. Zewail, J. Photochem. Photobiol. A **62**, 301 (1992).

35. Y. Yan, R. M. Witnell, K. R. Wilson, and A. H. Zewail, Chem. Phys. Lett. **193**, 402 (1992).

36. D. M. Willberg, M. Gutmann, E. E. Nitikin, and A. H. Zewail, Chem. Phys. Lett. **201**, 506 (1993).

Table 1. The rates and time constants for the I_2Ne_2 system:

$$I_2Ne_2(v_i') \longrightarrow I_2(v_f' = v_i' - 2) + 2Ne, \quad m = 2.$$ [a]

v'_i	$\tau_0/2$ (ps)[b]	τ_1 (ps)	τ_2 (ps)	k_1 (10^9 s^{-1})	k_2 (10^9 s^{-1})
17	63	84 ± 8	165 ± 12	12 ± 2	6 ± 1
18	54	65 ± 5	139 ± 9	15 ± 2	7 ± 1
19	44	47 ± 4	97 ± 4	21 ± 2	10 ± 1
20	39	41 ± 2	91 ± 4	24 ± 2	11 ± 1
21	35	38 ± 5	86 ± 5	26 ± 4	12 ± 1
22	29	23 ± 3	76 ± 5	43 ± 6	13 ± 1
23	27	19 ± 3	44 ± 5	53 ± 9	23 ± 3

[a] The specific values reported for τ_1 and for τ_2 are the averages measured for a number of transients; the reported errors are one standard deviation.

[b] These are half the vibrational predissociation lifetimes for $I_2Ne(v'_i)$, reported in chapter 3; see the text for further explanation.

Table 2. A comparison of the measured rate constants with those predicted by the model described in the text.

v'_i	k_1 (10^9 s^{-1})	k^c_1 (10^9 s^{-1})[a]	k_2 (10^9 s^{-1})	k^c_2 (10^9 s^{-1})[a]
17	12 ± 2	16	6 ± 1	6
18	15 ± 2	19	7 ± 1	8
19	21 ± 2	23	10 ± 1	9
20	24 ± 2	26	11 ± 1	11
21	26 ± 4	29	12 ± 1	13
22	43 ± 6	34	13 ± 1	14
23	53 ± 9	37	23 ± 3	17

[a] k^c_1 is calculated by Equation (10) using the results for VP of I_2Ne from (I); $k^c_1(v) = 2k_0(v)$. k^c_2 is derived from the results of (I); $k^c_2(v\text{-}1)$. For details, see the text.

Table 3. The effective rate and time constants measured for a number of I_2Ne_n systems: $I_2Ne_n(v'_i) \longrightarrow I_2(v'_f) + n\text{Ne}$

v'_i	v'_f	τ_{eff} (ps)	τ^c_{eff} (ps)	$k_{eff}(10^9\ s^{-1})$	$k^c_{eff}(10^9\ s^{-1})$
a) I_2Ne, $m = 1$					
13	12	216 ± 16	216 ± 16	4.6 ± 0.4	4.6 ± 0.4
14	13	196 ± 12	196 ± 12	5.1 ± 0.3	5.1 ± 0.3
15	14	182 ± 20	182 ± 20	5.5 ± 0.6	5.5 ± 0.6
16	15	160 ± 15	160 ± 15	6.3 ± 0.6	6.3 ± 0.6
17	16	126 ± 12	126 ± 12	7.9 ± 0.8	7.9 ± 0.8
18	17	107 ± 9	107 ± 9	9.3 ± 0.9	9.3 ± 0.9
19	18	87 ± 4	87 ± 4	11.5 ± 0.9	11.5 ± 0.9
20	19	78 ± 4	78 ± 4	12.8 ± 1.0	12.8 ± 1.0
21	20	69 ± 6	69 ± 6	14.5 ± 0.7	14.5 ± 0.7
22	21	58 ± 3	58 ± 3	17.2 ± 0.9	17.2 ± 0.9
23	22	53 ± 3	53 ± 3	18.9 ± 1.0	18.9 ± 1.0
b) I_2Ne_2, $m = 2$					
17	15	209 ± 19	184	4.8 ± 0.5	5.4
18	16	172 ± 10	147	5.8 ± 0.4	6.8
19	17	124 ± 6	124	8.1 ± 0.4	8.1
20	18	112 ± 4	103	8.9 ± 0.4	9.7
21	19	103 ± 4	92	9.7 ± 0.4	10.9
22	20	81 ± 10	80	12.3 ± 1.6	12.5
23	21	51 ± 3	69	19.6 ± 1.2	14.5
c) I_2Ne_2, $m = 3$					
19	16	230 ± 30	124	4.3 ± 0.6	8.1
20	17	162 ± 13	103	6.2 ± 0.5	9.7
21	18	145 ± 11	92	6.9 ± 0.6	10.9
22	19	114 ± 7	80	8.8 ± 0.6	12.5
d) I_2Ne_3, $m = 4$					
20	16	173 ± 18	129	5.8 ± 0.6	7.8
21	17	156 ± 9	107	6.4 ± 0.4	9.3
22	18	130 ± 7	95	7.7 ± 0.5	10.5
23	19	118 ± 7	84	8.5 ± 0.5	11.9
e) I_2Ne_4, $m = 5$					
22	17	176	109	5.7	9.2

5.6 Figure Captions

1. An experimental transient of I_2Ne_2 ($v'_i = 21/v'_f = 19$) together with fits to a single exponential rise convoluted with a 40 ps system response (A), and to a double exponential rise convoluted with a 40 ps system response (B). The robustness of these fits are discussed in the text.
2. Typical I_2Ne_n transients for various values of v'_i: (A) transients for $n = 1$, (B) transients for $n = 2$, (C) transients for $n = 3$, and (D) shows a transient recorded for a $n = 4$ cluster.
3. The experimental rates k_1 and k_2, and the theoretical rates, k_1^c and k_2^c,vs. the initially prepared vibrational state v'_i. A description of the theoretical model is given in the text.
4. Two I_2Ne_2 ($v'_i = 21$) transients showing the m dependence of VP.
5. The v'_i dependence of the effective reaction rates for a number of I_2Ne_n clusters. A description of the effective rates is presented in the text.

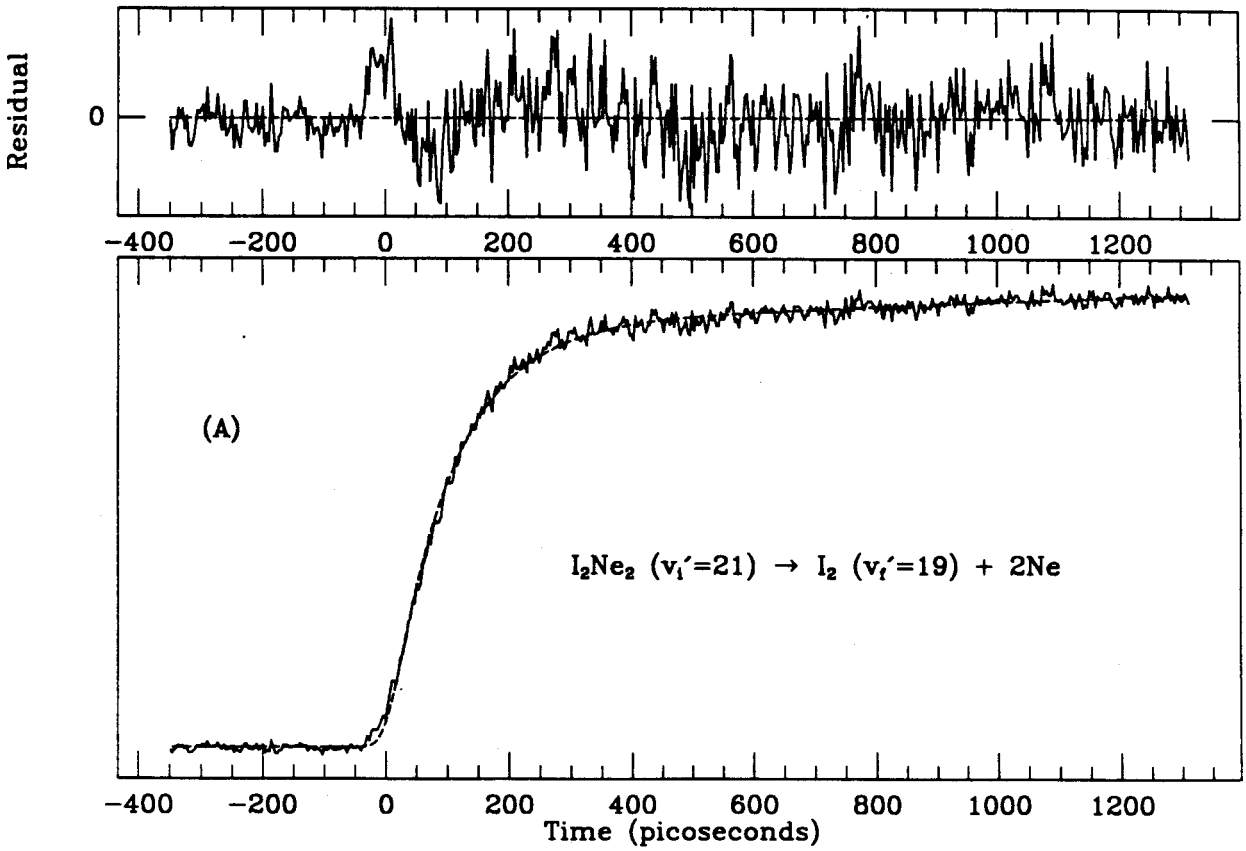
Residual
0
−400
−200
0
200
400
600
800
1000
1200
(A)
I_2Ne_2 (v_i'=21) → I_2 (v_f'=19) + 2Ne
Time (picoseconds)

Figure 1 (A)

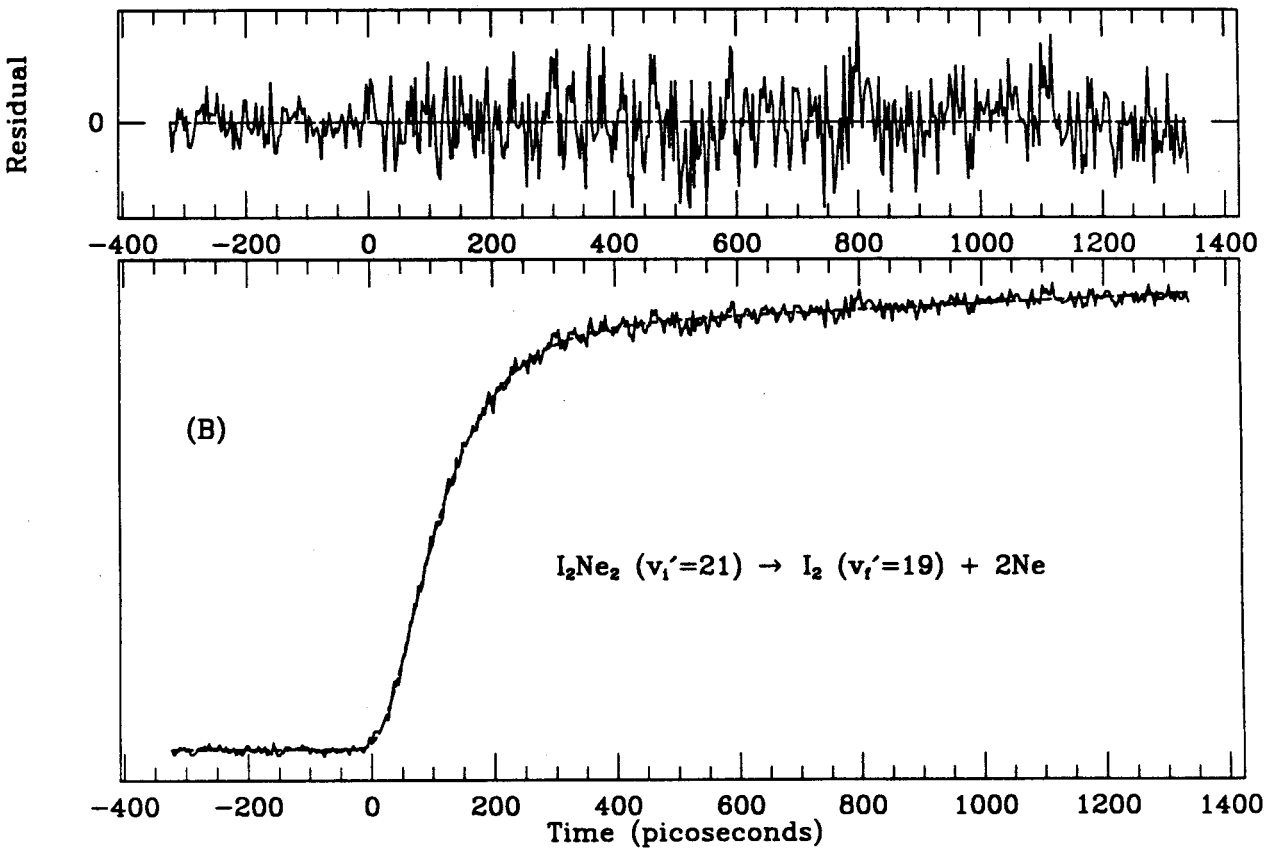
Residual
0
−400
−200
0
200
400
600
800
1000
1200
1400
(B)
I_2Ne_2 (v_i'=21) → I_2 (v_f'=19) + 2Ne
Time (picoseconds)

Figure 1 (B)

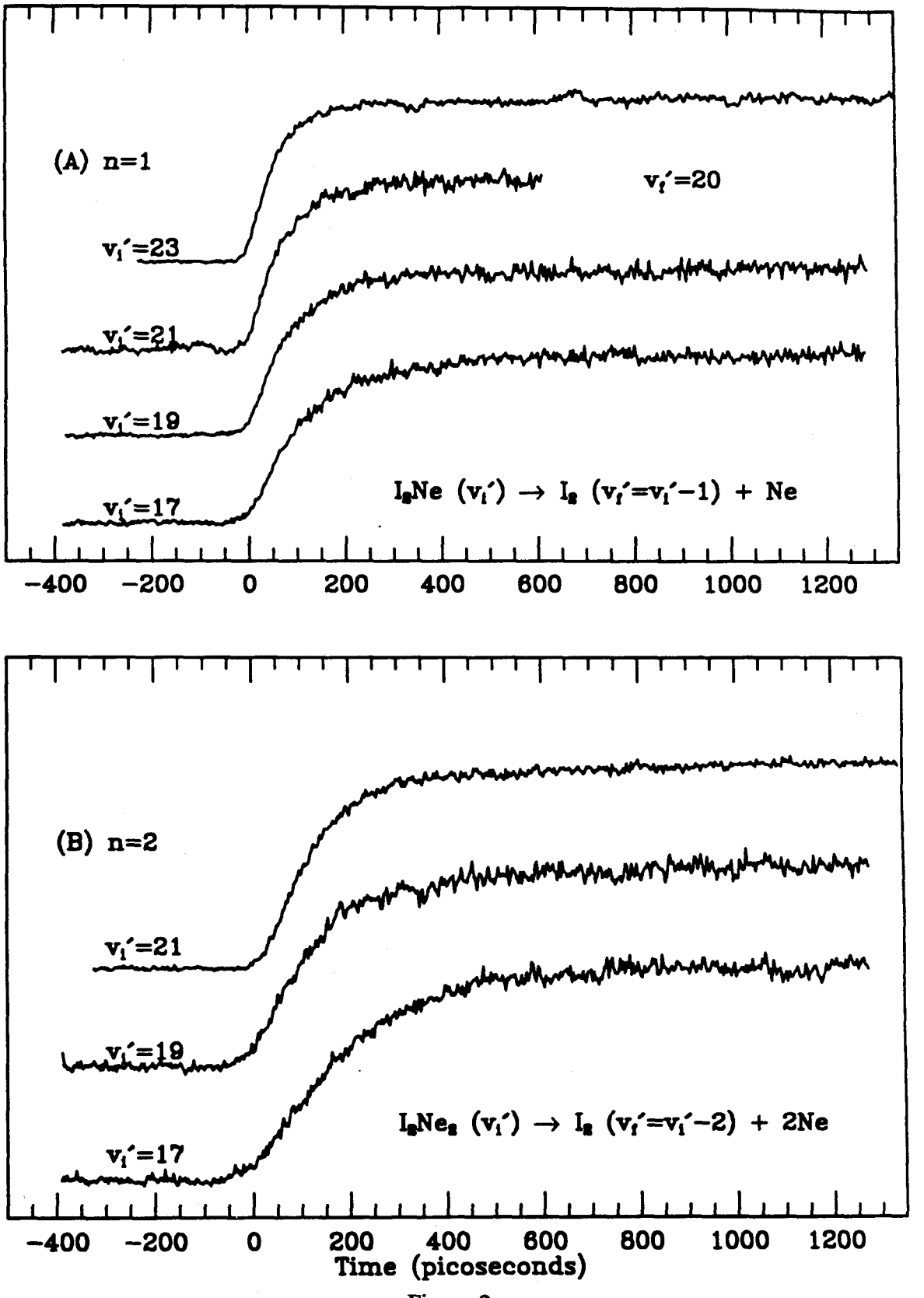
(A) n=1
v_i'=23
v_i'=21
v_i'=19
v_i'=17
v_f'=20
I_2Ne (v_i') → I_2 (v_f'=v_i'−1) + Ne
−400 −200 0 200 400 600 800 1000 1200
(B) n=2
v_i'=21
v_i'=19
v_i'=17
I_2Ne_2 (v_i') → I_2 (v_f'=v_i'−2) + 2Ne
−400 −200 0 200 400 600 800 1000 1200
Time (picoseconds)

Figure 2

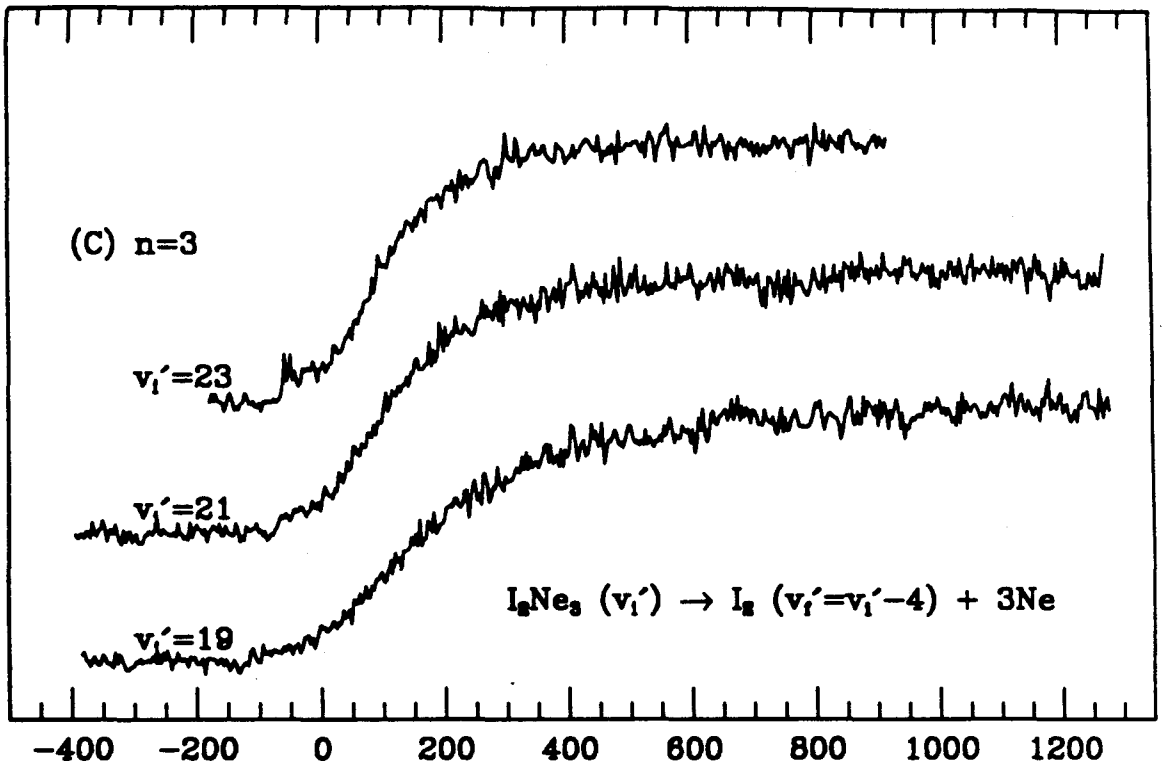

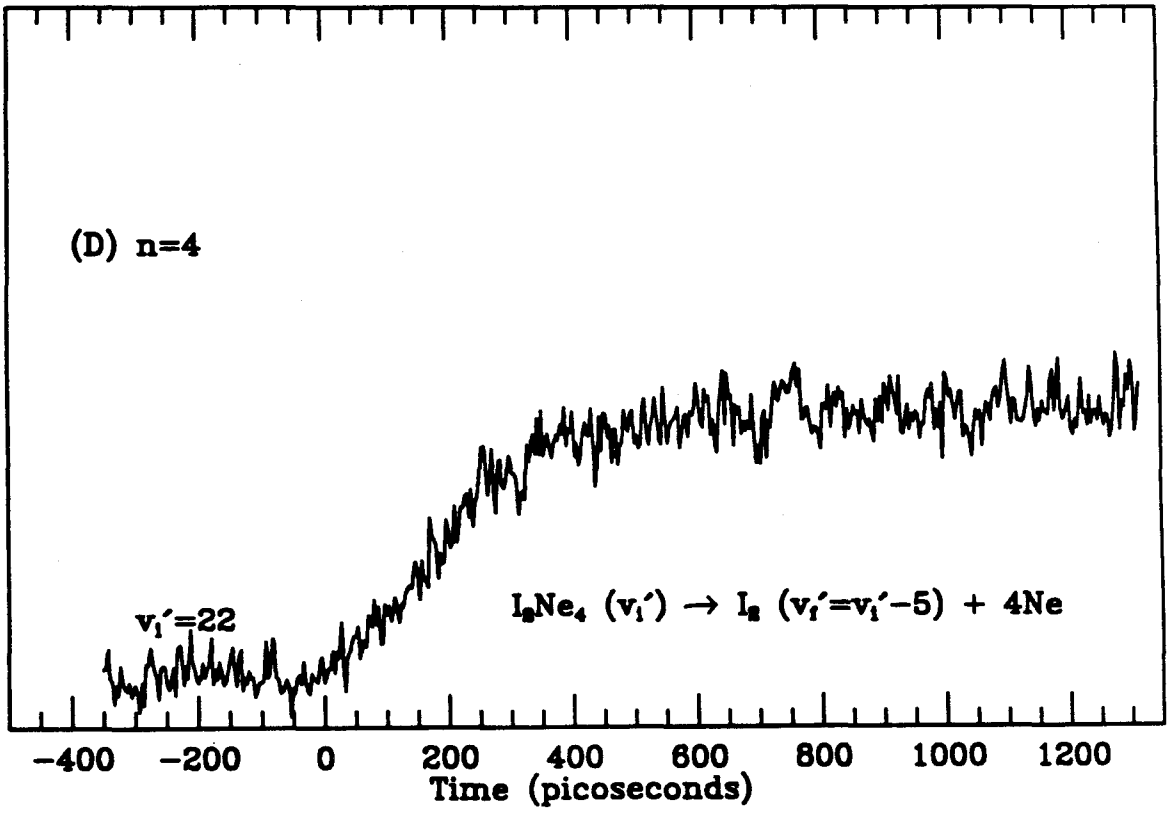

Figure 2 (continued)

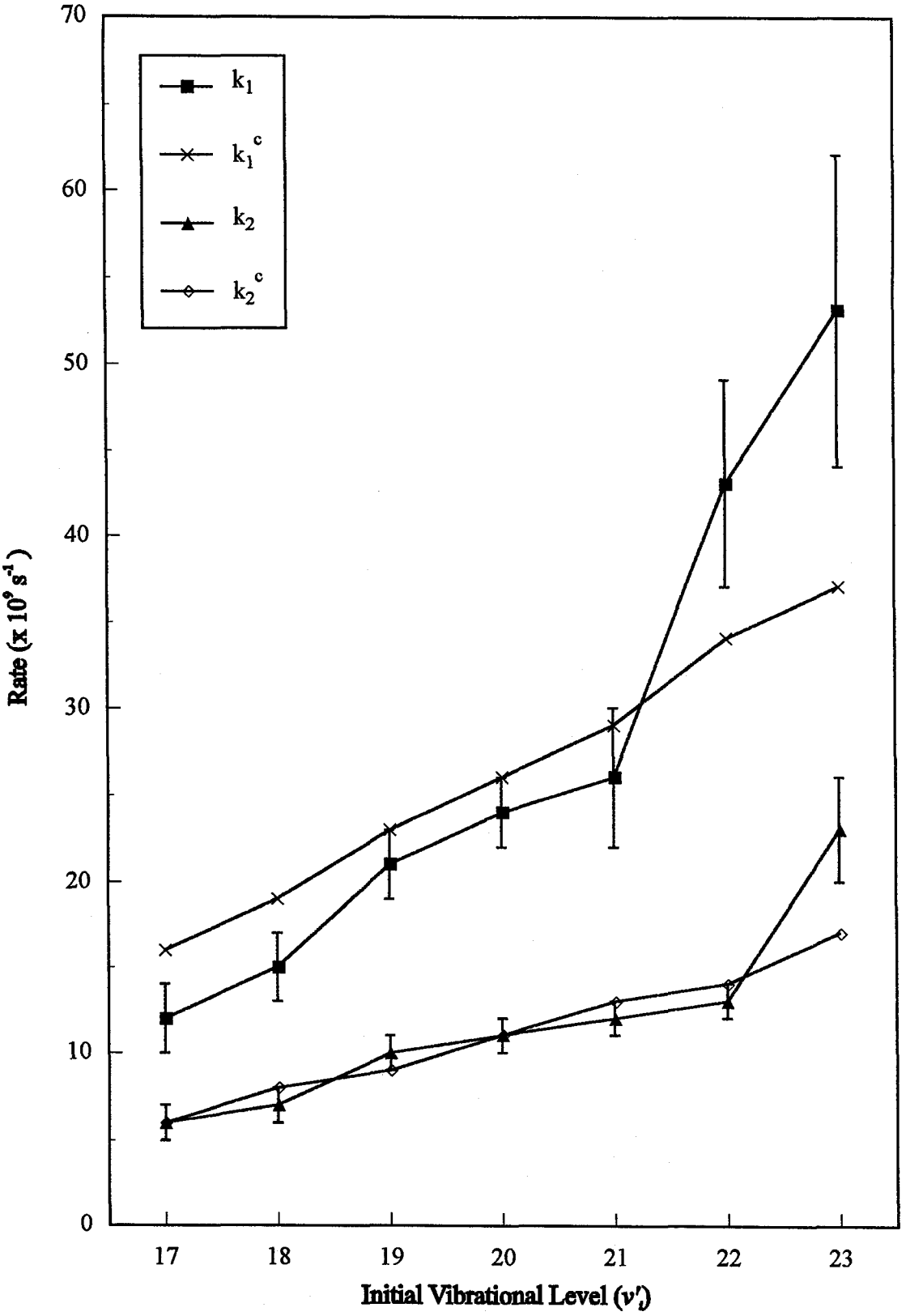
70
60
50
40
30
20
10
0
Rate (x 10⁹ s⁻¹)
k1
k1c
k2
k2c
17
18
19
20
21
22
23
Initial Vibrational Level (v'i)

Figure 3

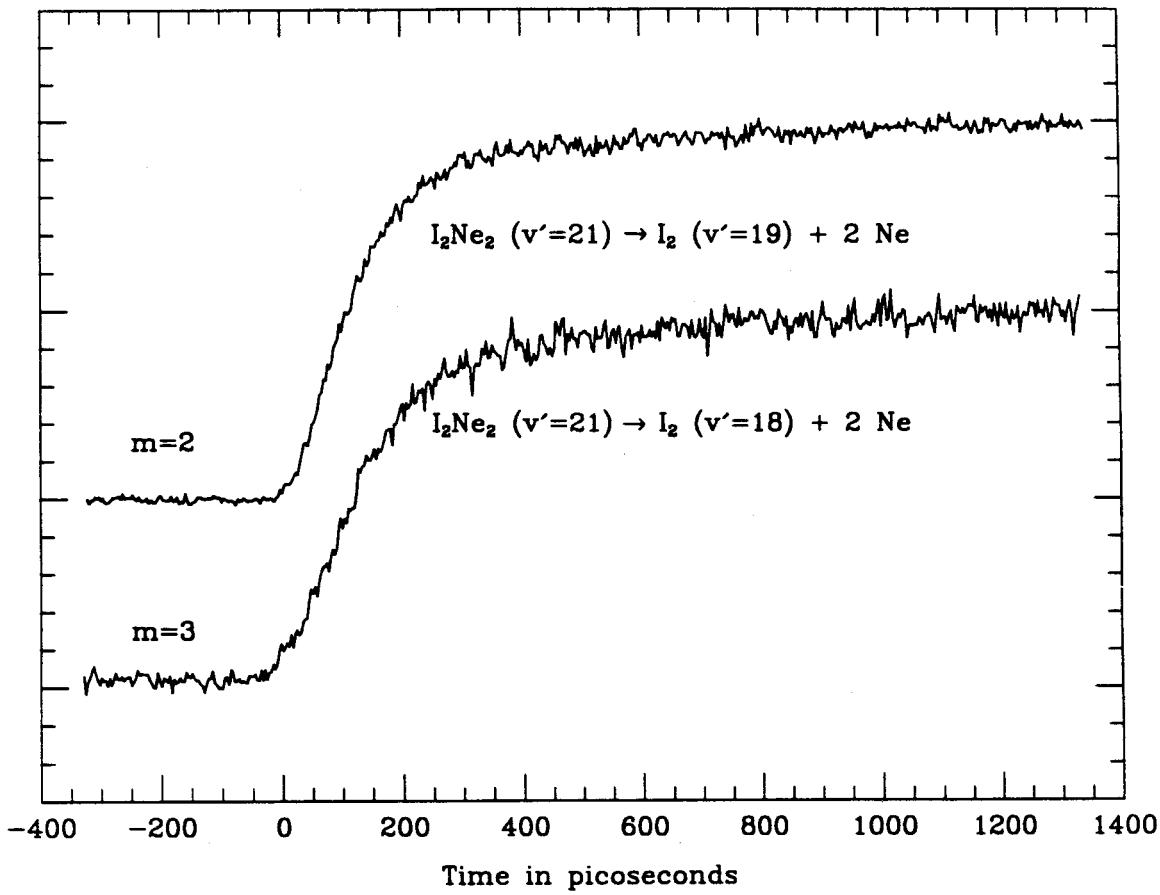
I_2Ne_2 (v′=21) → I_2 (v′=19) + 2 Ne
I_2Ne_2 (v′=21) → I_2 (v′=18) + 2 Ne
m=2
m=3
−400
−200
0
200
400
600
800
1000
1200
1400
Time in picoseconds

Figure 4

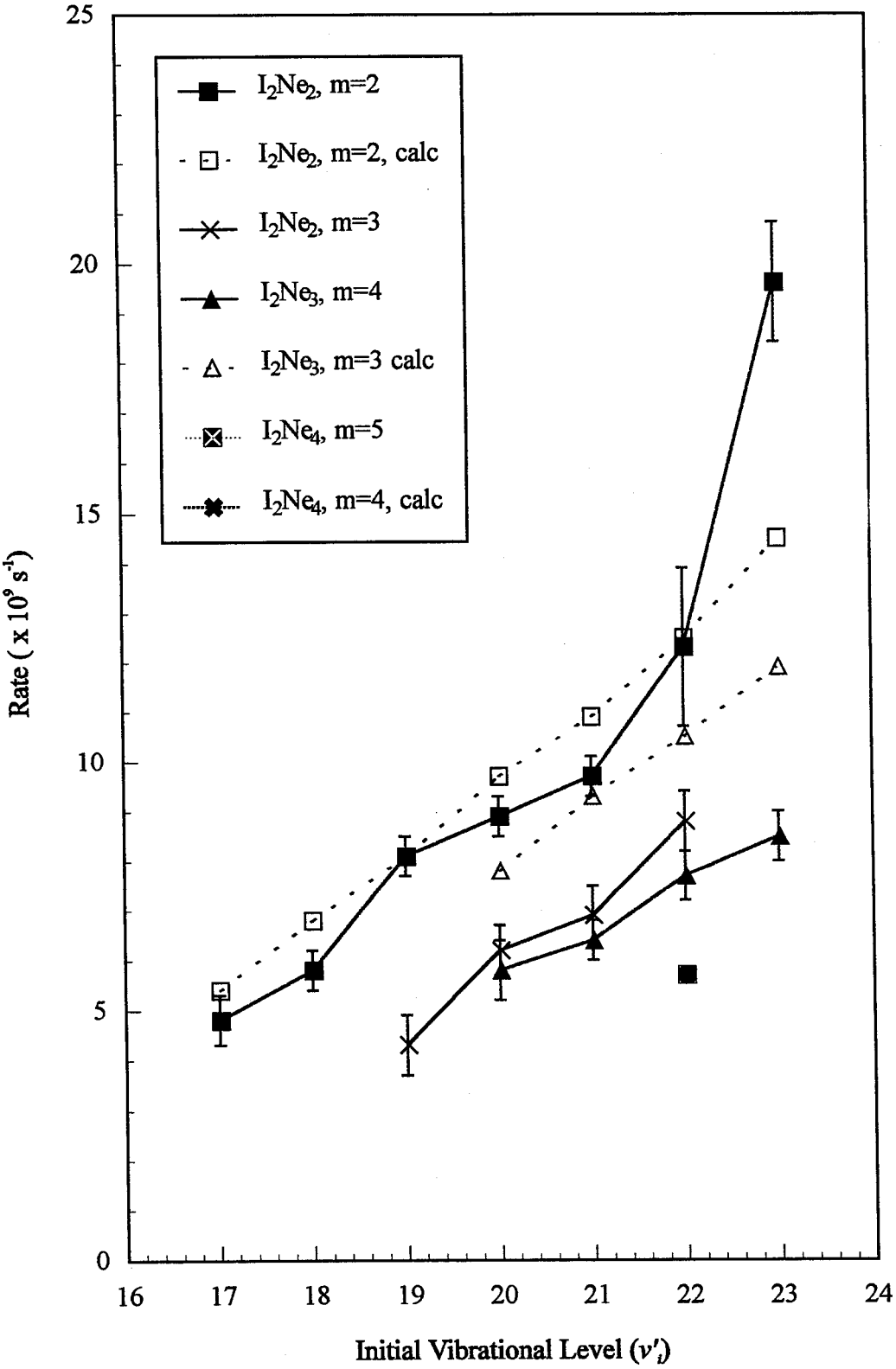
25
20
15
10
5
0
16
17
18
19
20
21
22
23
24
Rate (x 10^9 s^{-1})
Initial Vibrational Level (v'_i)
I_2Ne_2, m=2
I_2Ne_2, m=2, calc
I_2Ne_2, m=3
I_2Ne_3, m=4
I_2Ne_3, m=3 calc
I_2Ne_4, m=5
I_2Ne_4, m=4, calc

Figure 5

Chapter VI

Multi-Photon Ionization/Time-Resolved Mass Spectroscopic Investigations of Dynamical Processes in van der Waals Clusters

6.1 Introduction

As previously discussed in Chapter II of this thesis, the molecular beam system was constructed so that dynamical processes in mass-selected clusters could be time-resolved. Such experiments are performed using the combination of resonant-enhanced-multiphoton-ionization (REMPI) and time-of-flight mass spectroscopy (TOFMS). Briefly, the pump laser prepares a population of clusters in an excited state and initiates the dynamical process, *i. e.*, a proton transfer or an isomerization. For both the α-naphthol and stilbene cluster experiments performed in our laboratory (*vide infra*), the pump laser is tuned to the $S_1 \leftarrow S_0$ transition of the organic moiety. At a fixed time later, the probe laser interrogates the remaining population of the reactants by exciting them to the ionization continuum. Often, many cluster species have overlapping $S_1 \leftarrow S_0$ transitions, and/or overlapping ionization transitions, thereby eliminating the possibility of specifically exciting a given cluster via tuning the wavelength of either the pump or probe lasers. Therefore, in order to distinguish clusters of different masses, the ionized clusters are mass analyzed using the TOF spectrometer. A transient for a given cluster species can be obtained by setting the boxcar gate to intercept the signal of a particular mass.

The first complete set of REMPI/TOFMS experiments performed in this laboratory were the studies of excited state proton transfer in clusters of α-naphthol (NpOH) and ammonia, water, and piperidine(collectively represented as X).[1,2] In these experiments, the rate of proton transfer between the naphthol moiety of the cluster and the *surrounding* solvent molecules was measured:

$$\mathrm{NpOH(X)}_n \xrightarrow{k_{PT}} \mathrm{NpO^-(XH^+)}_n. \qquad (1)$$

The rate of proton transfer was measured as a function of cluster size. In this experiment, we found that proton transfer did not occur for ammonia clusters where $n < 3$, or for piperidine clusters of $n < 2$. Furthermore, no proton transfer was detected for any of the

water clusters studied ($n \leq 20$). This system, and systems like it, have become prototypical reactions for the time-resolved study of solvation effects on acid/base reactions.[3,4]

Recently, we have begun the study of another prototypical system: the excited state isomerization of *trans*-stilbene. As the reader who is familiar with the literature of physical chemistry well knows, the isomerization of stilbene has been extensively studied for the last fifty years. Reference 5 is the latest review dedicated to the photoisomerization dynamics of stilbene; it covers the studies done on the isolated gas phase molecule, as well as studies on stilbene dynamics in solution. A thorough study of the photoisomerization of *t*-stilbene isolated in a molecular beam has been presented in a series of papers published by this research group.[6] These previous investigations provide information on the energetics, influence of IVR on isomerization, and the actual rates of photoisomerization of the isolated *t*-stilbene molecule. One of the major unanswered questions regarding the isomerization of *t*-stilbene is the order of magnitude acceleration of the rate of isomerization in solution, as compared with the rate measured for the isolated molecule in molecular beam experiments.

Measuring the rates of isomerization in clusters would be a feasible experiment to help understand the effects of the solvent on the reaction rate at a microscopic level. There are two main advantages of this approach, the first being that the energy of a cluster, as in the case for an isolated molecule, is determined solely by the frequency of the excitation laser (note, that there will be some residual vibrational energy left in the cluster after the nucleation process). Therefore the excess vibrational energy in the cluster, *i. e.*, the energy of the cluster above the origin of the $S_1 \leftarrow S_0$ transition, can be controlled simply by tuning the pump laser. In other words, the cluster is a microcanonical solution, with a fixed value for its vibrational energy, as determined by the pump laser. Secondly, since our experimental system has the capability of mass resolution, the effect of solvent properties such as viscosity and polarity on the rate of *t*-stilbene isomerization can be

studied as a function of cluster size. This should allow one to determine how many solvent molecules are required in order for the isomerization rate in clusters to approach its value in bulk solutions.

It is important to note that the behavior of clusters do not necessarily mimic the microscopic behavior of solvent-solute interactions in solutions. However, due to the ability to control the energetics of the cluster, it may be possible to separate the effects of viscosity and collisional activation on the rate of isomerization. In solutions, the *t*-stilbene molecule can obtain the energy needed for isomerization from collisions with the solvent molecules. In clusters, however, the surrounding solvent molecule shell will most likely act as a sink of vibrational energy due to IVR. Also, an additional influence that the solvent shell in a cluster will have on the rate of stilbene isomerization will be its *viscosity* effects on the isomerization reaction coordinate.

Preliminary experiments on the radiative lifetime of *t*-stilbene in argon clusters, $St(Ar)_n$, excited to the origin of the $S_1 \leftarrow S_0$ transition have been performed in this laboratory.[7] It is important to note that at the origin, non-radiative decay channels such as isomerization and internal conversion are not accessed; all relaxation proceeds via the fluorescence channel.[8] In these experiments, the radiative lifetime of *t*-stilbene (2.7 ns for the isolated molecule), was measured as a function of n. Within the limits of experimental error (~ 10%) we did not observe any changes in the radiative lifetime for clusters up to $n = 10$.

Presently, our goal is to extend these preliminary results and study the rates of isomerization of *t*-stilbene in argon clusters. Unfortunately, the beginnings of these experiments on clusters of *t*-stilbene have been complicated by a number of technical difficulties, including the replacement of the VHS-10 cryobaffle, complete reconstruction of the TOFMS Einzel lens assembly, replacement of the multi-channel plate (MCP) detection system, and a complete overhaul of the nozzle heating system. Therefore, at this point, we have only obtained preliminary results for the stilbene system, and are only now

approaching the point where it may be possible to measure the rates of isomerization.[9] Along with the repairs done on the system over the last eight months, we have developed a number of procedures that should enhance the operation of the system in its TOFMS mode. The following section is a discussion of the alignment and operation of the laser/molecular beam apparatus for REMPI-TOFMS type experiments, analogous to the procedure outlined in Chapter II for laser induced fluorescence (LIF) experiments.

6.2 Experimental

6.2.1 Alignment of the Lasers

The laser system for REMPI-TOFMS experiments was aligned in the same manner as described in Chapter II for LIF-type experiments; the only major modification was how the pump and probe laser pulses were *combined* before entering the molecular beam. All of the TOFMS experiments were performed using a 1 (UV photon)+1 (UV photon) resonant MPI configuration. That is, both the pump and probe laser pulses were frequency doubled and were both in the UV spectral region. It was not possible to find a dichroic beamsplitter that would be highly reflective to the pump pulse and at the same time be highly transmisive for the probe pulse. Therefore, rather than combining the two laser pulses in a collinear configuration, the two laser pulses had to be sent to the molecular beam in a parallel arrangement using two combining mirrors. The mirrors are placed close together so that the paths of the pump and probe laser beams lie only 5 mm apart. Although this method preserved the energy of each of the pump and probe pulses, it made it much more difficult to spatially overlap the two lasers on the molecular beam inside the chamber. Two Klinger SL51BD mirror mounts are used for the combining mirrors, as they have exceptional thermal and mechanical stability. Their fine adjustment micrometers were also required for fine tuning the overlap of the pump and probe pulses, as described below.

An air-gap UV achromat was installed on the bottom of the ionization cube inside the buffer chamber in order to focus the two lasers to the same point on the molecular beam.[10] This achromat was required for two reasons. First, due to the inherently low UV pulse energy (<< 1 μJ) of both the pump and the probe lasers, tight focusing was required to achieve the high photon flux required for MPI. Secondly, since the two lasers were brought into the molecular beam chamber in a parallel configuration, they had to be spatially overlapped on the molecular beam. At the focal point of the achromat, both the pump and probe lasers could pass through a ~ 80 μm pinhole; therefore precise positioning of the achromat was crucial in order that the focal point was located on the molecular beam path. In order to achieve this precision, the achromat was mounted in a Newport optical positioning device that had been attached to the bottom flange on the ionization cube.[11] The position of the achromat could be adjusted along *x*, *y*, and *z* axes to optimize the overlap of the laser pulses with the molecular beam.

In order to assure that the pump and probe laser pulses were focusing on the same position, which also had to spatially overlap the path of the molecular beam, a pinhole target was built, as shown in Figure 1. This target could be mounted on the same flange as the Einzel lens assembly. The position of the pinhole could be adjusted with its micrometer so that it would exactly lie on the path of the molecular beam. The micrometers on the two combining mirrors could then be adjusted so that both the pump and probe lasers would pass through without clipping the edges of the pinhole (~ 80 μm).

6.2.2 Arrangement of the Molecular Beam

The set of TOFMS experiments on *t*-stilbene required heating of the solid stilbene sample to achieve a high enough vapor-pressure of stilbene to see signal. The previously described sample-holder/nozzle assembly was difficult to use and to clean, therefore a new sample holder was constructed for the present work on *t*-stilbene. A sketch of this sample-holder nozzle assembly is shown in Figure 2. Both the pulsed nozzle and the

sample holder could be actively heated independent of one another, with the same temperature controller used for the glass nozzle. In all experiments that required sample heating, the nozzle was maintained at a temperature of at least 10 °C greater than the sample holder, in order to minimize clogging of the nozzle. Under the recommendation of the manufacturer, the temperature of the nozzle was kept below 120 °C. It was discovered that the bellows tubing between the sample holder and the nozzle was an extremely poor thermal conductor, so poor that even in a vacuum it would act as a cold spot in the system unless it was actively heated. Therefore the best results were achieved when the nozzle itself was heated with a cartridge heater, and the sample holder and bellows tube were heated with a heating tape.

After the lasers were aligned, the ion optics reassembled into the cube, and vacuum chamber closed the molecular beam system was ready for evacuation. Typically the vacuum chambers would be pumped down, with the nozzle off, until the pressure in the expansion chamber was ~ 5×10^{-6} torr, and the pressure in the TOF chamber was ~ 5×10^{-7} torr. The pump down period usually required at least two hours. Once operational pressures had been achieved, the carrier-gas supply was turned on, the solenoid valve was activated, and the sample heaters were turned on slowly. For *t*-stilbene, the sample temperature was usually maintained at 100 °C and the nozzle temperature at 110 °C. When the nozzle parameters were set to 100 Hz repetition rate and 325 μs pulsewidth, the pressure in the expansion chamber typically was in the low 10^{-5} torr range. If the pressure in the expansion chamber was significantly higher, this usually indicated a leak in the gas delivery line inside the chamber.

It has been determined empirically that it takes approximately four to eight hours for the vapor pressure of *t*-stilbene to equilibrate in the free-jet expansion. Therefore, after a complete cleaning of the nozzle, the molecular beam was usually left running overnight or for a significantly long period of time before any of the experimental parameters were adjusted. Usually the molecular-beam apparatus would run for

approximately one to two weeks before the chamber had to be vented and the nozzle cleaned, as long as precautions were taken to prevent the accumulation of stilbene in the nozzle. As previously mentioned maintaining the nozzle at a temperature higher than that of the sample holder helped a great deal. Secondly, when the system was to be shut down for the night, the solenoid and the gas flow were left running for an hour after the heaters were turned off.

The carrier gas for the cluster experiments required much experimentation in order to determine which mixture of argon and helium provided the optimum cluster formation. A mixture of 5% Ar/95 % He was found to provide the optimum cluster formation. These percentages are based solely on the partial pressures of the two gases in the mixing cylinder. Mixtures ranging from 30 % Ar down to ~2 % Ar were tried. It should be noted that the high percentage of He was required for optimum cooling efficiency in the gas phase clusters. The mixtures were made in standard type K cylinders. Typically a cylinder was filled to 100 psig with argon (Liquid Air Products 99.9995 % purity), followed by several hundred psig of helium (Liquid Air Products 99.9999 % purity). It would take one to two days for complete mixing of the gases in the cylinder.

6.2.3 Signal Optimization

Once the lasers were aligned through the achromat, and the nozzle assembly was properly warmed up, the actual TOFMS experiment could be started. The first step was to ensure that the YAG laser was being triggered by the dual channel pulse generator. Much time has been lost over the years looking for signal when the YAG was being triggered internally. Secondly, the required high voltage was applied to the multichannel plate (MCP) detector. The MCP is a delicate and expensive detector, and the voltage should be slowly ramped up to the operational values of 1.8 - 2.0 kV. It is extremely important that no voltage be applied to the MCP when vacuum pressures in the TOF chamber exceed 1×10^{-6} torr, or serious damage to the plates may result. We found a

simple way to determine if the MCP detector was operational by monitoring its output on an oscilloscope, while the TOF chamber's ion-gauge was turned on. An ion signal, originating from the gauge, appeared like grass on the oscilloscope's screen. For the same reason the ion-gauge in the TOF chamber should be turned off when data is being collected.

When operating in the MPI mode, only three voltages were required for the ion-optics: 1) the repeller grid (also referred to as TOF1) which was set to 2.5 kV, 2) the extractor grid (also referred to as TOF2) which was set to 1.9 kV, 3) the Einzel lens voltage which was set to approximately 950 V. The optimum Einzel lens voltage depended on the mass of the cluster of interest, therefore its value was adjusted in order to optimize the signal for each experiment. The ground electrode, and the outer cylinders on the Einzel lens were grounded to the chamber. The four additional grids on the ion optics assembly, the filament, the filament bias, and the gate bias, are not required for MPI operation; they are used for electron impact ionization as described in Reference 2.

The initial optimization of the system for each experiment was usually accomplished by observing the mass spectrum using the LeCroy transient digitizer. Figure 3 shows a typical mass spectrum of the cluster distribution when *t*-stilbene was seeded into a 5 % Ar/ 95 % He gas mixture. This signal was entirely due to the pump laser, *i. e.*, two photons at the pump wavelength provide sufficient energy for ionization of any of the stilbene clusters. This *pump-alone* signal was useful for optimizing the molecular beam parameters, starting with the nozzle parameters, pulse width 1, and delay time 2, on the dual pulse generator. These parameters are discussed in Chapter 2 and control the timing and width of the gas jet exiting the solenoid valve. Following optimization of the nozzle parameters, the wavelength of the pump laser was adjusted to match the $S_1 \leftarrow S_0$ transition of the desired cluster. Once the signal of the cluster of interest was significant, and stable, the gated integrator would be used to monitor the signal during optimization.

Enhancement was achieved by optimized the overlap of the pump and probe lasers on the molecular beam. If the pinhole target was used as described above, and if the alignment of the two lasers had not been altered in the intervening time, usually minimal adjustments of the combining mirrors were required in order to spatially overlap the two laser pulses on the molecular beam. Furthermore, the telescope on the probe lasers output beam (see Figure 7 in Chapter II) could be adjusted to match the spot size of the probe laser and the pump laser on the molecular beam. Enhancement was easiest to detect when the pump laser was attenuated, or when the 100 μm solid etalon was used inside the pump laser in order to minimize the pump-alone signal. Figure 4 shows the enhancement obtained for a *t*-stilbene transient when the 100 μm solid etalon was used in the pump laser.

Since the transition to the ionization continuum is not sharp, the probe laser was operated without its 100 μm etalon so that it could operate at maximum laser intensity. When the probe wavelength was chosen, two factors had to be considered. First, a photon from the probe laser had to be sufficiently energetic to excite the molecule or the cluster to the ionization continuum. Usually the probe laser's wavelength was set for threshold ionization to minimize fragmentation of the clusters. Second, the probe laser's wavelength was chosen so that it would overlap a poor Franck-Condon region of the $S_1 \leftarrow S_0$ absorption spectrum; thereby minimizing any ionization solely caused by the probe laser.

6.3 References

1. J. J. Breen, L. W. Peng, D. M. Willberg, A. Heikal, P. Cong, and A. H. Zewail, J. Chem. Phys. **92**, 805 (1990).

2. L. W. Peng, *Ph. D. Thesis, California Institute of Technology*, (1991).

3. J. Lee, G. W. Robinson, S. P. Webb, L. A. Philips, and J. H. Clark, J. Am. Chem. Soc. **108**, 6538 (1986); S. P. Webb, L. A. Phillips, S. W. Yeh, L. M. Tolbert, and J. H. Clark, J. Phys. Chem. **90**, 5154 (1986).

4. (a) J. Steadman, and J. A. Syage, J. Phys. Chem. **95**, 326 (1991); (b) J. Steadman, and J. A. Syage, J. Am. Chem. Soc. **113**, 6786 (1991); (c) J. A. Syage, and J. Steadman, J. Chem. Phys. **95**, 2497 (1991); (e) O. Cheshnovsky, S. Leutwyler, J. Chem. Phys. **88**, 4127 (1988); (f) R. Knochenmuss, S. Leutwyler, J. Chem. Phys. **91**, 1268 (1989); (g) T. Droz, R. Knochenmuss, S. Leutwyler, J. Chem. Phys. **93**, 4520 (1990); (h) M. F. Hineman, G. A. Brucker, D. F. Kelley, and E. R. Bernstein, J. Chem. Phys. **97**, 3341 (1992).

5. D. H. Waldeck, *Chem. Rev.* **91**, 415 (1991), and references given therein.

6. (a) J. A. Syage, P. M. Felker, and A. H. Zewail, J. Chem. Phys. **81**, 4685 (1984);(b) J. A. Syage, P. M. Felker, and A. H. Zewail, J. Chem. Phys. **81**, 4706 (1984);(c) P. M. Felker, and A. H. Zewail, J. Phys. Chem. **89**, 5402 (1985).

7. D. M. Willberg Candidacy report.

8. P. M. Felker, W. R. Lambert, and A. H. Zewail, J. Chem. Phys. **82**, 3003 (1985).

9. Work in progress is presently being performed by A. Heikal.

10. See Reference 2 for a description of the ionization cube. Note the achromat was mounted in a Newport mount so that its focal length could be actively set on the molecular beam.

11. See Reference 2 for a description of the dimensions of the ionization cube.

6.4 Figure Captions

1. Diagram of the home-built sample holder and nozzle assembly. The solenoid valve and nozzle are standard Series 9 components from General Valve Inc. The 0.250" bellow tube assembly was made at the Caltech Chemistry Instrument shop; it is terminated with a female Swagelock 0.250" compression fitting at one end, and a male Swagelock 0.500" compression fitting at the oposite end. All components that come into direct contact with the sample are either stainless steel or teflon.
2. Diagram of the alignment pinhole and its mounting flange. The purpose of this pinhole is described in the text. Figure 2A shows the flange used for mounting the pinhole; all clearance holes are for 4-40 screws. Figure 2B shows the pinhole plate itself. Note that the actual pinhole is drilled through a 0.005" thick brass shim glued to the aluminum plate. Figure 3C shows the side view of the entire assembly, including the Deadal micrometer, ready for installation.
3. A typical mass spectrum of *t*-stilbene seeded into an expansion of 95 % He/ 5 % Ar backing gas. Stilbene-Argon clusters are labeled. The majority of the extraneous peaks are due to water contamination of the backing gas.
4. A typical transient obtained for bare *t*-stilbene under the conditions described in the text.

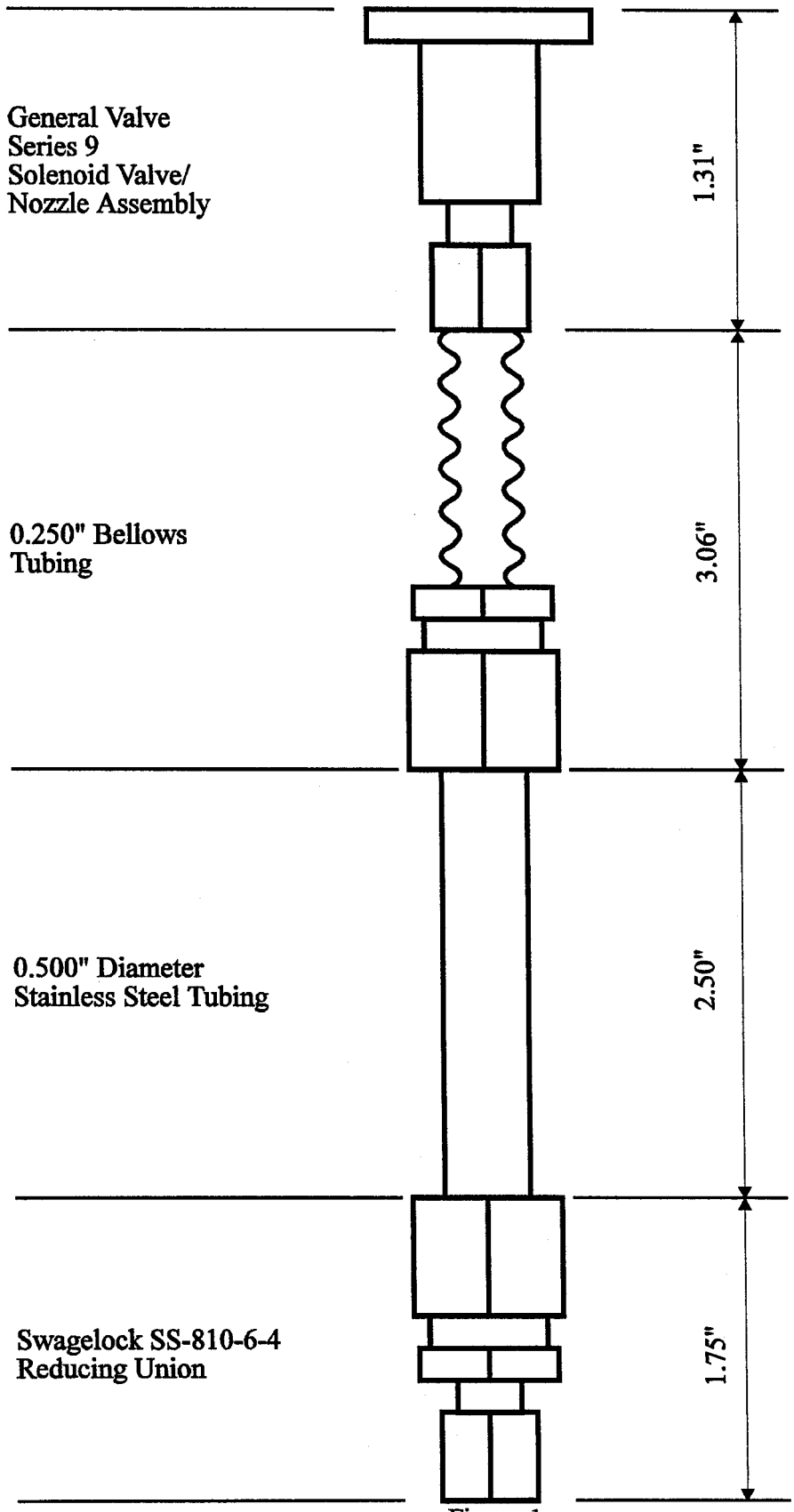
General Valve
Series 9
Solenoid Valve/
Nozzle Assembly
1.31"
0.250" Bellows
Tubing
3.06"
0.500" Diameter
Stainless Steel Tubing
2.50"
Swagelock SS-810-6-4
Reducing Union
1.75"

Figure 1

A

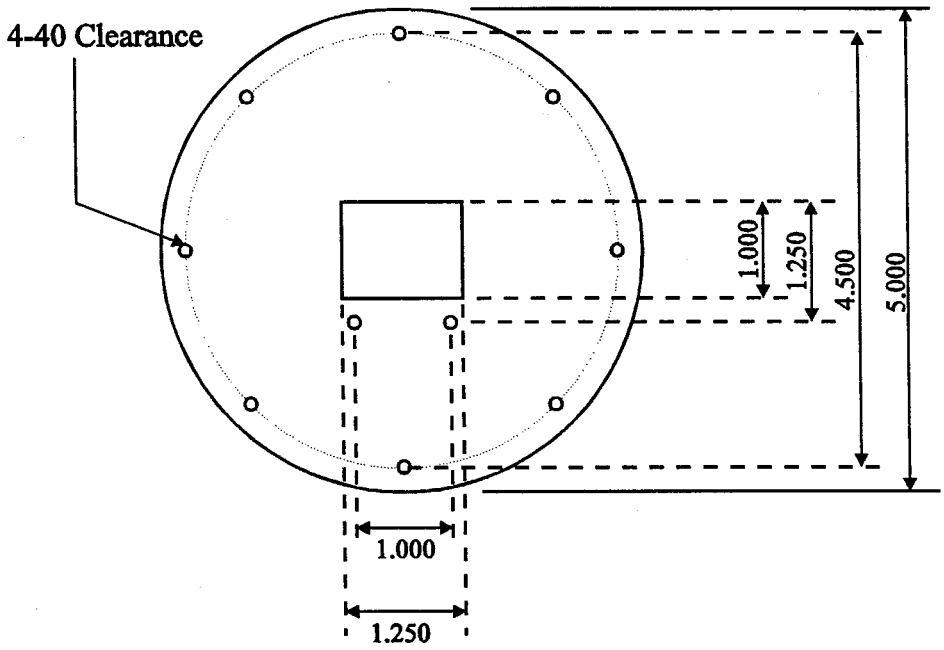
4-40 Clearance
1.000
1.250
4.500
5.000
1.000
1.250

B

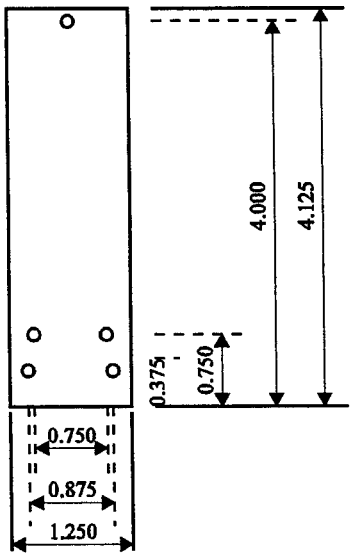
4.000
4.125
0.375
0.750
0.750
0.875
1.250

C

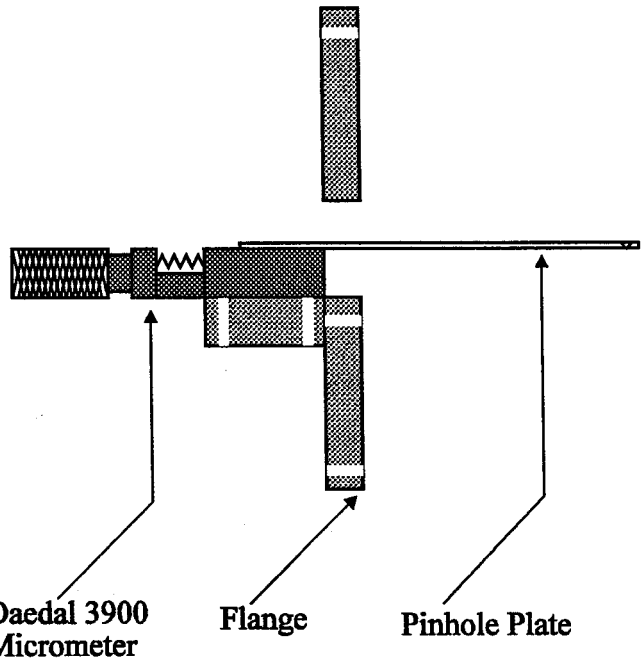
Daedal 3900
Micrometer
Flange
Pinhole Plate

Figure 2

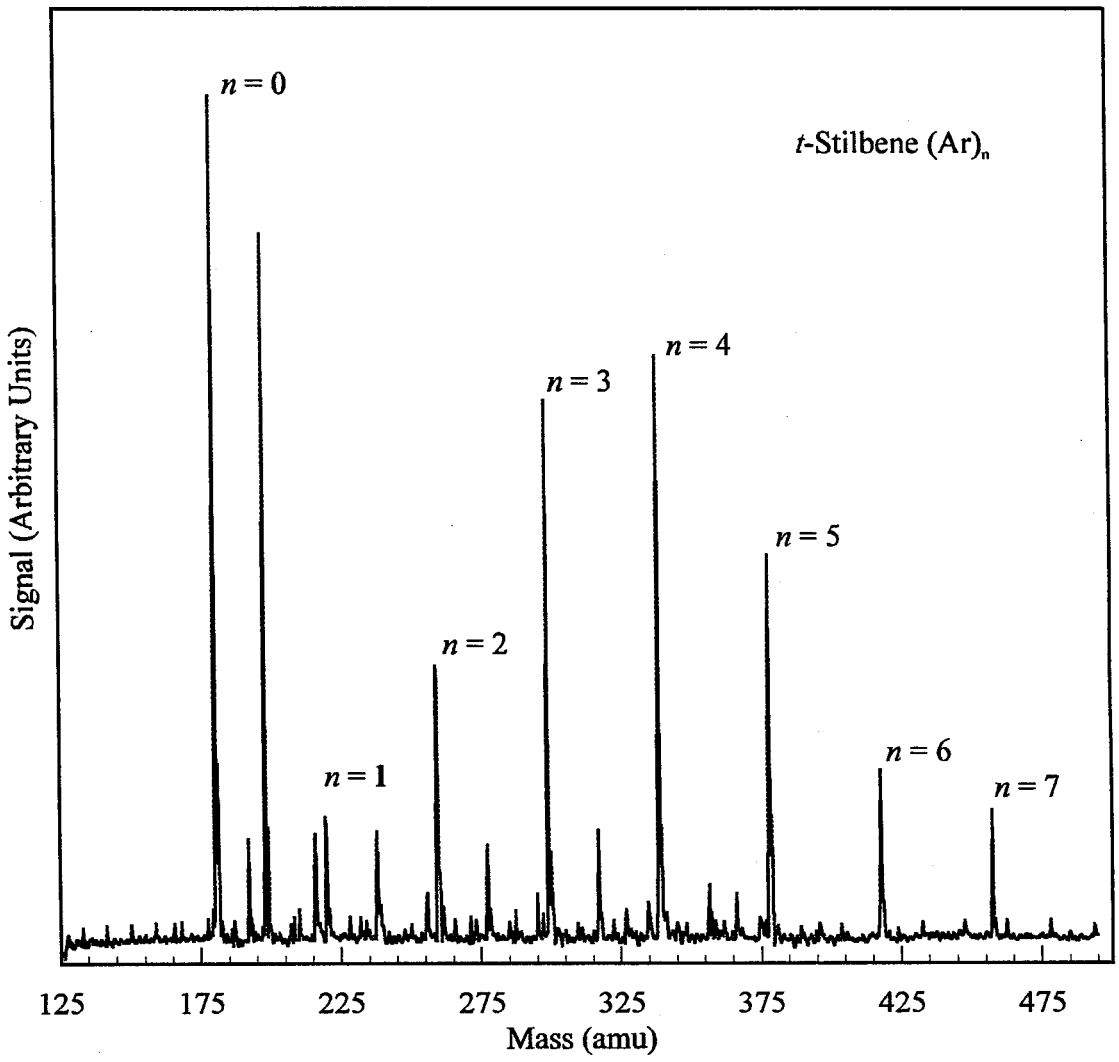
n = 0
t-Stilbene (Ar)n
n = 4
n = 3
n = 5
n = 2
n = 6
n = 1
n = 7
Signal (Arbitrary Units)
125
175
225
275
325
375
425
475
Mass (amu)

Figure 3

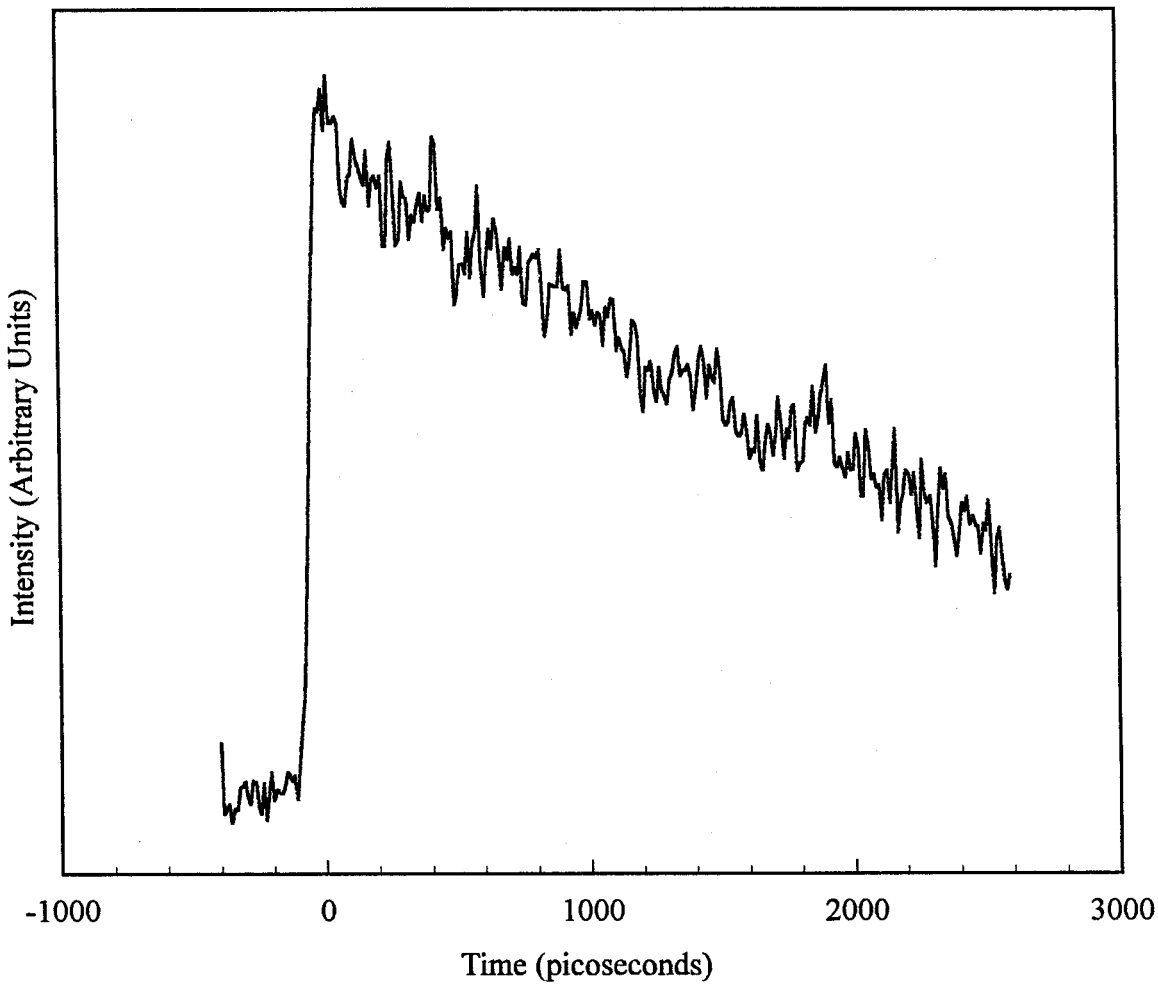
Intensity (Arbitrary Units)
-1000
0
1000
2000
3000
Time (picoseconds)

Figure 4